Pith:2026.000091v1 [gr-qc] 25 Nov 2026

Machine-verified six-coupling ultraviolet completion of gravity with matter and perturbative fakeon unitarity

Jonathan Washburn [1*]

[1]Recognition Physics Institute, Austin, Texas 78701, USA.

Corresponding author: Jonathan Washburn, e-mail: jon@recognitionphysics.org

Abstract

We present a machine-verified framework establishing the coupled ultraviolet fixed-point structure of higher-derivative quantum gravity with Standard Model and Recognition Science matter, the global phase and bifurcation topology of its graviton propagator, perturbative and distributional fakeon unitarity, and the elimination of continuum scalaron Landau poles by a discrete phase-comparison ceiling. First, within a bidirectional six-coupling functional renormalization group truncation retaining both dimension-six curvature cubes $\boldsymbol{C^3}$ (Goroff–Sagnotti) and $\boldsymbol{R^3}$ alongside $\boldsymbol{(G, \Lambda, C^2, R^2)}$, Banach contraction and Jordan-block-free $\mathbf{6 \times 6}$ characteristic-polynomial factorization certify five distinct non-Gaussian fixed points—pure gravity ($\mathbf{4+2}$ with a complex-conjugate pair) and both Near ($\mathbf{4+2}$, all real) and Far ($\mathbf{3+3}$, all real) physical branches for the Minimal Standard Model $\boldsymbol{(N_S, N_D, N_V) = (4, 45/2, 12)}$ and the three-generation $\mathbf{SM + 3\nu_R = (4, 24, 12)}$ spectrum—proving that $\boldsymbol{C^3}$ and $\boldsymbol{R^3}$ are simultaneously ultraviolet-irrelevant ($\boldsymbol{\theta_{C^3}, \theta_{R^3} < -2}$) at every certified fixed point while reducing conservatively to the five-coupling sector at zero $\boldsymbol{R^3}$ source. Second, in a first-principles Litim-integral five-coupling truncation across the continuous cutoff homotopy $\boldsymbol{s \in [0,1]}$ (Type II to Pure Type I) with derived Cardy ratios $\mathbf{1:11:62}$, affine-interval continuation certifies exact Donà–Eichhorn–Percacci scalar poles ($\boldsymbol{N_S^{pole} \in (40, 41)}$ for SM and $\boldsymbol{(41, 42)}$ for $\mathbf{SM + 3\nu_R}$ at Pure Type I, excluding the MSSM; $\boldsymbol{(7, 8)}$ at Type II, excluding two-Higgs-doublet models), a fermion-induced spin-$\mathbf{2}$ ghost-freedom transition $\boldsymbol{N_D^{ghost} \in (9, 37/4)}$, an exact ghost-free asymptotic-safety generation window $\boldsymbol{2 \le N_{gen} \le 7}$, a Stelle-to-Lee–Wick exceptional point $\boldsymbol{N_D^{LW} \in (10, 51/5)}$ placing SM and $\mathbf{SM + 3\nu_R}$ strictly inside the complex-conjugate Lee–Wick phase ($\boldsymbol{\Delta_{TT} < -100}$), and a global double-fold S-curve catastrophe ($\boldsymbol{F_1}$ at $\boldsymbol{N_D \in (56.85, 57)}$, $\boldsymbol{F_2}$ at $\boldsymbol{N_D \in (42, 42.5)}$) exhibiting triple fixed-point coexistence at $\boldsymbol{N_{gen} = 7}$. Third, for perturbative fakeon quantization, we prove arbitrary-loop parametric Cutkosky limits, exact Anselmi–Piva fakeon-cut removal, Compton-bounded acausal precursors ($\boldsymbol{\le (2m^3)^{-1} \int |h''|}$), resummed graviton unitarity ($\boldsymbol{|T| \le 16\pi}$), all-order spectral-recursion unitarity, above-threshold positivity of the non-factorizable two-loop kite discontinuity for both residues $\boldsymbol{r_4 = \pm 1}$ (with a sharp strong-coupling zero obstruction for $\boldsymbol{r_4 = -1}$), and a sharp zero-width distributional dichotomy separating uniform convergence of the subtracted density $\boldsymbol{D_{sub}}$ from an exact half-Breit–Wigner narrow-width pinch $\boldsymbol{\varepsilon S_3 \to r_4^2 L(s)/(256\pi^2 s)}$. Fourth, extending the canonical reciprocal cost $\boldsymbol{J(x) = \frac{1}{2}(x + x^{-1}) - 1}$ to phase ratios derives the dispersion ceiling $\boldsymbol{\Omega_{RS}^2(q) = (4/\ell_0^2)\sin^2(q\ell_0/2) \le 4/\ell_0^2}$ saturated uniquely at $\boldsymbol{\Lambda_{RS} = \pi/\ell_0}$, proves that the continuum one-loop $\boldsymbol{f_0^2}$ Landau pole is a regular point of the ratio flow with bounded $\boldsymbol{J}$-cost and is removed whenever $\boldsymbol{\Lambda_{RS} < \mu_{IR} e^{t_c}}$, and establishes $\boldsymbol{(\ell_0 k/\pi)^2}$ below-ledger linearized decay of both $\boldsymbol{C^3}$ and $\boldsymbol{R^3}$. Every theorem is formally verified in Lean 4 across **65** clean-room-audited modules (**176,246** lines, zero unfinished proofs, standard axioms only) and cross-checked by an independent **46**-test symbolic–numerical suite.

Keywords: Asymptotic safety, functional renormalization group, Goroff–Sagnotti counterterm, higher-derivative gravity, Standard Model matter, generation window, Lee–Wick poles, saddle-node bifurcation, fakeon unitarity, microcausality, discrete curvature ceiling, formal verification

1 Introduction

Quantizing four-dimensional gravity exposes four tightly coupled ultraviolet (UV) obstructions that no single perturbative trick resolves on its own. First, perturbative Einstein–Hilbert gravity is non-renormalizable at two loops: following 't Hooft and Veltman's one-loop analysis [4], Goroff and Sagnotti [1;2] (confirmed independently by van de Ven [3]) established an on-shell non-vanishing curvature-cubed counterterm $\int \sqrt{g}\, C^3$ with coefficient $209/(2880 \cdot 16\pi^2\epsilon)$, forcing an infinite proliferation of higher-dimension couplings unless the renormalization group (RG) flow is controlled by an interacting non-Gaussian UV fixed point—Weinberg's asymptotic safety scenario [18], formulated nonperturbatively through the Wetterich–Morris exact functional renormalization group (FRG) equation [19–24;37;38;40]. Second, adding the quadratic curvature invariants C^2 and R^2 renders the theory perturbatively renormalizable [5;6;17] and asymptotically free in the spin-2 Weyl coupling f_2^2 [7–9;14], yet introduces both a massive spin-2 Ostrogradsky ghost pole in the bare propagator and a finite-scale UV Landau pole in the scalaron coupling f_0^2 that drives the R^2 coefficient tachyonic at high energies [11–13]. Third, coupling gravity to observed Standard Model matter fields strongly reshapes the UV fixed point [41–43;45;48]: scalars destabilize Newton's constant toward a Donà–Eichhorn–Percacci pole $1/g_* = 0$ (constraining Higgs and supersymmetric extensions [44;46;47;51]), while Dirac fermions and gauge vectors control whether the spin-2 propagator acquires an unphysical Euclidean ghost pole, a real Lorentzian Stelle ghost, or a complex-conjugate Lee–Wick / unstable Merlin pair [15;16;52;53;59;65;67;68]. Fourth, projecting out the massive spin-2 ghost via Anselmi and Piva's fakeon (purely virtual particle) prescription [56–58;60] restores perturbative unitarity at one loop, yet requires rigorous multi-loop proof on non-factorizable topologies (where internal fakeon propagators go on shell inside physical Cutkosky cuts [54]) together with an exact analysis of the zero-width distributional limit $\varepsilon \to 0^+$ and microcausality violations [61;62;66].

A recurring vulnerability in quantum-gravity literature is treating numerical root-finding on low-order truncations, heuristic one-loop contour arguments, or single-basin fixed-point scans as settled theorems. Numerical Jacobian diagonalization can miss Jordan-block degeneracies or near/far branch coexistence; single-scheme matter calculations can conflate cutoff artifacts with physical phase boundaries; and formal principal-value manipulations can conceal genuine non-integrable $1/x^2$ pinches above three-particle thresholds. The purpose of this paper is to resolve all four ultraviolet questions with machine-verified mathematical precision in Lean 4 [72;73], establishing positive existence, spectral, bifurcation, unitarity, and ceiling theorems alongside three sharp constructive obstructions.

1.1 Position within the D_4^* and strong-field quantum-gravity program

This work forms the continuum ultraviolet and perturbative-unitarity pillar of the Recognition Science quantum-gravity program [76;77], following our machine-verified strong-field black-hole, nonsingular collapse, and quantum-horizon investigation [77] (and our companion linearized D_4^* lattice graviton study [78]). In Ref. [77], we proved all 16 nonlinear Einstein and Einstein–Maxwell equations across smooth ingoing Kerr and Kerr–Newman horizons, established exact 4D ADM and BMS_4 memory laws, and showed how an effective capacity density ceiling $\rho_c = 3/(8\pi G\ell^2)$ organized around the canonical reciprocal comparison cost

$$J(x) = \frac{1}{2}\left(x + x^{-1}\right) - 1 = \frac{(x-1)^2}{2x}, \qquad x > 0, \tag{1}$$

replaces central collapse singularities with bounded-curvature bounces while exposing sharp inhomogeneous shell-crossing and supercritical no-echo obstructions.

That strong-field paper left open the ultraviolet completion of the gravitational dynamics above the Planck scale and the perturbative unitarity of higher-derivative gravitational propagators. Here we address both directly, while maintaining strict separation between (i) continuum FRG truncations, (ii) perturbative and distributional fakeon amplitudes, and (iii) discrete recognition-ledger phase-comparison geometry. Where an analytical formula enters as an adopted working truncation parameter or structural identification rather than a microscopically derived lattice constant, we mark it explicitly at the point of use and in Section 7.4.

1.2 Summary of main results and sharp obstructions

Our results are organized into four theorem blocks and three decisive obstructions, all formally verified in Lean 4 against `Mathlib`[72;73] across 65 clean-room-audited modules (176,246 lines, zero unfinished proofs, strictly standard axioms [`propext`, `Classical.choice`, `Quot.sound`]; complete theorem-to-module mapping in Section A) and cross-checked by an independent 46-test symbolic–numerical Python/SymPy/SciPy suite (`verify_uv_paper.py`):

1. **Six-coupling $R^3 + C^3$ FRG completion and Jordan-block-free spectral stability (Section 3).** Extending the bidirectional Stelle–Litim FRG flow sequentially from four couplings $(\widetilde{G}, \widetilde{\Lambda}, f_2^2, f_0^2)$ through five couplings adding the Goroff–Sagnotti operator C^3 to six rescaled couplings $(\widehat{G}, \lambda, \widehat{a}, \widehat{b}, \widehat{c}, \widehat{d})$ retaining *both* independent dimension-six curvature cubes C^3 and R^3, we prove via Banach contraction the existence, local uniqueness on 10^{-4} balls, and Fréchet stability of five distinct non-Gaussian fixed points (Theorem 3.2): pure gravity and both Far and Near physical branches for the Minimal Standard Model $(N_S, N_D, N_V) = (4, 45/2, 12)$ and the three-generation SM $+ 3\nu_R$ benchmark $(4, 24, 12)$. Using explicit 6×6 Laplace determinant algebra, we prove complete complex characteristic-polynomial factorization $\det(zI_6 - \mathcal{M}_6) = \prod_{i=1}^{6}(z - e_i)$ into six pairwise distinct eigenvalues—ruling out defective Jordan blocks—and prove mutual exclusion of the three certified spectral shapes (Theorem 3.3): $4 + 2$ with a complex-conjugate pair ($\theta \approx 2.5363 \pm 1.8789i$) for pure gravity, all-real $3+3$ (making R^2 UV-irrelevant) on both matter Far branches, and all-real $4+2$ on both matter Near branches. At all five fixed points, *both* dimension-six operators are strictly UV-irrelevant with $\theta_{C^3} \in (-2.009, -2.0003)$ and $\theta_{R^3} \in (-2.024, -2.014)$ (Theorem 3.4). Setting the R^3 source to zero recovers all nine certified five-coupling fixed points conservatively across both Type I and Type II matter cutoffs, establishing that *both* $4 + 1$ Near and $3 + 2$ Far branches coexist under *both* cutoff types.
2. **Matter phase boundaries, the $2 \le N_{\rm gen} \le 7$ generation window, Lee–Wick poles, and the double-fold S-curve catastrophe (Section 4).** In an independent first-principles Litim-integral five-coupling FRG system $(u_0, u_1, u_2, u_C, \sigma)$ verified directly from Lebesgue integrals with exact one-loop benchmarks (Christensen–Duff 53/45, Ricci-flat fourth-order $C^2 + E_4$ coefficient $+413/180 = 133/20 - 196/45$, 4D Gauss–Bonnet topological invariance E_4, and Cardy conformal anomaly ratios $a_D/a_S = 11$, $a_V/a_S = 62$) and continuous ghost/matter cutoff homotopy $s \in [0, 1]$ (Type II to Pure Type I), affine-interval continuation certifies: (a) exact Donà–Eichhorn–Percacci scalar poles $1/g_* = 0$ at $N_S^{\rm pole} \in (40, 41)$ (SM, ≈ 40.08) and $(41, 42)$ (SM $+ 3\nu_R$, ≈ 41.45) at Pure Type I—admitting Minimal Higgs ($N_S = 4$) while excluding the MSSM ($N_S = 49$)—and at $N_S^{\rm pole} \in (7, 8)$ (SM $+ 3\nu_R$, ≈ 7.56) and $(10, 11)$ (SM, ≈ 10.87) at Type II, already excluding two-Higgs-doublet models ($N_S = 8$) at Type II (Theorem 4.1); (b) a fermion-induced Euclidean spin-2 ghost-freedom transition $N_D^{\rm ghost} \in (9, 37/4)$ (≈ 9.093 at $N_S = 4$) and an exact ghost-free asymptotic-safety generation window $N_{\rm gen} \in \{2, 3, 4, 5, 6, 7\}$ ($N_D = 8N_{\rm gen}$), bounded on both sides by Euclidean spin-2 ghost poles at $N_{\rm gen} = 1$ and $N_{\rm gen} = 8$ (Theorem 4.2), while matter simultaneously stabilizes pure gravity's near-singular mass-matrix eigenvalue ($\theta_5 \approx -723.6$ at $s = 0$, -301.1 at $s = 1$) down to clean $O(1)$ spectra; (c) an exact complex-p^2 pole trichotomy with a Stelle-to-Lee–Wick exceptional point $N_D^{\rm LW} \in (10, 51/5)$ (≈ 10.101), proving that both SM and SM $+ 3\nu_R$ lie uniformly across all $s \in [0, 1]$ in Phase III (complex-conjugate Lee–Wick/fakeon pair, $\Delta_{\rm TT} < -100$, globally positive $P_{\rm TT}(z) > 0$ on all $z \in \mathbb{R}$) alongside a physical Starobinsky scalaron pole (Theorem 4.4); and (d) a global smooth S-curve manifold over $u_C \in [-6, 11]$ with two exact saddle-node folds ($\det JV_5 = 0$), an upper fold F_1 at $u_C \in (13/2, 9)$ (≈ 7.769), $N_D^{F_1} \in (56.85, 57)$ (≈ 56.920) capping $N_{\rm gen} \le 7$, a lower fold F_2 at $u_C \in (-9/4, -5/4)$ (≈ -1.808), $N_D^{F_2} \in (42, 42.5)$ (≈ 42.335), and *triple fixed-point coexistence* at $N_{\rm gen} = 7$ (Theorem 4.5).
3. **Perturbative, all-order, and zero-width distributional fakeon unitarity (Section 5).** At arbitrary loop order, we prove parametric Cutkosky convergence[54], the arbitrary-n-vertex Veltman largest-time equation[55], exact Anselmi–Piva fakeon-cut removal (Im $= 0$ for all $\varepsilon \neq 0$), the two-loop sunset Cauchy–Schwarz threshold identity $s > (m_1 + m_2 + m_3)^2$, a rigorous Compton-scale microcausality precursor bound $|R_F - R_{\rm ret}| \le (2m^3)^{-1} \int |h''|$ (Theorem 5.1), resummed graviton elastic unitarity $|T| \le 16\pi$ contrasted against Feynman-ghost unitarity violation, and all-order inductive spectral-recursion unitarity (Theorem 5.2). On the non-factorizable two-loop kite graph,

we prove exact 4-cut combinatorics, above-threshold AP continuation of both triangle and three-body sub-amplitudes, and positivity of the unitarity-complete discontinuity $D(s,\varepsilon) > 0$ for both fakeon residues $r_4 = \pm 1$, paired with **Obstruction I** (a sharp strong-coupling zero at $g^2 = 32\pi^2/V_{\rm AP}(s,\varepsilon)$ for $r_4 = -1$ on $(m^2, 4m^2]$; Theorem 5.3). Resolving the zero-width limit $\varepsilon \to 0^+$ yields Theorem 5.4 and **Obstruction II**: while the subtracted density $D_{\rm sub} = D - g^4 S_3$ converges uniformly under every bounded test weight through and above $(m+M)^2$, the pure fakeon square $S_3 = \int d\Phi_3 (A_R^{\rm AP})^2$ develops a non-removable half-Breit–Wigner narrow-width pinch $\varepsilon S_3(s,\varepsilon) \to r_4^2 L(s)/(256\pi^2 s) > 0$ along the Dalitz chord $\{P(u) < 0\}$ (explicit witness $m = 1, M = 2, s = 10$: $L = 9/4$, $\varepsilon D(10,\varepsilon) \to 9/(10240\pi^2)$), proving that above-threshold unitarity statements must retain finite fakeon width $\varepsilon = M\Gamma$.

4. **UV-to-IR Stelle trajectories, Obstruction III (one-loop f_0^2 Landau pole), and the RS discrete J-cost ceiling (Section 6).** Solving the one-loop quadratic-gravity RG flow via an exact first integral ($r_\pm = (-1098 \pm \sqrt{1{,}185{,}604})/400$, approach exponent $p = \sqrt{1{,}185{,}604}/798 \approx 1.3645$), we establish **Obstruction III**: every continuum one-loop trajectory with $f_2^2(\mu_{\rm IR}), f_0^2(\mu_{\rm IR}) > 0$ hits an unavoidable finite-scale f_0^2 Landau pole at $t_c \le y(0)/c_{\rm floor}$ and turns tachyonic ($y < 0$). Extending the canonical cost Eq. (1) to complex phase ratios $z = e^{iq\ell_0}$ derives the discrete ledger dispersion symbol $\Omega_{\rm RS}^2(q) = -(2/\ell_0^2)\,\mathrm{Re}\, J_{\mathbb{C}}(e^{iq\ell_0}) = (4/\ell_0^2)\sin^2(q\ell_0/2)$, proving it matches continuum q^2 to $(5/48)\ell_0^2 q^4$ for $|q\ell_0| \le 1$ while attaining its unique maximum $4/\ell_0^2$ at the zone edge $\Lambda_{\rm RS} = \pi/\ell_0$ (Theorem 6.2). We then prove that the Landau pole is a regular point $x_c = -r_-/(r_+ - r_-) \approx 1.0042 > 1$ of the ratio flow with bounded comparison cost $J(x(t)) \le J(x(0))$, that all couplings remain positive and explicitly bounded across the entire ledger $[0, \Lambda_{\rm RS}]$ if and only if $\Lambda_{\rm RS} < \mu_{\rm IR} e^{t_c}$ (Theorem 6.3), and that below $\Lambda_{\rm RS}$ the linearized flows at the three primary six-coupling benchmark fixed points (pure gravity, Minimal SM Far, and SM$+3\nu_R$ Far; and identically at the Near points by $\theta_{C^3}, \theta_{R^3} < -2$) suppress both dimension-six modes (C^3, R^3) at least as $(\ell_0 k/\pi)^2$ while leaving the matter Far R^2 mode slowly decaying with exponent $r_4 \in (0.1597, 0.2060)$ (Theorem 6.4).

1.3 Explicit scope boundaries

Keeping proved theorems cleanly separated from open physics requires stating exact boundaries upfront (detailed further in Section 7.4):

1. *Finite FRG truncations and working coupling coefficients.* Both FRG architectures are finite-dimensional truncations (five and six curvature invariants) in fixed harmonic / Landau–DeWitt gauges and Litim-class regulators. In Architecture A, the gravitational saturation parameters $P_5 = (\eta, \kappa, \widehat{a}_s, \widehat{b}_s, A_3, B_3, \zeta) = (1/5, 1/2, 2/133, 1/50, 1, 1, 1)$ and the R^3 couplings $(A_3^R, B_3^R, \zeta^R) = (1,1,1)$ are adopted working inputs rather than evaluated from an untruncated Wetterich trace; Architecture B evaluates its heat-kernel and Litim threshold integrals from first principles with zero free gravitational parameters yet omits R^3 and higher-curvature operators beyond dimension six.
2. *Distinctness of the two FRG architectures.* We never conflate Architecture A (which exhibits both Near $4+2$ and Far $3+3$ branches on the same matter flow) with Architecture B (which exhibits the global double-fold S-curve and $2 \le N_{\rm gen} \le 7$ window). Whether their near/far bifurcation structure is connected by a continuous regulator deformation remains open.
3. *Perturbative vs. nonperturbative unitarity.* Our fakeon unitarity theorems cover arbitrary-vertex Veltman largest-time identities, arbitrary-order melon/sunset spectral-recursion chains, and the non-factorizable two-loop kite with scalar cubic vertices; general multi-loop anomalous-threshold Landau topologies, graviton tensor numerators beyond scalar-skeleton cuts, and nonperturbative Lorentzian unitarity remain open.
4. *Nonlinear below-ledger flow and Hadamard finite part.* Below-ledger $(\ell_0 k/\pi)^2$ decay of C^3 and R^3 is formally proved for the certified linearized flow (the uniform nonlinear quadratic remainder bound is explicitly left open), and the cumulative Hadamard finite part PV $\int (1/f_- - 1/f_+)$ of the subtracted kite square remains open.

Table 1 Globally disambiguated nomenclature used across Architecture A (six-coupling FRG), Architecture B (first-principles Litim-integral five-coupling FRG), perturbative fakeon unitarity, and the discrete phase-comparison ledger ceiling.

Symbol	Meaning / Definition	Domain / Value
$J(x)$, $J_{\mathbb{C}}(z)$	Canonical reciprocal cost $\frac{1}{2}(x+x^{-1})-1$; complex $\frac{1}{2}(z+z^{-1})-1$	$x>0$, $z\in\mathbb{C}^{\times}$
ℓ_0, Λ_{RS}, q, $\Omega^2_{\mathrm{RS}}(q)$	Recognition ledger length, cutoff $\Lambda_{\mathrm{RS}}=\pi/\ell_0$, wavenumber q, dispersion $(4/\ell_0^2)\sin^2(q\ell_0/2)$	$\ell_0>0$, $\Omega^2_{\mathrm{RS}}(\Lambda_{\mathrm{RS}})=4/\ell_0^2$
k, t	Renormalization group momentum scale and RG time $t=\ln(k/\mu_{\mathrm{IR}})$	$k>0$, $t\in\mathbb{R}$
$\widetilde{G}$, $\widetilde{\Lambda}$, f_2^2, f_0^2	Dimensionless Newton, cosmological, Weyl^2 ($\alpha=-\frac{1}{2f_2^2}$), and R^2 ($\beta=\frac{1}{6f_0^2}$) couplings	Physical Stelle/FRG units
$\widehat{G}$, λ, $\widehat{a}$, $\widehat{b}$, $\widehat{c}$, $\widehat{d}$	Rescaled 6-coupling coordinates: $\widehat{G}=\widetilde{G}/\pi$, $\lambda=\widetilde{\Lambda}$, $\widehat{a}=f_2^2/(16\pi^2)$, $\widehat{b}=f_0^2/(16\pi^2)$, $\widehat{c}$ (C^3), $\widehat{d}$ (R^3)	Architecture A (Sec. 3)
v_2, v_0, w_2, w_0, ϖ_0	Inverse Stelle mass ratios $v_2=\widehat{G}/\widehat{a}$, $v_0=\widehat{G}/\widehat{b}$; reduced $w_s=1/v_s$; regulator mass ϖ_0	$v_s, w_s>0$
$\mathcal{M}_6$, $\theta_i=-e_i$	Six-coupling stability matrix $\partial\widehat{\beta}_6/\partial x$ and critical exponents (minus eigenvalues)	$\mathrm{Re}\,\theta_i>0$ UV-relevant
$u=(u_0,u_1,u_2,u_C,\sigma)$	Action couplings in Architecture B: $g=-\pi/u_1$, $\lambda=-u_0/(2u_1)$, $u_2[R^2]$, $u_C[C^2]$, $\sigma[C^3]$	Architecture B (Sec. 4)
$s_{\mathrm{cut}}\in[0,1]$	Endomorphism-dressed ghost/matter cutoff homotopy parameter (denoted s in Sec. 4)	0: Type II, 1: Pure Type I
(N_S,N_D,N_V), N_{gen}	Massless real scalars, Dirac fermions, gauge vectors; generation count $N_D=8N_{\mathrm{gen}}$	SM $(4,\frac{45}{2},12)$; RS3 $(4,24,12)$
$P_{\mathrm{TT}}(u,z)$, Δ_{TT}	Spin-2 inverse propagator $u_Cz^2-\frac{1}{2}u_1z-\frac{1}{2}u_0$; discriminant $\frac{1}{4}u_1^2+2u_Cu_0$	$\Delta_{\mathrm{TT}}<0$: Lee–Wick Phase III
F_1, F_2	Upper and lower saddle-node folds of global S-curve $N_D(u_C)$ ($\det JV_5=0$)	$N_D^{F_1}\approx 56.92$, $N_D^{F_2}\approx 42.34$
m, M, r_4, ε, $h(t)$	Scalaron mass, fakeon mass ($0<m<M$), residue $r_4=\pm1$, width $\varepsilon=M\Gamma$, classical source h	Perturbative fakeon sector
s, Φ_2, Φ_3, $D(s,\varepsilon)$	Mandelstam energy squared $s=p^2$, 2-/3-body phase spaces, complete cut density	Sec. 5
D_{sub}, S_3, $L(s)$, K_{pinch}	Subtracted density $D-g^4S_3$, fakeon square, pinch-chord length, narrow-width residue	Witness $L(10)=9/4$
$\ell(t)$, ℓ_{IR}, $y(t)$, $\rho(t)$	One-loop $f_2^2(t)$, IR datum $f_2^2(\mu_{\mathrm{IR}})$, $y=1/f_0^2$, Codello–Percacci ratio $\rho=\ell y/2$	Fixed ratios $r_-<r_+<0$
t_c, x_c	One-loop f_0^2 Landau pole scale ($y(t_c)=0$) and ratio coordinate $x_c=-r_-/(r_+-r_-)$	$x_c\approx 1.0042>1$

1.4 Conventions and nomenclature

Throughout the FRG sections (Sections 3 and 4), we work in four-dimensional Euclidean signature $(+,+,+,+)$ matching standard Wetterich-equation conventions[21;27], whereas Lorentzian signature $(-,+,+,+)$ is used in complex-p^2 pole analysis (Section 4) and perturbative fakeon S-matrix amplitudes (Section 5), matching Ref.[77]. To prevent any collision across the two FRG coordinate systems, one-loop Stelle couplings, fakeon kinematics, and discrete ledger variables, Table 1 fixes all symbols uniquely across the manuscript.

2 Canonical reciprocal cost, dual FRG architectures, and formal methodology

Before stating and proving the main theorems of Sections 3 to 6, we summarize the three unifying structures that organize this study: the Recognition Science reciprocal cost and matter benchmarks, the exact relationship between our two complementary FRG architectures, and the machine-verified interval-contraction and spectral-factorization methodology.

2.1 Recognition Science grounding and benchmark matter spectra

In the Recognition Science (RS) foundation[74–76], comparing any positive physical ratio $x\in\mathbb{R}_{>0}$ carries the unique dimensionless cost functional Eq. (1), selected by zero cost at balance ($J(1)=0$), reciprocal symmetry ($J(x)=J(x^{-1})$), unit curvature ($J''(1)=1$), and multiplicative d'Alembert composition

$J(xy) + J(xy^{-1}) = 2J(x)J(y) + 2J(x) + 2J(y)$. Across this ultraviolet study, this structure enters at three distinct, clearly labeled levels:

1. *Derived complex phase-ratio dispersion ceiling (Section 6).* Evaluating the analytic continuation $J_{\mathbb{C}}(z) = \frac{1}{2}(z + z^{-1}) - 1$ on the phase ratio $z = e^{iq\ell_0}$ between adjacent ledger cells of spacing $\ell_0 > 0$ yields $J_{\mathbb{C}}(e^{iq\ell_0}) = \cos(q\ell_0) - 1$, bounding the link comparison cost strictly to $[-2, 0]$ and deriving directly the dispersion symbol $\Omega^2_{\mathrm{RS}}(q) = (4/\ell_0^2)\sin^2(q\ell_0/2)$ with its unique maximum $4/\ell_0^2$ at the zone edge $\Lambda_{\mathrm{RS}} = \pi/\ell_0$.
2. *Working structural identification for the fakeon Green function (Section 5).* Writing $x = e^u$ turns Eq. (1) into $J(e^u) = \cosh u - 1 = \mathrm{evenPart}(\exp)(u) - 1$. Applying the same even projection $\mathrm{evenPart}(f)(t) = \frac{1}{2}(f(t) + f(-t))$ to the retarded oscillator Green function $G_{\mathrm{ret}}(\omega, t) = \theta(t)\sin(\omega t)/\omega$ reproduces the Anselmi–Piva fakeon Green function $G_F(\omega, t) = \sin(\omega|t|)/(2\omega)$ identically. In strict accordance with our formal source documentation (Section A), we classify this parallel as a *working structural identification* of shared even-projection symmetry rather than a microscopic derivation of fakeon quantization from $J(x)$.
3. *Standard Model and* SM + $3\nu_R$ *benchmark matter spectra (Sections 3 and 4).* We evaluate every matter-coupled theorem on two physical benchmark spectra: the Minimal Standard Model $(N_S, N_D, N_V)_{\mathrm{SM}} = (4, 45/2, 12)$ (one real Higgs doublet, 45 Weyl fermions, 12 gauge bosons) and the complete three-generation neutrino-extended spectrum

$$(N_S, N_D, N_V)_{\mathrm{RS3}} = (4,\ 24,\ 12) \qquad (\mathrm{SM} + 3\nu_R), \tag{2}$$

together with general integer generation scans $N_D = 8N_{\mathrm{gen}}$ ($N_{\mathrm{gen}} = 1, \ldots, 8$, where each complete generation carries 16 Weyl = 8 Dirac fermion states). Within Recognition Science[76], the 8 Dirac states per generation reflect $2^D = 8$ binary configurations in $D = 3$ spatial dimensions (and 24-cell D_4^* fourth-rank spherical 5-design isotropy on S^3); throughout our proofs, however, $(4, 45/2, 12)$, $(4, 24, 12)$, and $(4, 8N_{\mathrm{gen}}, 12)$ enter purely as exact rational matter multiplicities, requiring no external assumptions on gauge-group unification.

2.2 Two complementary FRG architectures: why both are needed

A central methodological strength of this paper is the deployment of *two independent, complementary FRG architectures* whose proven domains reinforce one another without circularity:

- **Architecture A (Sections 3 and 6):** A bidirectional Stelle–Litim flow in harmonic gauge parameterized in rescaled couplings $(\widehat{G}, \lambda, \widehat{a}, \widehat{b}, \widehat{c}, \widehat{d})$ that retains *both* dimension-six curvature cubes C^3 and R^3 simultaneously. Its role is to certify the six-coupling UV fixed points, prove Jordan-block-free 6×6 spectral factorization, establish Near $(4 + 2)$ vs. Far $(3 + 3)$ branch coexistence under both Type I and Type II cutoffs, and link directly to the one-loop Stelle flow and the discrete ledger ceiling $\Lambda_{\mathrm{RS}} = \pi/\ell_0$.
- **Architecture B (Section 4):** A first-principles Lebesgue-integral Wetterich flow in Landau–DeWitt gauge parameterized in action couplings $u = (u_0, u_1, u_2, u_C, \sigma)$ $(1, R, R^2, C^2, C^3)$ with zero free gravitational tuning parameters, exact one-loop benchmarks (53/45 and +413/180), exact 4D Gauss–Bonnet topological invariance, derived Cardy anomaly ratios $1 : 11 : 62$, and a continuous cutoff homotopy $s \in [0, 1]$. Its role is to map the global matter phase diagram, certify the exact Donà–Eichhorn–Percacci scalar poles, prove the $2 \le N_{\mathrm{gen}} \le 7$ ghost-free generation window, classify the complex-p^2 Lee–Wick propagator poles, and trace the global double-fold S-curve catastrophe (F_1, F_2) across $u_C \in [-6, 11]$.

Keeping the two architectures strictly disambiguated guarantees that readers can verify every theorem on its own equations without ever blurring working parameters of Architecture A with first-principles integral derivations of Architecture B.

2.3 Formal verification standard: Banach contraction, affine-interval slopes, and 6×6 spectral algebra

Every theorem in this paper is machine-verified in Lean 4 against `Mathlib`[72;73] with zero unfinished proofs (`0 sorry`), zero custom axioms, and strictly standard foundations

[propext, Classical.choice, Quot.sound]. To keep the main physics exposition clean and timeless, exact Lean 4 module paths and declaration names are organized in the complete reproducibility ledger of Section A. Four formal techniques recur across the 65 audited modules:

1. *Preconditioned Banach contraction.* For each fixed point of Architecture A, we reduce $\beta(\mathbf{x}) = 0$ analytically to a three-variable map $T_{\mathrm{red}}(\lambda, w_2, w_0)$ (slaving $\widehat{G}, \widehat{c}, \widehat{d}$ exactly) and apply a preconditioned Newton operator $N(p) = p - A(p - T_{\mathrm{red}}(p))$ on closed balls of radius 10^{-12} (existence and 12-digit enclosure) and 10^{-4} (local uniqueness), proving exact Lipschitz contraction constants $K < 1$ via rational interval-slope arithmetic.
2. *First-order affine-interval continuation.* For the global cutoff homotopy $s \in [0, 1]$, scalar-pole continuations, fermion-transition curves, and the 45-subinterval global S-curve over $u_C \in [-6, 11]$ in Architecture B, exact first-order affine enclosures $\hat{a}(\tau) = c_0 + c_1\tau \pm \delta$ ($\tau \in [-1, 1]$) preserve linear correlations across Newton steps and certify continuous, locally unique implicit curves $u^*(\tau)$ with exact Fréchet Jacobians.
3. *Jordan-block-free* 6×6 *characteristic-polynomial factorization.* Explicit recursive Laplace expansions of 5×5 and 6×6 determinants enable exact rational enclosure of $\det(tI_6 - \mathcal{M}_6)$ without symbolic explosion. Six pairwise distinct eigenvalues (certified via intermediate-value sign changes and exact quadratic deflation for complex pairs) force the monic characteristic polynomial over $\mathbb{C}$ to factor completely as $\det(zI_6 - \mathcal{M}_6) = \prod_{i=1}^{6}(z - e_i)$, mathematically excluding defective Jordan blocks and guaranteeing exact eigenvalue multiplicity counting. Nonsingularity of the deleted 5×5 minor then proves that every eigenvector of a given eigenvalue carries a nonzero component along the corresponding curvature operator $(\widehat{b}, \widehat{c}, \widehat{d})$.
4. *Measure-theoretic Cutkosky and distributional limits.* All threshold integrals in Sections 4 and 5 are proved using Lebesgue/Bochner integration, the fundamental theorem of calculus, and the Lebesgue dominated convergence theorem, ensuring that zero-width convergence and narrow-width divergence are separated without heuristic interchange of limits.

3 Six-coupling $R^3 + C^3$ functional renormalization group and Jordan-block-free spectral stability

A decisive test of asymptotic safety is whether adding the two-loop Goroff–Sagnotti counterterm $\int \sqrt{g}\, C^3$ [1;2] together with the independent dimension-six curvature cube $\int \sqrt{g}\, R^3$ introduces new ultraviolet-relevant directions that would destroy predictivity [25;26;28–34;36]. In this section we establish the complete Architecture A hierarchy (with all formal Lean 4 theorem-to-module correspondences recorded in Section A): from exact fourth-order Stelle–Litim threshold integrals through bidirectional four- and five-coupling flows and derived Type I / Type II matter shifts to five Banach-certified, Jordan-block-free six-coupling fixed points in which *both* C^3 and R^3 remain strictly UV-irrelevant ($\theta_{C^3}, \theta_{R^3} < -2$).

3.1 Stelle–Litim threshold integrals and the one-loop a_3 vanishing lemma

In the fourth-order Stelle kinetic profile with inverse mass-squared ratio $v = 16\pi\widetilde{G}/f_s^2 > 0$ (so $v_2 = \widehat{G}/\widehat{a}$ for the spin-2 Weyl sector and $v_0 = \widehat{G}/\widehat{b}$ for the spin-0 scalaron sector), the dimensionless kinetic polynomial is $P_v(z) = z + vz^2$, regulated by the optimized fourth-order Litim cutoff [23;24] $R_v(z) = \big((1+v) - (z+vz^2)\big)\theta(1-z)$. For $z \in (0, 1)$, the regularized denominator is constant, $P_v(z) + R_v(z) + \varpi_0 = 1 + v + \varpi_0$, while the full scale-derivative numerator (before dividing by $2Zk^2$) is

$$N_v^{\mathrm{full}}(z) = 2(1 + 2v) - \eta_N(1 - z) - \eta_f v(1 - z^2). \tag{3}$$

Dividing by 2 yields the standardized threshold numerator $N_v(z) = (1+2v) - \frac{1}{2}\eta_N(1-z) - \frac{1}{2}\eta_f v(1-z^2)$, whose one-loop ($\eta_N = \eta_f = 0$) limit is the constant $N_v^{(0)}(z) := (r_1 - zr_1') + v(2r_2 - zr_2') = 1 + 2v$ on $z \in (0, 1)$. Evaluating the elementary Lebesgue threshold integrals $\Phi_p^n[v](\varpi_0) = \frac{1}{\Gamma(n)} \int_0^1 z^{n-1} N_v^{(0)}(z)/(1 + v + \varpi_0)^p\, dz$ and the η-weighted companion integrals $\widetilde{\Phi}_p^n[v](\varpi_0)$ directly yields the exact closed-form

rational building blocks with $D(v,\lambda) := 1 + v - 2\lambda$:

$$G_1(v,\lambda) = \frac{(1+2v)(-4-7v-10\lambda)}{D^2}, \qquad G_2(v,\lambda) = -\frac{1+v+10\lambda}{2D^2},$$
$$G_3(v,\lambda) = \frac{v\left(-\frac{7}{12} - \frac{11}{15}v - \frac{10}{3}\lambda\right)}{D^2}, \qquad V_1(v,\lambda) = \frac{1+2v}{2D}, \tag{4}$$
$$V_2(v,\lambda) = \frac{1}{12D}, \qquad V_3(v,\lambda) = \frac{v}{8D}, \tag{5}$$

together with the quadratic-coupling threshold $T(v,\lambda) = v(1+2v)/(2D^2)$ and the one- and three-insertion dimension-six thresholds

$$\Phi_2^2(v,\lambda) = \frac{1+2v}{2D^2}, \qquad \Phi_4^4(v,\lambda) = \frac{1+2v}{24D^4} = \frac{\Phi_2^2(v,\lambda)}{12D^2}. \tag{6}$$

In the inverted Stelle mass ratios $w = 1/v = m^2/k^2 > 0$, writing $\Delta(w,\lambda) := 1 + w(1-2\lambda)$, every threshold remains rational and smooth down to $w = 0$: for example, $T(1/w,\lambda) = (2+w)/(2\Delta^2)$ and $\Phi_2^2(1/w,\lambda) = w(2+w)/(2\Delta^2) = wT(1/w,\lambda)$. At $v = 0$ ($w \to \infty$), Eq. (4)–Eq. (5) reduce identically to Reuter's harmonic-gauge Einstein–Hilbert thresholds $G_1(0,\lambda) = (-4-10\lambda)/(1-2\lambda)^2$ and $G_2(0,\lambda) = -(1+10\lambda)/(2(1-2\lambda)^2)$.

Lemma 3.1 (Vanishing one-loop ($\eta_N = \eta_f = 0$) Litim a_3 source)**.** *In the one-loop threshold regime ($\eta_N = \eta_f = 0$), for every $v, \varpi_0 \in \mathbb{R}$, $p \in \mathbb{N}$, and $z \in (0,1)$, the standardized halved Litim threshold integrand*

$$W^{(0)}_{v,\varpi_0,p}(z) := \frac{N_v^{(0)}(z)}{\left(P_v(z) + R_v(z) + \varpi_0\right)^p}$$

is identically equal to the constant $(1+2v)/(1+v+\varpi_0)^p$. Consequently, $\frac{d}{dz}W^{(0)}_{v,\varpi_0,p}(z) = 0$ throughout $(0,1)$, so the one-loop heat-kernel a_3 functional $Q_{-1}[W^{(0)}] = -(W^{(0)})'(0^+) = 0$ vanishes identically on both the spin-2 (v_2) and spin-0 (v_0) lines.

Proof. On $0 < z < 1$, the indicator $\theta(1-z)$ equals 1 on the open neighborhood $(0,1)$ of z, so $P_v(y) + R_v(y) + \varpi_0 = 1 + v + \varpi_0$ and $N_v^{(0)}(y) = 1 + 2v$ identically on $(0,1)$. Since a locally constant function has zero derivative, $\frac{d}{dz}W^{(0)}_{v,\varpi_0,p}(z) = 0$ everywhere on $(0,1)$, hence $Q_{-1}[W^{(0)}] = 0$. □

Note carefully the exact scope of Theorem 3.1 and its relationship to Architecture B (Section 4.1). The vanishing $Q_{-1}[W^{(0)}] = 0$ holds strictly at $\eta_N = \eta_f = 0$—that is, in the one-loop threshold regime and identically for minimally coupled massless matter fields whose anomalous dimensions vanish. Whenever gravitational anomalous dimensions are nonzero ($\eta_N \neq 0$, as at any non-Gaussian fixed point with $\eta_N = -2$), the $-\frac{1}{2}\eta_N(1-z)$ piece of Eq. (3) is linear in z and generates a non-vanishing derivative $W'(0^+) \propto \eta_N$. Architecture A models the dimension-six beta functions Eq. (21) purely via three-curvature insertions Φ_4^4 on the fourth-order propagators (omitting the η_N-proportional Q_{-1} source), whereas Architecture B retains the exact non-vanishing $Q_{-1}[W] = (2A_1 + \dot{A}_1)/D = -\eta_N A_1/D$ directly from the fourth-order Wetterich trace in Eq. (27).

3.2 Derived matter shifts and the Type I versus Type II Newton-shift gap

For N_S minimally coupled real scalars, N_D Dirac fermions, and N_V gauge vectors regulated by the second-order Litim cutoff $R_k(z) = (k^2 - z)\theta(k^2 - z)$, differentiating $t \mapsto R_{e^t}(z)$ at $t = 0$ gives $\partial_t R_k(z) = 2\theta(1-z)$, so the matter threshold integrand $W(z) = \partial_t R_k(z)/(z + R_k(z))$ equals 2 on $(0,1)$ and 0 on $(1,\infty)$. Direct Lebesgue integration on $(0,\infty)$ proves the exact threshold moments

$$Q_2[W] = \int_0^\infty zW(z)\,dz = 1, \qquad Q_1[W] = \int_0^\infty W(z)\,dz = 2,$$
$$Q_0[W] = \lim_{z\to 0^+} W(z) = 2, \qquad Q_{-1}[W] = 0, \tag{7}$$

together with the one-insertion moment $Q_2[W_2] = \int_0^\infty z\,\partial_t R_k/(z+R_k)^2\,dz = 1$. The statistics-weighted Euclidean heat-kernel traces $(t_0, t_2^{\rm II}, t_{4C}, t_{4R})$ per species are:

$$\begin{aligned} \text{Real scalar } (-\nabla^2): &\quad \left(\tfrac{1}{2},\ \tfrac{1}{12},\ \tfrac{1}{240},\ \tfrac{1}{144}\right), \\ \text{Dirac fermion } (\not{D}^2 = -\nabla^2 + \tfrac{1}{4}R): &\quad \left(-2,\ \tfrac{1}{6},\ \tfrac{1}{40},\ 0\right), \\ \text{Feynman-gauge vector } (-\nabla^2 + \mathrm{Ric} - 2\,\text{ghosts}): &\quad \left(1,\ -\tfrac{1}{3},\ \tfrac{1}{20},\ 0\right). \end{aligned} \tag{8}$$

Conformal invariance of massless Dirac fermions and 4D gauge vectors fixes $t_{4R} = 0$ identically, leaving minimally coupled scalars as the sole matter source in the R^2 row. Contracting Eq. (7) with Eq. (8) yields exact rational matter shifts for the vacuum sum ΔS, the Newton-anomalous-dimension coefficient Δb_1, the Weyl-squared coefficient c_W, and the minimally coupled R^2 coefficient c_0:

$$\Delta S(N_S, N_D, N_V) = \frac{N_S - 4N_D + 2N_V}{2}, \quad c_W(N_S, N_D, N_V) = \frac{N_S + 6N_D + 12N_V}{60}, \quad c_0(N_S) = \frac{N_S}{12}, \tag{9}$$

$$\Delta b_1^{\rm II}(N_S, N_D, N_V) = \frac{N_S + 2N_D - 4N_V}{6}, \quad \Delta b_1^{\rm I}(N_S, N_D, N_V) = \frac{N_S - N_D - N_V}{6}. \tag{10}$$

Here Type II regulates $\not{D}^2 = -\nabla^2 + R/4$ and $-\nabla^2 + \mathrm{Ric}$ directly, whereas Type I regulates the bare Laplacian $-\nabla^2$ and expands the endomorphisms $E = R/4$ and $E = \mathrm{Ric}$ out of the propagator via $Q_1 \sum N t_{2,\rm bare} - Q_2[W_2] \sum N t_E$ (with $t_2^{\rm II} = t_{2,\rm bare} - t_E$ identically). Subtracting the two expressions in Eq. (10) yields the exact cutoff-scheme gap:

$$\Delta b_1^{\rm II} - \Delta b_1^{\rm I} = \frac{N_D - N_V}{2}, \tag{11}$$

which vanishes if and only if $N_D = N_V$. For our two benchmark matter contents, the derived shifts are:

$$\begin{aligned} \text{Minimal SM } (4, \tfrac{45}{2}, 12): &\quad \Delta S = -31,\ \ \Delta b_1^{\rm II} = \tfrac{1}{6},\ \ \Delta b_1^{\rm I} = -\tfrac{61}{12}, \\ &\quad c_W = \tfrac{283}{60},\ \ c_0 = \tfrac{1}{3},\ \ \Delta b_1^{\rm II} - \Delta b_1^{\rm I} = \tfrac{21}{4}; \end{aligned} \tag{12}$$

$$\begin{aligned} \text{RS3 SM} + 3\nu_R\ (4, 24, 12): &\quad \Delta S = -34,\ \ \Delta b_1^{\rm II} = \tfrac{2}{3},\ \ \Delta b_1^{\rm I} = -\tfrac{16}{3}, \\ &\quad c_W = \tfrac{73}{15},\ \ c_0 = \tfrac{1}{3},\ \ \Delta b_1^{\rm II} - \Delta b_1^{\rm I} = 6. \end{aligned} \tag{13}$$

In particular, all four matter flows ($\{\mathrm{SM}, \mathrm{RS3}\} \times \{\text{Type I}, \text{Type II}\}$) are formally proved pairwise distinct functions on coupling space: c_W separates SM (283/60) from RS3 (73/15) at $x = (1,1,1,1,1)$, while $\Delta b_1^{\rm II} \neq \Delta b_1^{\rm I}$ separates the two cutoff types at each certified Type II Near fixed point (where $\widehat{G}_* > 0$ and $1 - \widehat{G}_* b_2 > 1$).

3.3 The bidirectional six-coupling flow $\widehat{\beta}_6$ and reduced fixed-point map

Passing to rescaled coordinates $x = (\widehat{G}, \lambda, \widehat{a}, \widehat{b}, \widehat{c}, \widehat{d}) \in \mathbb{R}^6$ with $\widehat{G} = \widetilde{G}/\pi$, $\lambda = \widetilde{\Lambda}$, $\widehat{a} = f_2^2/(16\pi^2)$, and $\widehat{b} = f_0^2/(16\pi^2)$ removes all explicit factors of π while preserving the characteristic polynomial of the stability matrix by diagonal similarity $\mathcal{M}_{\rm phys} = D_\pi\,\mathcal{M} D_\pi^{-1}$ with $D_\pi = \mathrm{diag}(\pi, 1, 16\pi^2, 16\pi^2, \dots)$. With $v_2 = \widehat{G}/\widehat{a}$ and $v_0 = \widehat{G}/\widehat{b}$, the six-coupling flow $\widehat{\beta}_6(x)$ is defined by the curvature-squared anomalous dimensions

$$\eta_{\widehat{a}} = \eta\left(1 - \frac{\widehat{a}\,T(v_2, \lambda)}{\widehat{a}_s}\right) + \zeta v_2 \widehat{c}\,\Phi_2^2(v_2, \lambda) - c_W \widehat{a}, \tag{14}$$

$$\eta_{\widehat{b}} = \kappa\left(1 - \frac{\widehat{b}\,T(v_0, \lambda)}{\widehat{b}_s}\right) + \zeta^R v_0 \widehat{d}\,\Phi_2^2(v_0, \lambda) + c_0 \widehat{b}, \tag{15}$$

the gravitational Newton anomalous dimension $\eta_N = \widehat{G}b_1/(1-\widehat{G}b_2)$ with

$$b_1 = \frac{1}{3}\left[\frac{1}{2}\big(G_1 - \eta_{\widehat{a}}G_3\big)(v_2,\lambda) + \frac{1}{10}\big(G_1 - \eta_{\widehat{b}}G_3\big)(v_0,\lambda) + \frac{2}{5}G_1(0,\lambda) - 7\right] + \Delta b_1, \tag{16}$$

$$b_2 = -\frac{1}{6}\left[\frac{1}{2}G_2(v_2,\lambda) + \frac{1}{10}G_2(v_0,\lambda) + \frac{2}{5}G_2(0,\lambda)\right], \tag{17}$$

the vacuum trace sum

$$S = 5\big(V_1 - \eta_N V_2 - \eta_{\widehat{a}}V_3\big)(v_2,\lambda) + \big(V_1 - \eta_N V_2 - \eta_{\widehat{b}}V_3\big)(v_0,\lambda) + 4\big(V_1 - \eta_N V_2\big)(0,\lambda) - 4 + \Delta S, \tag{18}$$

and the six beta functions

$$\beta_{\widehat{G}} = (2+\eta_N)\widehat{G}, \qquad \beta_\lambda = -(2-\eta_N)\lambda + \frac{1}{2}\widehat{G}S, \tag{19}$$

$$\beta_{\widehat{a}} = \widehat{a}\,\eta_{\widehat{a}}, \qquad \beta_{\widehat{b}} = \widehat{b}\,\eta_{\widehat{b}}, \tag{20}$$

$$\beta_{\widehat{c}} = 2\widehat{c} + A_3 v_2^3 \Phi_4^4(v_2,\lambda) + B_3\widehat{G}\widehat{c}\,\Phi_2^2(v_2,\lambda), \qquad \beta_{\widehat{d}} = 2\widehat{d} + A_3^R v_0^3 \Phi_4^4(v_0,\lambda) + B_3^R\widehat{G}\widehat{d}\,\Phi_2^2(v_0,\lambda). \tag{21}$$

Notice the explicit bidirectional coupling: $\widehat{c}$ feeds back into $\eta_{\widehat{a}}$ (and hence into η_N, S, $\beta_{\widehat{G}}$, β_λ, and $\beta_{\widehat{a}}$), while $\widehat{d}$ symmetrically feeds back into $\eta_{\widehat{b}}$ (and hence into η_N, S, $\beta_{\widehat{G}}$, β_λ, and $\beta_{\widehat{b}}$). Constructing $\widehat{\beta}_6$ as a directed acyclic graph of elementary rational nodes with paired exact gradient lemmas proves that on the smooth domain (every denominator nonzero) the Fréchet derivative of $\widehat{\beta}_6$ is the explicit 6×6 stability matrix $\mathcal{M}_6(x) = \partial\widehat{\beta}_6/\partial x$. At any zero of $\eta_{\widehat{a}}, \eta_{\widehat{b}}$, the $\widehat{a}$- and $\widehat{b}$-rows satisfy $\partial\beta_{\widehat{a}} = \widehat{a}\nabla\eta_{\widehat{a}}$ and $\partial\beta_{\widehat{b}} = \widehat{b}\nabla\eta_{\widehat{b}}$, with exact cross-derivative decoupling $\partial\eta_{\widehat{b}}/\partial\widehat{d} = \zeta^R v_0 \Phi_2^2$, $\partial\eta_{\widehat{a}}/\partial\widehat{d} = 0$, and $\partial\eta_{\widehat{b}}/\partial\widehat{c} = 0$.

Working at the adopted gravitational benchmark point $P_5 = (\eta, \kappa, \widehat{a}_s, \widehat{b}_s, A_3, B_3, \zeta) = (\frac{1}{5}, \frac{1}{2}, \frac{2}{133}, \frac{1}{50}, 1, 1, 1)$ with $(A_3^R, B_3^R, \zeta^R) = (1,1,1)$, every physical zero $(\widehat{G}, \widehat{a}, \widehat{b} > 0)$ of Eq. (19)–Eq. (21) satisfies $\eta_N = -2$ and $\eta_{\widehat{a}} = \eta_{\widehat{b}} = 0$, which reduces the six-dimensional fixed-point problem bijectively to fixed points of a three-variable map $T_{\mathrm{red},6}(\lambda, w_2, w_0) = (T_{1M}, T_{2M}, T_{36})$ in the Stelle mass ratios $w_2 = 1/v_2 = \widehat{a}/\widehat{G}$, $w_0 = 1/v_0 = \widehat{b}/\widehat{G}$, with

$$\widehat{G}_* = \frac{2}{2b_2 - b_1}, \qquad \widehat{c}_* = -\frac{A_3\tau_2(w_2,\lambda)}{2 + B_3\widehat{G}_* w_2 T(w_2,\lambda)}, \qquad \widehat{d}_* = -\frac{A_3^R\tau_0(w_0,\lambda)}{2 + B_3^R\widehat{G}_* w_0 T(w_0,\lambda)}, \tag{22}$$

where $\tau_2 = T(w_2)/(12\Delta_2^2)$ and $\tau_0 = T(w_0)/(12\Delta_0^2)$ are the three-insertion sources, and the third component T_{36} is dressed by $\delta_0 = \zeta^R\widehat{d}_* T(w_0)/\kappa$:

$$T_{36}(\lambda, w_2, w_0) = \frac{\widehat{b}_s\big(1 + \delta_0 + c_0\widehat{G}_* w_0/\kappa\big)}{\widehat{G}_*\, T(w_0,\lambda)}. \tag{23}$$

At $A_3^R = 0$, the reduced map simplifies identically to the five-coupling matter-coupled system with $\widehat{d}_* = 0$, so both the five-coupling Goroff–Sagnotti family and (at zero matter and $A_3 = 0$) the four-coupling bidirectional contraction are exact conservative sub-families of Eq. (19)–Eq. (21).

3.4 Jordan-block-free 6×6 spectral algebra and five Banach-certified fixed points

Because symbolic expansion of a 6×6 characteristic polynomial exceeds recursion limits and numerical eigenvalue routines can silently miss repeated-root Jordan blocks, our formal spectral library establishes a self-contained algebraic engine over $\mathbb{C}$:

1. *Exact Laplace minor hierarchy:* Every 5×5 determinant equals its recursive first-row Laplace expansion through explicit minors f_2, f_3, f_4, and every 6×6 determinant equals its recursive Laplace expansion e_6, allowing exact interval-arithmetic enclosure of $\det(tI_6 - \mathcal{M}_6)$ at rational test points $t \in \mathbb{Q}$.

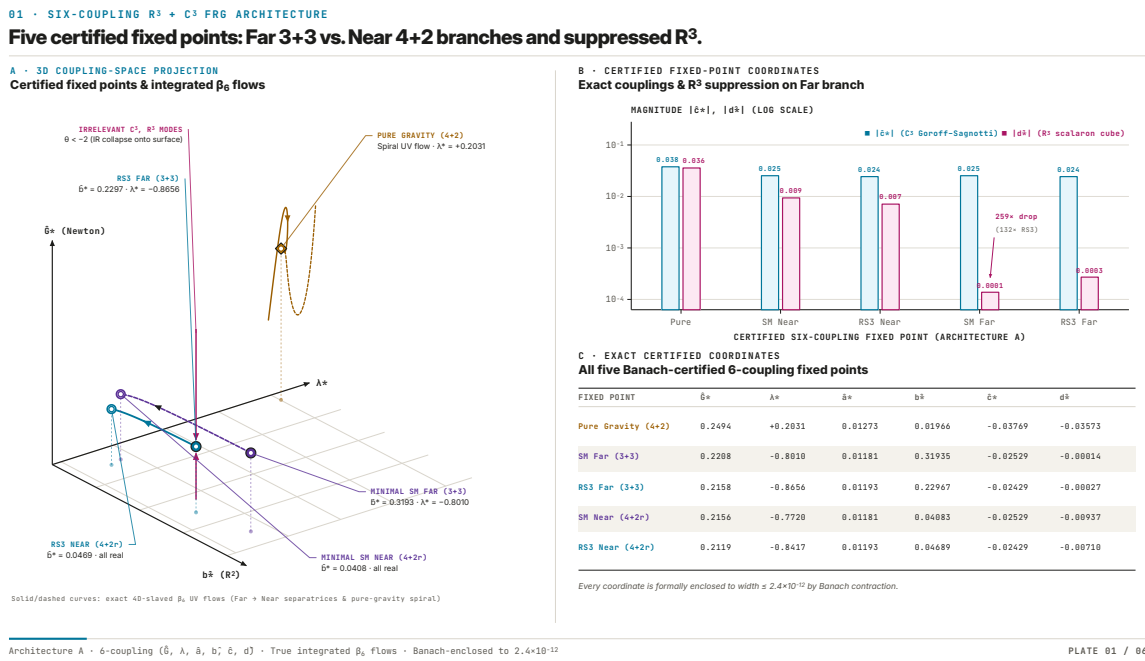

FIXED POINT	b̂*	λ*	â*	b̃*	c̃*	d̃*
Pure Gravity (4+2)	0.2494	+0.2031	0.01273	0.01966	-0.03769	-0.03573
SM Far (3+3)	0.2208	-0.8010	0.01181	0.31935	-0.02529	-0.00014
RS3 Far (3+3)	0.2158	-0.8656	0.01193	0.22967	-0.02429	-0.00027
SM Near (4+2r)	0.2156	-0.7720	0.01181	0.04083	-0.02529	-0.00937
RS3 Near (4+2r)	0.2119	-0.8417	0.01193	0.04689	-0.02429	-0.00710

Fig. 1 Six-coupling R^3+C^3 FRG architecture (Architecture A, Section 3). **a** Orthographic 3D projection in $(\lambda^*, \widehat{b}^*, \widehat{G}^*)$ showing the five Banach-certified fixed points—pure gravity ($4+2$, gold diamond), Minimal SM Far/Near (violet), and SM $+ 3\nu_R$ Far/Near (cyan)—together with exact numerically integrated 4D-slaved $\widehat{\beta}_6$ UV trajectories (Far $\to$ Near heteroclinic separatrices and pure-gravity two-arm UV spiral) and steep IR-collapsing C^3, R^3 directions ($\theta < -2$, magenta arrows). **b** Log-scale comparison of $|\widehat{c}_*|$ and $|\widehat{d}_*|$, showing a 259× suppression of $|\widehat{d}_*|$ on SM Far (132× on SM $+ 3\nu_R$ Far) relative to pure gravity as $\widehat{b}_*$ increases onto the Far branch. **c** Exact certified six-coupling coordinates (enclosed to $\leq 2.4 \times 10^{-12}$).

2. *Monic root splitting:* If a monic polynomial $p \in \mathbb{C}[X]$ vanishes at k pairwise distinct points $r_1, \ldots, r_k$, then $p = \big(\prod_{i=1}^{k}(X - r_i)\big)Q$ with Q monic of degree $\deg p - k$. Hence: (a) six distinct real sign changes of $\det(tI_6 - \mathcal{M}_6)$ yield six distinct real eigenvalues and exhaust the entire complex spectrum (proving all eigenvalues are real with zero Jordan blocks); (b) four distinct real roots leave an explicit real quadratic cofactor $\mu^2 + \beta\mu + \gamma$ with $\gamma = g(0)/\prod(0 - r_i)$ and $\beta = g(1)/\prod(1 - r_i) - 1 - \gamma$ ($g(t) := \det(tI_6 - \mathcal{M}_6)$), whose negative discriminant certifies a complex-conjugate pair $\mu, \bar{\mu}$ with $\operatorname{Im}\mu > 0$.
3. *Nonsingular minor eigenvector-component test:* If the deleted 5×5 minor $\det\big(rI_5 - (\mathcal{M}_6)_{\hat{k},\hat{k}}\big) \neq 0$, then *every* nonzero eigenvector v of $\mathcal{M}_6$ for eigenvalue r satisfies $v_k \neq 0$ (otherwise deleting entry k would give a nonzero null vector of $rI_5 - (\mathcal{M}_6)_{\hat{k},\hat{k}}$, contradiction).

Applying preconditioned Banach contraction to $T_{\mathrm{red},6}$ and this 6×6 spectral algebra yields our three main Architecture A theorems, illustrated in Figs. 1 and 2 and tabulated in Tables 2 and 3.

Theorem 3.2 (Existence, local uniqueness, and Fréchet stability of five six-coupling fixed points)**.** *At the five derived six-coupling parameter points—pure gravity, Minimal SM Type I (Far and Near), and* SM $+ 3\nu_R$ *Type I (Far and Near) with* $(A_3^R, B_3^R, \zeta^R) = (1, 1, 1)$*—each preconditioned Newton map* $N(p) = p - A(p - T_{\mathrm{red},6}(p))$ *is a strict contraction on its closed ball of radius* 10^{-12} *(contraction constants* $K_M \leq 2 \times 10^{-6}$*) and on its uniqueness ball* B_U *of radius* 10^{-4} *in reduced coordinates* (λ, w_2, w_0) *(*$K_U \leq 3 \times 10^{-3}$*). Consequently:*

1. *All five physical fixed points* $x_* \in \mathbb{R}^6$ *satisfy* $\widehat{\beta}_6(x_*) = 0$ *with* $\widehat{G}_*, \widehat{a}_*, \widehat{b}_* > 0$ *and* $\widehat{c}_*, \widehat{d}_* < 0$*, enclosed to width* $\leq 2.4 \times 10^{-12}$ *by the values in Table 2;*
2. *Each* x_* *is the unique zero of* $\widehat{\beta}_6$ *with* $\widehat{G}, \widehat{a}, \widehat{b} > 0$ *whose reduced projection* $(\lambda, \widehat{a}/\widehat{G}, \widehat{b}/\widehat{G})$ *lies in* B_U*;*
3. *At every* x_**, the Fréchet derivative of* $\widehat{\beta}_6$ *exists and equals the explicit stability matrix* $\mathcal{M}_6(x_*)$*.*

To guarantee that critical-exponent counts cannot be corrupted by repeated eigenvalues or defective Jordan blocks, we define three exhaustive complex spectral shapes directly via full characteristic-polynomial factorization over $\mathbb{C}$:

- `Shape42`($\mathcal{M}_6$): $\det(zI_6-\mathcal{M}_6)=(z-r_1)(z-r_2)(z-r_c)(z-r_d)(z-\mu)(z-\bar{\mu})$ for all $z\in\mathbb{C}$, with real $r_1<r_2<0$, $2<r_c<r_d$, $\operatorname{Re}\mu<0<\operatorname{Im}\mu$, all six eigenvalues witnessed by nonzero eigenvectors, and $v_4\neq 0$ (resp. $v_5\neq 0$) on every r_c (resp. r_d) eigenvector (4 UV-relevant + 2 UV-irrelevant).
- `Shape33`($\mathcal{M}_6$): $\det(zI_6-\mathcal{M}_6)=(z-r_1)(z-r_2)(z-r_3)(z-r_b)(z-r_c)(z-r_d)$ with six distinct real roots $r_1<r_2<r_3<0<r_b<1$ and $2<r_c<r_d$, with $v_3\neq 0$ on r_b, $v_4\neq 0$ on r_c, and $v_5\neq 0$ on r_d (3 UV-relevant + 3 UV-irrelevant, all real).
- `Shape42r`($\mathcal{M}_6$): $\det(zI_6-\mathcal{M}_6)=(z-r_1)(z-r_2)(z-r_3)(z-r_4)(z-r_c)(z-r_d)$ with six distinct real roots $r_1<r_2<r_3<r_4<0$ and $2<r_c<r_d$, with $v_4\neq 0$ on r_c and $v_5\neq 0$ on r_d (4 UV-relevant + 2 UV-irrelevant, all real).

Theorem 3.3 (Jordan-block-free spectral classification and mutual exclusion)**.** *For every real* 6×6 *matrix* $\mathcal{M}_6$ *possessing six pairwise distinct complex eigenvalues* $c_1,\dots,c_6$*, its characteristic determinant factors completely as* $\det(zI_6-\mathcal{M}_6)=\prod_{i=1}^{6}(z-c_i)$ *for all* $z\in\mathbb{C}$*, so* $\mathcal{M}_6$ *is diagonalizable over* $\mathbb{C}$ *with zero Jordan blocks and every eigenvalue belongs to* $\{c_1,\dots,c_6\}$*. Moreover, the three spectral shapes are pairwise mutually exclusive, and the five certified six-coupling stability matrices satisfy:*

1. *Pure gravity:* ***`Shape42`*** *(*$4+2$ *with complex spiral pair* $\theta\approx 2.5363\pm 1.8789i$*, real relevant* $+0.4361,+0.1534$*, and irrelevant* $-2.0088,-2.0144$*);*
2. *Minimal SM Type I Far and* $\mathrm{SM}+3\nu_R$ *Type I Far:* ***`Shape33`*** *(all-real* $3+3$*: three relevant directions and three irrelevant directions,* R^2*,* C^3*, and* R^3*);*
3. *Minimal SM Type I Near and* $\mathrm{SM}+3\nu_R$ *Type I Near:* ***`Shape42r`*** *(all-real* $4+2$*: four relevant directions and two irrelevant directions,* C^3 *and* R^3*).*

Proof outline. For each fixed point, exact interval arithmetic on the Laplace expansion $e_6(tI_6-\mathcal{M}_6)$ certifies strict opposite signs at the endpoints of each rational bracket $[a_k,b_k]$, isolating the real roots via the intermediate value theorem. On the four matter branches, all six brackets are strictly separated and disjoint, so monic splitting factors the degree-6 characteristic polynomial completely over $\mathbb{C}$ with unit cofactor $Q=1$, proving all eigenvalues are real and excluding `Shape42`. For pure gravity, the four real roots split off a real monic quadratic with strictly positive $4\gamma-\beta^2$ and $\beta>5$, yielding $\mu,\bar{\mu}$ with $\operatorname{Re}\mu<-5/2$ and $\operatorname{Im}\mu>9/5$, violating realness. Mutual exclusion between `Shape33` and `Shape42r` follows immediately from evaluating the `Shape42r` factorization at the `Shape33` root $r_b\in(0,1)$, which lies strictly between $r_4<0$ and $r_c>2$. Finally, strict sign enclosures of the deleted 5×5 minors establish $v_3\neq 0$, $v_4\neq 0$, and $v_5\neq 0$. □

Theorem 3.4 (Simultaneous UV irrelevance of C^3 and R^3 and Near/Far branch coexistence)**.** *At all five certified six-coupling fixed points, both dimension-six curvature cubes* C^3 *and* R^3 *correspond to strictly UV-irrelevant real eigen-directions with critical exponents* $\theta_{C^3},\theta_{R^3}<-2$ *(nonzero* $\widehat{c}$ *and* $\widehat{d}$ *eigenvector components, respectively). Furthermore:*

1. *At the exact named Type I parameter points for both Minimal SM and* $\mathrm{SM}+3\nu_R$*, the six-coupling flow simultaneously admits a Near physical fixed point (*`Shape42r`*,* $4+2$*) and a Far physical fixed point (*`Shape33`*,* $3+3$*) with strictly ordered scalaron couplings* $\widehat{b}_*^{\mathrm{Near}}<\widehat{b}_*^{\mathrm{Far}}$ *(*$0.0408<0.3193$ *for SM;* $0.0469<0.2297$ *for* $\mathrm{SM}+3\nu_R$*);*
2. *In the conservative five-coupling limit* $A_3^R=0$*, all four matter flows* $(\{\mathrm{SM},\mathrm{RS3}\}\times\{\textit{Type I},\textit{Type II}\})$ *simultaneously possess both a Near* $4+1$ *physical fixed point and a Far* $3+2$ *physical fixed point, all eight pairwise distinct, with* $\theta_{C^3}<-2$ *at all eight matter zeros and at the pure-gravity five-coupling zero.*

Remark 3.5 (Physical origin of the R^3 suppression on the Far branch and resolution of basin dependence). Comparing Table 2 and Table 3 highlights two structural features. First, turning on the R^3 sector ($A_3^R=B_3^R=\zeta^R=1$) shifts the five-coupling coordinates by less than 0.1% on the matter Far branches ($\widehat{b}_*^{\mathrm{RS3}}$ moves from 0.229633 to 0.229672), because the larger Far-branch scalaron coupling $\widehat{b}_*$ lowers $v_0=\widehat{G}_*/\widehat{b}_*$ and suppresses the three-insertion source $v_0^3\Phi_4^4$ by more than two orders of magnitude ($|\widehat{d}_*|$ drops 259× from 0.03573 in pure gravity to 0.000138 on SM Far, and 132× to 0.000271 on $\mathrm{SM}+3\nu_R$ Far). Second, Theorem 3.4 settles a subtle methodological point: the UV critical-surface dimension (3 vs. 4 relevant directions) is *not* uniquely toggled by switching between Type I and Type II matter cutoffs—both cutoff types admit both the Near (4 relevant) and Far (3 relevant) branches. Single-basin Newton searches can land on the Near branch for Type II and the Far branch for Type I,

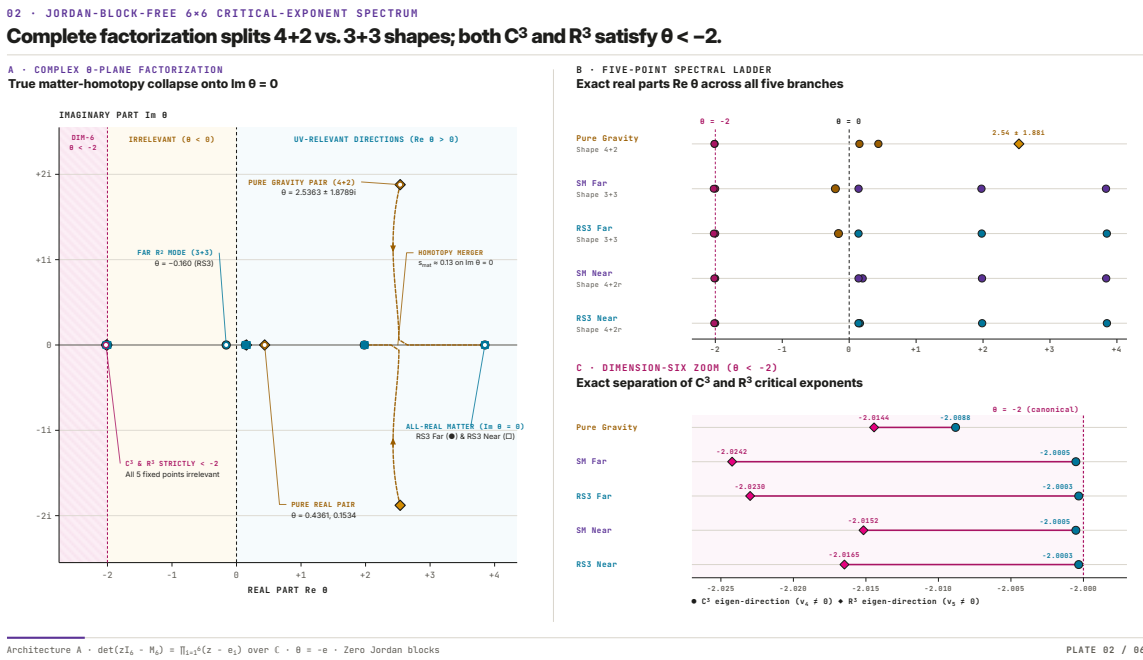

Fig. 2 Jordan-block-free 6×6 critical-exponent spectrum (Theorem 3.3). **a** Complex θ-plane showing all real eigenvalues strictly on $\mathrm{Im}\,\theta = 0$ (filled cyan circles for $\mathrm{SM}+3\nu_R$ Far, open cyan squares for $\mathrm{SM}+3\nu_R$ Near) and the exact computed matter-scaling homotopy ($s_{\mathrm{mat}} \in [0,1]$, dashed amber curves) along which pure gravity's complex-conjugate spiral pair ($\theta = 2.5363 \pm 1.8789i$, gold diamonds) merges onto the real axis at $s_{\mathrm{mat}} \approx 0.13$ before splitting into real matter exponents. **b** Complete real-part spectral ladder across all five certified fixed points. **c** Precision zoom into $\theta \in (-2.027, -1.997)$ resolving the exact separation between θ_{C^3} (cyan circles, $v_4 \neq 0$) and θ_{R^3} (magenta diamonds, $v_5 \neq 0$), both strictly below $\theta = -2$.

Table 2 Exact Banach-certified six-coupling fixed points $(\widehat{G}_*, \lambda_*, \widehat{a}_*, \widehat{b}_*, \widehat{c}_*, \widehat{d}_*)$ and Jordan-block-free critical exponents $\theta_i = -e_i$ in Architecture A. Every coordinate is formally enclosed to width $\leq 2.4 \times 10^{-12}$ and every real eigenvalue to width $\leq 2.1 \times 10^{-6}$.

Content / Branch	$\widehat{G}_*$	λ_*	$\widehat{a}_*$	$\widehat{b}_*$	$\widehat{c}_*$	$\widehat{d}_*$	Critical exponents $\theta_i = -e_i$
Pure Gravity $(4+2)$	0.2494	$+0.2031$	0.01273	0.01966	-0.03769	-0.03573	$2.536 \pm 1.879i$, 0.436, 0.153, -2.009, -2.014
SM Type I Far $(3+3)$	0.2208	-0.8010	0.01181	0.31935	-0.02529	-0.00014	3.837, 1.976, 0.140, -0.206, -2.001, -2.024
RS3 Type I Far $(3+3)$	0.2158	-0.8656	0.01193	0.22967	-0.02429	-0.00027	3.849, 1.980, 0.139, -0.160, -2.000, -2.023
SM Type I Near $(4+2\mathrm{r})$	0.2156	-0.7720	0.01181	0.04083	-0.02529	-0.00937	3.840, 1.984, 0.201, 0.140, -2.001, -2.015
RS3 Type I Near $(4+2\mathrm{r})$	0.2119	-0.8417	0.01193	0.04689	-0.02429	-0.00710	3.851, 1.987, 0.160, 0.139, -2.000, -2.016

creating an apparent scheme-dependent change in predictivity; certifying both pairs at the exact named parameter points eliminates that ambiguity cleanly.

3.5 Bidirectional four-coupling contraction and foundational curved-background FRG benchmarks

The six-coupling hierarchy of Sections 3.3 and 3.4 rests on two formally verified lower-dimensional pillars in our 65-module suite (Section A): the pure-gravity bidirectional four-coupling contraction and a sequence of first-principles curved-background heat-kernel FRG benchmarks.

Setting $A_3 = A_3^R = 0$ and zero matter in Eq. (19)–Eq. (20) recovers the four-coupling bidirectional Stelle–Litim flow in $(\widehat{G}, \lambda, \widehat{a}, \widehat{b})$. Preconditioned Banach contraction encloses the unique physical fixed

Table 3 Conservative five-coupling ($A_3^R = 0$, $\widehat{d}_* = 0$) Banach-certified fixed points across both cutoff types (Type II and Type I) and both matter contents, proving Near $(4+1)$ and Far $(3+2)$ coexistence under every cutoff type.

Content / Cutoff / Branch	$\widehat{G}_*$	λ_*	$\widehat{a}_*$	$\widehat{b}_*$	$\widehat{c}_*$	Critical exponents θ_i
Pure Gravity $(4+1)$	0.2494	+0.2031	0.01273	0.02117	−0.03769	$2.536 \pm 1.880i$, 0.472, 0.153, −2.009
SM Type II Near $(4+1)$	0.4865	−1.7648	0.01122	0.03449	−0.02820	3.868, 2.010, 0.269, 0.143, −2.001
RS3 Type II Near $(4+1)$	0.5615	−2.2592	0.01126	0.03677	−0.02753	3.882, 2.019, 0.245, 0.142, −2.001
SM Type I Near $(4+1)$	0.2157	−0.7724	0.01181	0.04176	−0.02529	3.840, 1.984, 0.206, 0.140, −2.001
RS3 Type I Near $(4+1)$	0.2119	−0.8420	0.01193	0.04778	−0.02429	3.851, 1.987, 0.163, 0.139, −2.000
SM Type II Far $(3+2)$	0.5200	−1.9194	0.01123	0.38455	−0.02817	3.868, 2.004, 0.143, −0.316, −2.001
RS3 Type II Far $(3+2)$	0.6016	−2.4555	0.01127	0.30133	−0.02750	3.883, 2.013, 0.142, −0.281, −2.001
SM Type I Far $(3+2)$	0.2208	−0.8010	0.01181	0.31933	−0.02529	3.837, 1.976, 0.140, −0.206, −2.001
RS3 Type I Far $(3+2)$	0.2158	−0.8656	0.01193	0.22963	−0.02429	3.849, 1.980, 0.139, −0.160, −2.000

point in its ball to width $\leq 2.4 \times 10^{-12}$:

$$\widehat{G}_* \approx 0.249231, \qquad \lambda_* \approx +0.203075, \qquad \widehat{a}_* \approx 0.015689, \qquad \widehat{b}_* \approx 0.021169. \tag{24}$$

To certify ultraviolet attractiveness without numerical diagonalization, we prove the general complex quartic Routh–Hurwitz criterion[70;71]: every root $\mu \in \mathbb{C}$ of $\mu^4 + c_1\mu^3 + c_2\mu^2 + c_3\mu + c_4 = 0$ with $c_1, c_3, c_4 > 0$ and $c_1c_2c_3 - c_3^2 - c_1^2c_4 > 0$ obeys $\operatorname{Re}\mu < 0$. Interval verification of these four inequalities on the 4×4 Fréchet Jacobian proves $\operatorname{Re}\mu < 0$ for every complex eigenvalue, and exact diagonal similarity transfers the identical characteristic polynomial and all four positive UV critical exponents ($\operatorname{Re}\theta > 0$) to physical coordinates $(G, \Lambda, f_2^2, f_0^2)$. Comparing Eq. (24) against Tables 2 and 3 quantifies the exact back-reaction of the dimension-six operators: turning on C^3 shifts $\widehat{a}_*$ from 0.01569 to 0.01273 while leaving $(\widehat{G}_*, \lambda_*)$ fixed within 0.07%, and subsequently turning on R^3 shifts $\widehat{b}_*$ from 0.02117 to 0.01966 without altering the four-relevant UV stability count.

In parallel, our curved-background covariant heat-kernel modules establish exact one- to four-coupling benchmarks on S^4, Einstein, and Ricci-flat 4D manifolds:

Proposition 3.6 (Curved-background heat-kernel and Wetterich FRG benchmarks)**.** *The following exact curved-background identities and lower-dimensional fixed points are formally certified (module index in Section A):*

1. Einstein–Hilbert Reuter fixed point and IR Gaussian saddle: *Both Type I and Type II harmonic-gauge Einstein–Hilbert Wetterich flows possess the classical IR Gaussian saddle* $(g, \lambda) = (0, 0)$ *with exact Jacobian eigenvalues* $(+2, -2)$ *together with a certified non-Gaussian UV fixed point with* $g_* > 0$, $\lambda_* < 1/2$, *and complex-conjugate UV-attractive spiral exponents.*
2. Universal 4D supertrace b_4, algebraic Weyl-cubed identities, and $f(R)$ fixed points: *For every algebraic* 4D *Riemann tensor, the gravitational supertrace obeys* $b_4 = \frac{1}{120}R^2 + \frac{7}{20}R_{\mu\nu}^2 + \frac{53}{90}E_4$ *(reducing to* $\frac{419}{2160}R^2$ *on* S^4*), and every algebraic* 4D *Weyl tensor satisfies the exact cubic syzygies* $2I_2 + I_1 = 0$ *and* $2I_3 - I_1 = 0$ *(non-vacuously witnessed on a Petrov Type D Weyl tensor with* $I_1 = -96$*). In the* $f(R)$ *truncation up to* R^3*, the* R^3 *coupling is UV-irrelevant (*$\theta_4 < -3.8$*) alongside three UV-relevant directions (*$\theta_3 > 2$ *and complex pair* $\alpha > 2.65$, $\beta > 2$*).*
3. Einstein-background Weyl-squared Hessian and four-coupling fixed point: *For every algebraic* 4D *Weyl tensor, the* 9×9 *symmetric-traceless Weyl endomorphism* W *satisfies* $\operatorname{tr} W = 0$, $\operatorname{tr} W^2 = 3C^2$, *and* $\operatorname{tr} W^3 = -3I_1$*. On an Einstein background, the* C^2 *transverse-traceless Hessian factors exactly as* $(\Delta_L - R/2)(\Delta_L - R/3)$*, reproducing the exact one-loop coefficients* 53/45 *and* 413/180 *and yielding a Banach-certified four-coupling fixed point with* $g_* \in (0.48, 0.49)$*, strictly positive Euclidean propagators (*$P_T > 0.87$, $P_H > 3.64$*), and* 3 *relevant* +1 *irrelevant critical exponents.*

4. First-principles derived a_2/b_6 Goroff–Sagnotti traces on Ricci-flat backgrounds: *Explicit covariant second variation on arbitrary* 4D *Ricci-flat manifolds (witnessed by the exact Schwarzschild Bianchi wave identity* $|\nabla C|^2 - \frac{1}{2}\Box C^2 = 3I_1$*) yields the universal Seeley–DeWitt coefficient* $b_6 = \frac{1}{1512} I_1$ *and off-diagonal heat-kernel traces* $c_{s^{-4}} = 0$, $c_{s^{-3}}(c) = \frac{49}{4} + \frac{21}{4}c$, *and* $c_{s^{-2}}(c) = -\frac{45}{8} - 20c + \frac{21}{8}c^2$ *as exact polynomials in the endomorphism parameter* c. *Evaluating the derived three-coupling* (g, λ, σ) *Wetterich flow certifies strong Goroff–Sagnotti irrelevance in both Type II* ($c = 1$: $c_{s^{-2}} = -23$, $\theta^{\mathrm{II}}_{\mathrm{GS}} \in (-10.17, -10.15)$) *and Type I* ($c = 0$: $c_{s^{-2}} = -45/8$, $\theta^{\mathrm{I}}_{\mathrm{GS}} \in (-6.49, -6.48)$), *together with global uniqueness of the bounded safe trajectory along the nonlinear* $\lambda = 0$ *Reuter trajectory* ($\theta^{\mathrm{1D}}_{\mathrm{GS}} = -486/59 \approx -8.237$).

Taken together, Theorem 3.6 and Theorems 3.2 to 3.4 demonstrate coherent qualitative stability across independent curvature bases and truncation depths: whether one computes the off-diagonal b_6 trace directly on Ricci-flat backgrounds or couples C^3 and R^3 bidirectionally into the full fourth-order Stelle–Litim flow with Standard Model or SM + $3\nu_R$ matter, the Goroff–Sagnotti counterterm and the R^3 curvature cube remain strictly UV-irrelevant ($\theta < -2$) with zero Jordan-block degeneracy.

4 Matter phase boundaries, the $2 \leq N_{\mathrm{gen}} \leq 7$ generation window, Lee–Wick poles, and the double-fold S-curve

While Architecture A establishes six-coupling $R^3 + C^3$ stability at fixed benchmark parameters, answering *which* matter spectra permit a physically healthy, ghost-free ultraviolet fixed point requires a first-principles Wetterich truncation[19] with zero free gravitational tuning parameters and continuous control over the regulator scheme. In this section we develop Architecture B (complete formal-module correspondence in Section A): we derive the coupled five-coupling flow $(u_0, u_1, u_2, u_C, \sigma)$ directly from Litim threshold integrals, certify exact one-loop, Gauss–Bonnet, and Cardy conformal-anomaly benchmarks, map the Donà–Eichhorn–Percacci scalar-pole boundaries, establish the exact $2 \leq N_{\mathrm{gen}} \leq 7$ generation window (together with full $M_5^{-1} J V_5$ critical-exponent diagnostics), classify the Lorentzian complex-p^2 Lee–Wick poles, and prove the global double-fold S-curve catastrophe with triple fixed-point coexistence at $N_{\mathrm{gen}} = 7$.

4.1 First-principles Litim-integral five-coupling flow, Routh–Hurwitz stability, and Cardy ratios

In the five-coupling curvature-invariant basis

$$\Gamma_k[g] = \int d^4x \sqrt{g} \left(k^4 u_0 + k^2 u_1 R + u_2 R^2 + u_C C^2 + k^{-2} \sigma C^3 \right), \tag{25}$$

the physical Newton coupling and dimensionless cosmological constant are recovered by the smooth diffeomorphism $g = -\pi/u_1$, $\lambda = -u_0/(2u_1)$ (physical gravity requires $u_1 < 0 \iff g > 0$). For a fourth-order kinetic operator $A_2 z^2 + A_1 z + A_0$ regulated by the Type I pure-Laplacian $(-\nabla^2)$ Litim cutoff[23], the scale-derivative kernel is the quadratic polynomial $\partial_t R_k(z) = (4A_2 + \dot{A}_2) + (4A_1 + \dot{A}_1) - (2A_1 + \dot{A}_1) z - \dot{A}_2 z^2$ on $z \in [0, 1]$ with constant regularized denominator $D = A_2 + A_1 + A_0$. Direct integration via the fundamental theorem of calculus proves all six threshold functionals exactly:

$$Q_2[W] = \frac{2A_2 + \frac{4}{3}A_1 + \frac{1}{4}\dot{A}_2 + \frac{1}{6}\dot{A}_1}{D}, \qquad Q_1[W] = \frac{4A_2 + 3A_1 + \frac{2}{3}\dot{A}_2 + \frac{1}{2}\dot{A}_1}{D}, \tag{26}$$

$$Q_0[W] = \frac{4A_2 + 4A_1 + \dot{A}_2 + \dot{A}_1}{D}, \qquad Q_{-1}[W] = \frac{2A_1 + \dot{A}_1}{D}, \tag{27}$$

together with $Q_2[W_2] = Q_2[W]/D$ and $Q_3[W_2] = \left(\frac{2}{3}A_2 + \frac{5}{12}A_1 + \frac{1}{15}\dot{A}_2 + \frac{1}{24}\dot{A}_1\right)/D^2$. Notice that at any non-Gaussian fixed point ($\dot{A}_1 = 0$ in dimensionless units corresponds to $\eta_N = -2$ in dimensional units), $Q_{-1}[W] = 2A_1/D \neq 0$, cleanly complementing the one-loop $\eta_N = 0$ vanishing of Theorem 3.1. Applying Eq. (26)–Eq. (27) to the York transverse-traceless spin-2 denominator $d_{T0}(u) = -\frac{1}{2}u_0 - \frac{1}{2}u_1 + u_C$ and conformal spin-0 denominator $d_{H0}(u) = \frac{1}{8}u_0 + \frac{3}{16}u_1 + \frac{9}{8}u_2$, combined with the one-parameter

endomorphism-dressed ghost and matter cutoff family $R_k^{(s)}(\Delta) = (k^2 - \Delta_s)\theta(k^2 - \Delta_s)$, $\Delta_s = -\nabla^2 - (1-s)cR$ for $s \in [0,1]$, yields the exact stationarity system $V_5^{(s)}(u; N_S, N_D, N_V) = 0$ and flow mass matrix $M_5(u)$ obeying $M_5(u)\,\partial_t u + V_5^{(s)}(u) = 0$, with exact Fréchet Jacobian $JV_5(u) = \partial V_5^{(s)}/\partial u$ independent of (s, N_S, N_D, N_V).

Four exact benchmark identities validate this first-principles truncation before any fixed point is sought:

1. *Exact one-loop gravitational limits (Christensen–Duff and Ricci-flat $C^2 + E_4$ Stelle limit):* Evaluating the Type I Weyl endomorphism $E = -2C$ integral analytically recovers the exact Christensen–Duff one-loop coefficient $53/45$[10] in the pure Einstein–Hilbert limit ($u_2 = u_C = 0$) and the exact asymptotically free fourth-order coefficient

$$\frac{413}{180} = \frac{133}{20} - \frac{196}{45} > 0 \tag{28}$$

   in the pure quadratic limit ($u_1 = 0$). Explicitly, Eq. (28) is the *Ricci-flat $C^2 + E_4$ projection*: on four-dimensional Ricci-flat backgrounds ($R_{\mu\nu} = 0$), the topological Euler density satisfies $E_4 = C^2$, so evaluating the Wetterich trace on Ricci-flat spaces combines the pure Weyl-squared one-loop coefficient $133/20$ (matching $a_\ell = 133/(160\pi^2)$ in Section 6.1[8;9]) with the one-loop topological Gauss–Bonnet beta-function coefficient $-196/45$.
2. *Universal* 4D *Gauss–Bonnet propagator decoupling and degree-*5 *Routh–Hurwitz stability:* Formal four-dimensional tensor variation proves that $E_4 = R^2_{\mu\nu\rho\sigma} - 4R^2_{\mu\nu} + R^2$ obeys $L_{\mu\nu} = 0$ identically, so the topological coupling decouples from all bulk graviton propagators (even though its one-loop beta function contributes $-196/45$ to the Ricci-flat projection Eq. (28)). For the 5×5 stability matrix $S = M_5^{-1} JV_5$, zero-cancellation Vieta deflation factors off the two negative real roots (irrelevant directions) and proves over $\mathbb{C}$ that the remaining cubic $z^3 - s_1 z^2 + s_2 z - s_3$ with $s_1, s_2, s_3 > 0$ and $s_1 s_2 - s_3 > 0$[70;71] splits into three open right-half-plane roots ($\mathrm{Re}\, z > 0$), certifying exact 3-relevant / 2-irrelevant complex UV stability.
3. *Exact ghost-homotopy invariance:* Across the entire scheme continuum $s \in [0,1]$, the Landau–DeWitt vector ghost ($d = 4, c = 1/4$) plus York Jacobian scalars ($c = 1/2$ minus $c = 1/3$) satisfy $\mathrm{gh}_0(s) = -2$, $\mathrm{gh}_2(s) = -463/1080$ (via the exact algebraic identity $s^2 + 2s(1-s) + (1-s)^2 = 1$), and $\mathrm{gh}_3(s) = 11/180$ identically, while only the Newton trace $\mathrm{gh}_1(s) = -\frac{11}{6} + \frac{7}{12}s$ interpolates linearly from Type II ($s = 0$) to Pure Type I ($s = 1$).
4. *Exact Cardy conformal-anomaly ratios and vanishing direct C^3 matter trace:* Evaluating the second-order Litim moments ($Q_2 = 1, Q_1 = 2, Q_0 = 2, Q_{-1} = 0$) on the scalar, Dirac, and gauge-vector heat kernels yields the exact Cardy Euler-anomaly ratios[49;50]

$$\frac{a_D}{a_S} = 11, \qquad \frac{a_V}{a_S} = 62, \tag{29}$$

   alongside $m_{\mathrm{matter},4}(s) \equiv 0$ (zero direct matter sourcing of C^3) and scheme-invariant R^2 and C^2 matter traces, while $m_{\mathrm{matter},1}(s) = \frac{1}{6} - \frac{21}{4}s$ (SM) and $\frac{2}{3} - 6s$ (SM + $3\nu_R$) matches the exact Newton-shift gap Eq. (11).

For pure gravity ($N_S = N_D = N_V = 0$), affine-interval continuation certifies a unique continuous fixed-point curve $u^*_{\mathrm{pure}}(s)$ across all $s \in [0,1]$ with $g_*(0) \approx 1.0552$, $u_C^*(0) \approx -1.0133$ (Type II) and $g_*(1) \approx 1.1783$, $u_C^*(1) \approx -0.9069$ (Pure Type I), with uniform 3-relevant / 2-irrelevant complex UV stability across the entire homotopy. Crucially, however, pure gravity exhibits two severe pathologies in this truncation (Table 5): (i) $u_C^* < 0$ across all $s \in [0,1]$, which induces a finite Euclidean spin-2 ghost pole ($z_+ \approx +1.500$ at $s = 1$); and (ii) a near-singular flow mass matrix ($\det M_5 \approx +0.0415$ at $s = 0$, $+0.1278$ at $s = 1$), producing an anomalously large irrelevant critical exponent $\theta_5 \approx -723.6$ ($s = 0$) / -301.1 ($s = 1$). Coupling to Standard Model or SM + $3\nu_R$ matter simultaneously cures *both* pathologies, driving $u_C^* > 0$ and restoring $\det M_5 \approx 0.80$–0.85 with clean $O(1)$ critical exponents!

4.2 Euclidean spin-2 propagator dichotomy and Donà–Eichhorn–Percacci scalar poles

On flat four-dimensional space with dimensionless momentum squared $z = p^2/k^2$, the transverse-traceless spin-2 inverse propagator of Eq. (25) is the quadratic polynomial

$$P_{\mathrm{TT}}(u, z) = u_C z^2 - \frac{1}{2} u_1 z - \frac{1}{2} u_0, \tag{30}$$

matching the regulated denominator $P_{\mathrm{TT}}(u, 1) = d_{T0}(u)$ at $z = 1$. Its Euclidean positivity is governed by an exact algebraic dichotomy, while increasing the real scalar count N_S drives $u_1^* \to 0^-$ (an exact $1/g_* = 0$ Donà–Eichhorn–Percacci scalar pole[41]), mapped across the full (N_D, N_S) plane in Fig. 3a.

Theorem 4.1 (Spin-2 Euclidean dichotomy and exact Donà–Eichhorn–Percacci scalar poles)**.** *The spin-2 inverse propagator Eq. (30) and the matter-coupled fixed-point curves $V_5^{(s)}(u; N_S, N_D, N_V) = 0$ satisfy:*

1. Global Euclidean positivity vs. ghost-pole dichotomy: *Whenever $u_0 < 0$, $u_1 < 0$, and $u_C > 0$, one has $P_{\mathrm{TT}}(u, z) \geq -\frac{1}{2} u_0 > 0$ for every $z \geq 0$ (global Euclidean spin-2 ghost freedom). Conversely, whenever $u_0 < 0$ and $u_C < 0$, there exists a finite Euclidean ghost pole $z_{\mathrm{ghost}} > 0$ with $P_{\mathrm{TT}}(u, z_{\mathrm{ghost}}) = 0$.*
2. Pure Type I ($s = 1$) scalar poles (MSSM exclusion): *Certified affine-interval continuation proves exact $1/g_* = 0$ ($u_1^* = 0$) poles at*

$$N_S^{\mathrm{pole}}(\mathrm{SM}, s = 1) \in (40, 41) \quad (\approx 40.080), \qquad N_S^{\mathrm{pole}}(\mathrm{RS3}, s = 1) \in (41, 42) \quad (\approx 41.450), \tag{31}$$

   crossing from physical $g_* > 0$ ($u_1^* < 0$) to unphysical $g_* < 0$ ($u_1^* > 0$). Thus the Minimal Higgs doublet ($N_S = 4$) sits deep inside the physical phase, whereas the Minimal Supersymmetric Standard Model ($N_S = 49 > 42$) lies strictly on the unphysical $g_* < 0$ side.
3. Type II ($s = 0$) scalar poles (2HDM exclusion): *At Type II ($s = 0$), exact $1/g_* = 0$ poles occur at*

$$N_S^{\mathrm{pole}}(\mathrm{RS3}, s = 0) \in (7, 8) \quad (\approx 7.558), \qquad N_S^{\mathrm{pole}}(\mathrm{SM}, s = 0) \in (10, 11) \quad (\approx 10.873). \tag{32}$$

   Consequently, for $\mathrm{SM} + 3\nu_R$, even a two-Higgs-doublet extension ($N_S = 8$) already crosses onto the unphysical $g_* < 0$ side at Type II.

Proof outline. For Part 1, if $u_0 < 0, u_1 < 0, u_C > 0$, then for every $z \geq 0$ both $u_C z^2 \geq 0$ and $-\frac{1}{2} u_1 z \geq 0$, so $P_{\mathrm{TT}}(u, z) \geq -\frac{1}{2} u_0 > 0$. Conversely, if $u_0 < 0$ and $u_C < 0$, then $P_{\mathrm{TT}}(u, 0) = -\frac{1}{2} u_0 > 0$ while at $Z = (|u_1| + |u_0| + 1)/(-u_C) + 1 > 1$ one has $P_{\mathrm{TT}}(u, Z) < 0$, so the intermediate value theorem produces $z_{\mathrm{ghost}} \in (0, Z)$ with $P_{\mathrm{TT}}(u, z_{\mathrm{ghost}}) = 0$. For Parts 2 and 3, affine-interval Banach contraction certifies continuous implicit curves $u^*(N_S)$ across $[40, 41]$, $[41, 42]$, $[7, 8]$, and $[10, 11]$ with opposite endpoint signs for $u_1^*(N_S)$, forcing exact zeros $u_1^*(N_S^{\mathrm{pole}}) = 0$ by the intermediate value theorem. □

4.3 Fermion-induced ghost freedom, the $2 \leq N_{\mathrm{gen}} \leq 7$ generation window, and full stability diagnostics

Fixing $N_S = 4$, $N_V = 12$, and Pure Type I ($s = 1$) and scanning the Dirac fermion count N_D uncovers a sharp fermion-induced phase transition that flips u_C^* from negative (pure gravity and one generation) to positive, creating a finite window of viable fermion generations (Fig. 3b, Table 4). Away from the $N_S = 4$ slice, the full two-dimensional boundaries $N_D^{\mathrm{ghost}}(N_S)$, $N_D^{\mathrm{LW}}(N_S)$, and $N_D^{F_1}(N_S)$ curve smoothly across the (N_D, N_S) plane (Fig. 3a): $N_D^{\mathrm{ghost}}(N_S)$ rises from 8.115 at $N_S = 0$ through 9.093 at $N_S = 4$ to 15.073 at $N_S = 30$, meeting both $N_D^{\mathrm{LW}}(N_S)$ and the Pure Type I DEP scalar-pole boundary at the exact triple junction $(N_D, N_S) \approx (16.60, 34.68)$, while the upper fold $N_D^{F_1}(N_S)$ curves inward from 57.95 at $N_S = 0$ to meet the DEP curve near $(44.27, 60.8)$, enclosing a completely bounded viable Lee–Wick region.

Theorem 4.2 (Spin-2 ghost-freedom transition and exact generation window $2 \leq N_{\mathrm{gen}} \leq 7$)**.** *At Pure Type I ($s = 1$) with $N_S = 4$ and $N_V = 12$:*

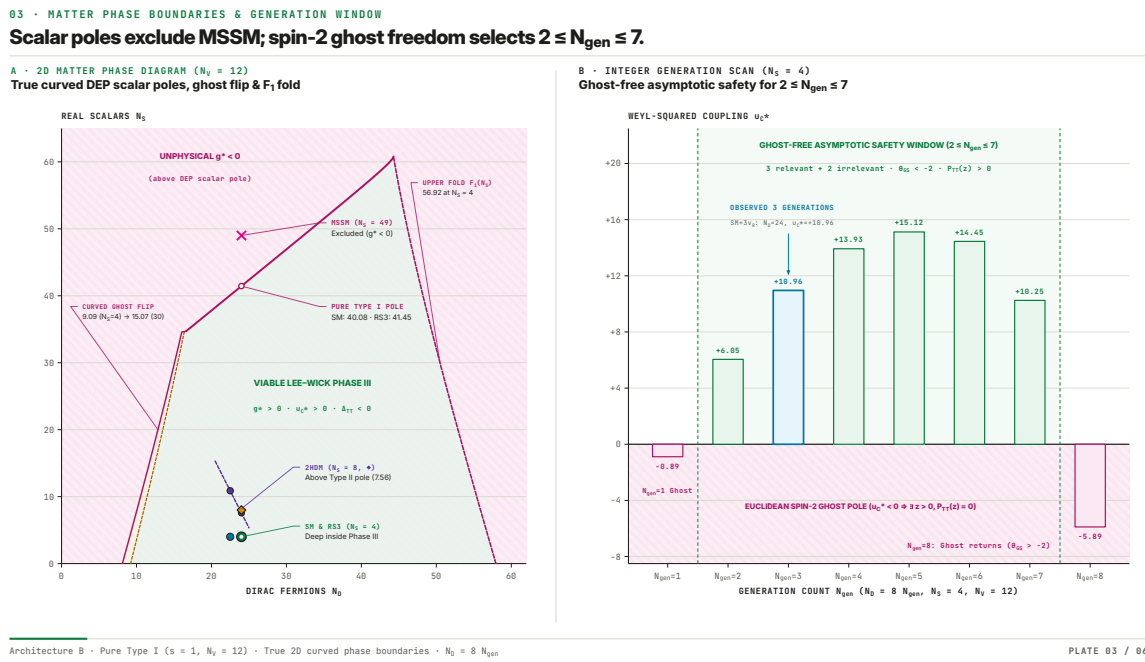

Fig. 3 Matter phase boundaries and integer generation window in Architecture B (Theorems 4.1 and 4.2). **a** Exact 2D (N_D, N_S) matter phase diagram at Pure Type I ($s = 1, N_V = 12$): true computed curved boundaries $N_D^{\text{ghost}}(N_S)$ (solid magenta, rising from 8.12 at $N_S = 0$ to 15.07 at $N_S = 30$), $N_D^{\text{LW}}(N_S)$ (dashed amber), the DEP scalar-pole curve ($N_S^{\text{pole}} = 40.08$ SM, 41.45 SM$+3\nu_R$, meeting the ghost-flip curve at the triple junction $(16.60, 34.68)$), and the upper fold $N_D^{F_1}(N_S)$ enclose the closed green viable Lee–Wick Phase III region while excluding the MSSM ($N_S = 49$, cross); the dashed violet curve plots the true Type II DEP boundary passing directly through both Type II pole markers (10.87 SM, 7.56 SM $+ 3\nu_R$, below 2HDM $N_S = 8$, gold diamond). **b** Exact integer generation scan $N_{\text{gen}} = 1, \ldots, 8$ ($N_D = 8N_{\text{gen}}$, $N_S = 4$) displaying u_C^*: Euclidean spin-2 ghost poles appear at $N_{\text{gen}} = 1$ (-0.89) and $N_{\text{gen}} = 8$ (-5.89), isolating the exact ghost-free asymptotic-safety window $2 \le N_{\text{gen}} \le 7$ containing the observed three generations ($N_{\text{gen}} = 3$, $u_C^* = +10.96$).

1. Fermion-induced ghost-freedom transition: *Certified affine-interval continuation over* $N_D \in [9, 37/4]$ *proves the existence of an exact phase transition* $N_D^{\text{ghost}} \in (9, 37/4)$ *(*≈ 9.0926*) where* $u_C^*(N_D^{\text{ghost}}) = 0$*, separating the Euclidean ghost-pole phase (*$u_C^* < 0$ *for* $N_D < N_D^{\text{ghost}}$*) from the globally Euclidean ghost-free phase (*$u_C^* > 0$ *for* $N_D > N_D^{\text{ghost}}$*).*
2. Exact generation window $2 \le N_{\text{gen}} \le 7$: *Across all eight integer generation counts* $N_{\text{gen}} \in \{1, \ldots, 8\}$ *with* $N_D = 8N_{\text{gen}}$ *(Tables 4 and 5):*
   - $N_{\text{gen}} = 1$ *(*$N_D = 8$*): exhibits a finite Euclidean spin-2 ghost pole (*$u_C^* \approx -0.89 < 0 \implies \exists z > 0,\ P_{\text{TT}}(z) = 0$*);*
   - $N_{\text{gen}} \in \{2, 3, 4, 5, 6, 7\}$ *(*$N_D \in \{16, 24, 32, 40, 48, 56\}$*): every generation admits a certified fixed point with* $g_* > 0$*, global Euclidean spin-2 positivity (*$\forall z \ge 0,\ P_{\text{TT}}(z) > 0$*), five strictly real critical exponents (*3 *relevant,* 2 *irrelevant, codimension-*2 *UV predictivity certified by left-eigenvector transversality), and enhanced Goroff–Sagnotti irrelevance (*$\theta_{\text{GS}} < -2$*);*
   - $N_{\text{gen}} = 8$ *(*$N_D = 64$*): the Euclidean spin-2 ghost pole returns (*$u_C^* \approx -5.889 < -5 < 0 \implies \exists z > 0,\ P_{\text{TT}}(z) = 0$*) and Goroff–Sagnotti irrelevance weakens (*$\theta_{\text{GS}} \approx -1.855 > -2$*).*

Remark 4.3 (Near-singular M_5 in pure gravity and stabilization by matter). Table 5 exposes an important diagnostic feature of fourth-order Litim truncations that is invisible from sign counts alone. In pure gravity ($u_C^* < 0$) and at $N_{\text{gen}} = 1$ ($u_C^* \approx -0.89$), the flow mass matrix $M_5(u_*)$ approaches near-degeneracy ($\det M_5 = +0.0415$ at $s = 0$, $+0.1278$ at $s = 1$, $+0.1857$ at $N_{\text{gen}} = 1$), producing large anomalous exponents ($\theta_5 = -723.6$ at $s = 0$, -301.1 at $s = 1$; $\theta_1 = +42.4$ at $N_{\text{gen}} = 1$) reminiscent of the well-known η-pole sensitivity of Litim higher-derivative flows[27;32]. Once realistic matter ($N_{\text{gen}} \ge 2$) drives u_C^* positive and large, $\det M_5$ immediately stabilizes to 0.74–0.96 and every critical exponent moderates to clean $O(1)$ near-canonical values (for SM $+ 3\nu_R$ at $s = 1$: $+5.61, +3.31, +1.39, -0.072, -2.25$). Notice also how $\theta_4 = -0.012$ at $N_{\text{gen}} = 7$ approaches zero right before annihilating at the saddle-node fold F_1 ($N_D^{F_1} = 56.92$).

Table 4 Certified phase classification across integer generation counts $N_{\rm gen} = 1, \ldots, 8$ ($N_D = 8N_{\rm gen}, N_S = 4, N_V = 12, s = 1$), together with the three coexisting fixed points at $N_{\rm gen} = 7$.

$N_{\rm gen}$	N_D	Branch / Phase	u_C^*	$\Delta_{\rm TT}$	UV	Status
1	8	Phase I (Euclidean ghost)	-0.89	> 0	$3+2$	Ghost pole $z_+ > 0$
2	16	Phase III (Lee–Wick/fakeon)	$+6.05$	< 0	$3+2$	Viable ($\theta_{\rm GS} < -2$)
3	**24**	**Phase III (SM + $3\nu_R$)**	$\mathbf{+10.96}$	$\mathbf{-163.1}$	**3+2**	**Observed ($s \in [0,1]$)**
4	32	Phase III (Lee–Wick/fakeon)	$+13.93$	< 0	$3+2$	Viable ($\theta_{\rm GS} < -2$)
5	40	Phase III (Lee–Wick/fakeon)	$+15.12$	< 0	$3+2$	Viable ($\theta_{\rm GS} < -2$)
6	48	Phase III (Lee–Wick/fakeon)	$+14.45$	< 0	$3+2$	Viable ($\theta_{\rm GS} < -2$)
7	56	Upper: Phase III (Lee–Wick)	$+10.25$	< -480	$3+2$	Viable (sharp cap)
7	56	Middle: Phase III (fold)	$+5.29$	< -240	$4+1$	Unstable partner
7	56	Lower: Phase I (ghost)	-4.73	> 0	$3+2$	Ghost pole $z_+ > 0$
8	64	Phase I (Euclidean ghost)	-5.89	> 0	$3+2$	Ghost ($\theta_{\rm GS} > -2$)

Table 5 Full 5×5 stability spectra $\theta_i = \mathrm{eig}(M_5(u_*)^{-1} J V_5(u_*))$ and flow mass-matrix determinants $\det M_5(u_*)$ across Architecture B benchmarks and $N_{\rm gen} = 1, \ldots, 8$ ($N_S = 4, N_V = 12$). Pure gravity and $N_{\rm gen} = 1$ exhibit large eigenvalues driven by small $\det M_5$; realistic matter ($N_{\rm gen} \geq 2$) restores $\det M_5 \sim O(1)$ and clean $O(1)$ exponents.

Benchmark / Content	u_C^*	$\det M_5$	Critical exponents $\theta_i = \mathrm{eig}(M_5^{-1} J V_5)$
Pure Gravity ($s = 0$, Type II)	-1.0133	$+0.0415$	$+20.040, +2.919 \pm 0.357i, -1.560, -723.578$
Pure Gravity ($s = 1$, Pure Type I)	-0.9069	$+0.1278$	$+18.577, +2.905 \pm 0.566i, -1.534, -301.071$
Minimal SM ($s = 0$, Type II)	$+10.6587$	$+0.7960$	$+8.461, +3.442, +1.418, -0.086, -2.298$
Minimal SM ($s = 1$, Pure Type I)	$+10.1937$	$+0.8374$	$+5.950, +3.342, +1.405, -0.078, -2.276$
SM + $3\nu_R$ ($s = 0$, Type II)	$+11.5324$	$+0.8094$	$+8.057, +3.438, +1.408, -0.080, -2.275$
SM + $3\nu_R$ ($s = 1$, Pure Type I)	$+10.9584$	$+0.8503$	$+5.610, +3.305, +1.387, -0.072, -2.254$
$N_{\rm gen} = 1$ ($N_D = 8$, $s = 1$)	-0.8893	$+0.1857$	$+42.368, +2.975, +2.124, -3.263, -5.193$
$N_{\rm gen} = 2$ ($N_D = 16$, $s = 1$)	$+6.0467$	$+0.7381$	$+9.010, +3.406, +1.477, -0.128, -2.466$
$N_{\rm gen} = 4$ ($N_D = 32$, $s = 1$)	$+13.9252$	$+0.8946$	$+4.661, +3.036, +1.283, -0.053, -2.183$
$N_{\rm gen} = 5$ ($N_D = 40$, $s = 1$)	$+15.1232$	$+0.9189$	$+4.340, +2.761, +1.167, -0.041, -2.148$
$N_{\rm gen} = 6$ ($N_D = 48$, $s = 1$)	$+14.4497$	$+0.9354$	$+4.202, +2.543, +1.035, -0.031, -2.127$
$N_{\rm gen} = 7$ Upper ($N_D = 56$, $s = 1$)	$+10.2475$	$+0.9509$	$+4.116, +2.345, +0.841, -0.012, -2.109$
$N_{\rm gen} = 8$ ($N_D = 64$, $s = 1$)	-5.8893	$+0.9563$	$+4.396, +2.856, +1.148, -0.382, -1.855$

4.4 Lorentzian complex-p^2 Lee–Wick poles and the global double-fold S-curve catastrophe

Euclidean positivity ($u_C > 0$) does not by itself eliminate real Lorentzian Ostrogradsky ghosts at $z < 0$. Analytic continuation of Eq. (30) to complex momentum squared $z \in \mathbb{C}$, governed by the exact discriminant

$$\Delta_{\rm TT}(u) := \frac{1}{4} u_1^2 + 2 u_C u_0, \tag{33}$$

together with the flat spin-0 Starobinsky scalaron inverse propagator $P_0(u, z) = \frac{9}{8} u_2 z^2 + \frac{3}{16} u_1 z + \frac{1}{8} u_0$ (matching $P_0(u, 1) = d_{H0}(u)$), produces a complete four-way complex-pole classification (Fig. 4a).

Theorem 4.4 (Complex-p^2 pole trichotomy, Stelle-to-Lee–Wick exceptional point, and uniform SM/SM + $3\nu_R$ Phase III)**.** *For every $u \in \mathbb{R}^5$ with $u_0 < 0$ and $u_1 < 0$:*

1. Phase I ($u_C < 0$): $\Delta_{\rm TT} > 0$ *with one Euclidean ghost pole $z_+ > 0$ and one Lorentzian pole $z_- < 0$. Pure gravity lies in Phase I at both $s = 0$ and $s = 1$ (with $z_+ \approx +1.500$ at $s = 1$).*
2. Phase II ($u_C > 0, \Delta_{\rm TT} > 0$): $P_{\rm TT}(z) > 0$ *on all $z \geq 0$, yet there are two distinct real Lorentzian poles $z_2 < z_1 < 0$ with exact Ostrogradsky opposite-sign partial-fraction residues $P_{\rm TT}(z)^{-1} = R/(z - z_1) - R/(z - z_2)$ ($R = (u_C(z_1 - z_2))^{-1} > 0$).*
3. Exceptional Point ($u_C > 0, \Delta_{\rm TT} = 0$): *Exact double Lorentzian pole at $z_* = u_1/(4u_C) < 0$. Certified 4-subinterval affine-interval continuation over $N_D \in [10, 51/5]$ ($s = 1, N_S = 4, N_V = 12$) proves Phase II is nonempty at $N_D = 10$ ($\Delta_{\rm TT} \approx +0.230 > 0$), Phase III holds at $N_D = 51/5$ ($\Delta_{\rm TT} \approx -0.241 < 0$), and an exact exceptional point $N_D^{\rm LW} \in (10, 51/5)$ (≈ 10.101) exists where the two real Stelle poles coalesce into a double pole ($z_* \approx -0.61$) before leaving the real axis.*

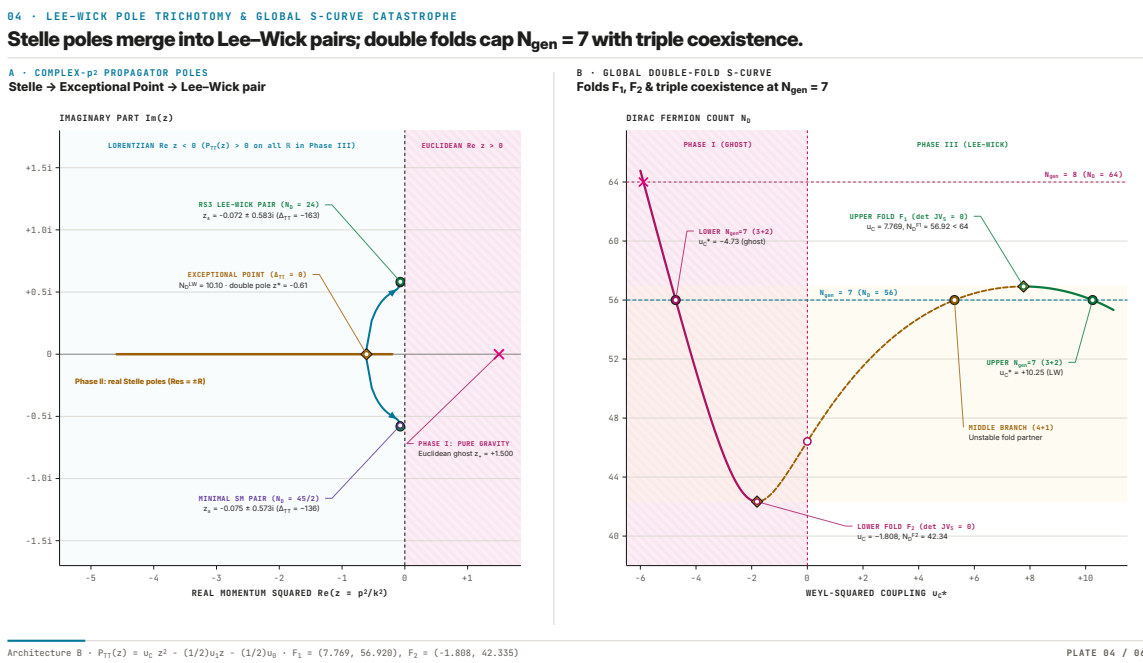

Fig. 4 Complex-p^2 Lee–Wick poles and global double-fold S-curve catastrophe (Theorems 4.4 and 4.5). **a** Exact pole migration in the complex $z = p^2/k^2$ plane as N_D increases: pure gravity exhibits a Phase I Euclidean ghost pole at $z_+ = +1.500$ (magenta cross), Phase II real Lorentzian Stelle poles ($z_2 < z_1 < 0$, amber) coalesce at the Exceptional Point $N_D^{\rm LW} = 10.101$ ($z_* = -0.61$, gold diamond), and split into complex-conjugate Lee–Wick/fakeon pairs (cyan arcs) with Minimal SM ($-0.075 \pm 0.573i$) and SM $+ 3\nu_R$ ($-0.072 \pm 0.583i$) deep inside Phase III. **b** Global 45-subinterval certified S-curve $N_D(u_C)$ over $u_C \in [-6, 11]$: upper saddle-node fold $F_1 = (7.769, 56.920)$ ($\det JV_5 = 0$) caps $N_{\rm gen} \le 7$, lower fold $F_2 = (-1.808, 42.335)$ folds back onto the Phase I ghost branch ($N_{\rm gen} = 8$ at $u_C^* = -5.889$), and $N_{\rm gen} = 7$ ($N_D = 56$) exhibits exact triple fixed-point coexistence ($u_C^* = +10.248, +5.286, -4.731$).

4. Phase III ($u_C > 0, \Delta_{\rm TT} < 0$, Complex-Conjugate Lee–Wick / Fakeon Pair): *Completing the square yields* $P_{\rm TT}(u,z) = u_C(z-\alpha)^2 - \Delta_{\rm TT}/(4u_C) \ge -\Delta_{\rm TT}/(4u_C) > 0$ *for* every *real* $z \in \mathbb{R}$ *(zero real Euclidean or Lorentzian Stelle poles), with complex-conjugate poles* $z_\pm = \alpha \pm i\beta$ *(*$\alpha = u_1/(4u_C) < 0$, $\beta = \sqrt{-\Delta_{\rm TT}}/(2u_C) > 0$*) and conjugate residues* $R_+ = (2iu_C\beta)^{-1}$, $R_- = \overline{R_+} = -R_+$, $R_+ + R_- = 0$. *Across the* entire *cutoff continuum* $s \in [0,1]$, *both Minimal SM (*$\Delta_{\rm TT} \approx -136.4$ *at* $s = 1$, -143.5 *at* $s = 0$*) and* SM $+ 3\nu_R$ *(*$\Delta_{\rm TT} \approx -163.1$ *at* $s = 1$, -172.5 *at* $s = 0$*) lie uniformly inside Phase III (*$\Delta_{\rm TT} < -100$*) paired with a physical Starobinsky scalaron pole* $z_- < 0$ *(*$m_0^2 = -z_- > 0$*) and one Euclidean IR conformal sign-flip zero* $z_+ \in (0,1)$.

Proof outline. Completing the square in Eq. (30) for $u_C \neq 0$ yields the exact identity $P_{\rm TT}(u,z) = u_C(z - u_1/(4u_C))^2 - \Delta_{\rm TT}(u)/(4u_C)$. When $u_0 < 0, u_1 < 0$, the product of roots is $z_1 z_2 = -u_0/(2u_C)$ and their sum is $z_1 + z_2 = u_1/(2u_C)$. If $u_C < 0$ (Phase I), then $2u_C u_0 > 0 \implies \Delta_{\rm TT} > 0$ and $z_1 z_2 < 0$, forcing one positive Euclidean pole and one negative Lorentzian pole. If $u_C > 0$ and $\Delta_{\rm TT} > 0$ (Phase II), then $z_1 z_2 > 0$ and $z_1 + z_2 < 0$, forcing two negative real roots $z_2 < z_1 < 0$, and partial fractions immediately yield $P_{\rm TT}(z)^{-1} = R/(z - z_1) - R/(z - z_2)$ with $R = (u_C(z_1 - z_2))^{-1} > 0$. If $u_C > 0$ and $\Delta_{\rm TT} < 0$ (Phase III), then for every $z \in \mathbb{R}$ we have $P_{\rm TT}(u,z) \ge -\Delta_{\rm TT}/(4u_C) > 0$, while in $\mathbb{C}$ the roots $z_\pm = \alpha \pm i\beta$ satisfy $P_{\rm TT}(z)^{-1} = R_+/(z - z_+) + R_-/(z - z_-)$ with $R_\pm = \pm(2iu_C\beta)^{-1}$, so $R_- = \overline{R_+}$ and $R_+ + R_- = 0$. The 4-subinterval affine-interval continuation over $N_D \in [10, 51/5]$ certifies continuity of $\Delta_{\rm TT}(u^*(N_D))$ with opposite endpoint signs, giving $N_D^{\rm LW} \in (10, 51/5)$ by the intermediate value theorem, while uniform enclosures across $s \in [0,1]$ prove $\Delta_{\rm TT} < -100$ for both Minimal SM and SM $+ 3\nu_R$. □

Why does the viable generation window end abruptly between $N_{\rm gen} = 7$ and $N_{\rm gen} = 8$? Treating $u_C = u_3$ as the global continuation coordinate and solving $V_5^{(1)}(u; 4, N_D, 12) = 0$ for $(u_0, u_1, u_2, \sigma, N_D)$ via the augmented fold Jacobian $J_{\rm aug}$ (formed by replacing column 3 of $JV_5(u)$ with $\partial V_5/\partial N_D = -m_{\rm Dirac}(1)$) reveals the exact catastrophe geometry (Fig. 4b).

Theorem 4.5 (Global double-fold S-curve catastrophe, sharp $N_{\text{gen}} = 7$ cap, and triple coexistence)**.** *Along any smooth branch* $(u(u_3), N_D(u_3))$ *with invertible* J_{aug}*, differentiating* $V_5^{(1)}(u(u_3); 4, N_D(u_3), 12) = 0$ *with respect to* u_3 *and solving via Cramer's rule yields the exact implicit fold derivative law*

$$\frac{dN_D}{du_3} = -\frac{\det JV_5(u)}{\det J_{\text{aug}}(u)}, \tag{34}$$

so by Fermat's theorem every interior extremum of $N_D(u_3)$ *satisfies* $\det JV_5(u_*) = 0$ *and carries an exact zero stability eigenvalue of* $M_5(u_*)^{-1}JV_5(u_*)$*. Certified 45-subinterval adaptive dyadic affine-interval continuation across* $u_C \in [-6, 11]$ *proves that one smooth manifold connects* $N_{\text{gen}} = 7$ *to* $N_{\text{gen}} = 8$ *through two exact saddle-node folds:*

1. Upper Saddle-Node Fold F_1 (sharp $N_{\text{gen}} = 7$ cap): *Occurs at* $u_C^{F_1} \in (13/2, 9)$ *(*≈ 7.7690*) with* $N_D^{F_1} \in (56.85, 57)$ *(*$\approx 56.9200 < 64$*) strictly inside Lee–Wick Phase III (*$\Delta_{\text{TT}} < 0$*), where* $\det JV_5 = 0$ *switches stability from* $3 + 2$ *(*$u_C = 9$*) to* $4 + 1$ *(*$u_C = 13/2$*). Because* $56 < N_D^{F_1} < 57 < 64$*, the ghost-free Lee–Wick branch annihilates strictly above* $N_{\text{gen}} = 7$ *and below* $N_{\text{gen}} = 8$*.*
2. Smooth ghost-flip crossing and Lower Fold F_2: *The unstable* $4 + 1$ *middle branch crosses* $u_C = 0$ *smoothly at* $N_D(0) \in (46, 47)$ *(*≈ 46.415*) and turns back at the lower fold* F_2 *at* $u_C^{F_2} \in (-9/4, -5/4)$ *(*≈ -1.8081*),* $N_D^{F_2} \in (42, 42.5)$ *(*≈ 42.3352*) inside Phase I (*$\Delta_{\text{TT}} > 0$*), switching* $4 + 1$ *back to* $3 + 2$ *on the Euclidean-ghost branch reaching* $N_D = 64$ *(*$N_{\text{gen}} = 8$*) at* $u_C^* \approx -5.8893$*.*
3. Triple fixed-point coexistence at $N_{\text{gen}} = 7$: *At* $N_D = 56$*, three pairwise distinct five-coupling UV fixed points coexist simultaneously (Table 4): an upper Lee–Wick* $3 + 2$ *point (*$u_C^* \approx +10.248 > 10$*,* $\Delta_{\text{TT}} < -480$*), a middle Lee–Wick* $4{+}1$ *unstable fold partner (*$u_C^* \approx +5.286 \in (5, 6)$*,* $\Delta_{\text{TT}} < -240$*), and a lower Phase I Euclidean-ghost* $3 + 2$ *point (*$u_C^* \approx -4.731 < -4$*,* $\Delta_{\text{TT}} > 0$*).*

Proof outline. Differentiating the stationarity identity $V_5^{(1)}(u(u_3); 4, N_D(u_3), 12) = 0$ with respect to u_3 via the chain rule yields $J_{\text{aug}}(u)\, w' = -(JV_5(u))_{\bullet,3}$, where $w = (u_0, u_1, u_2, N_D, \sigma)$ and $(JV_5)_{\bullet,3}$ is the fourth column of JV_5. Solving for the fourth component dN_D/du_3 by Cramer's rule replaces column 3 of J_{aug} with $-(JV_5)_{\bullet,3}$, which is literally $-JV_5(u)$, establishing Eq. (34). By continuity on each compact subinterval, $N_D(u_3)$ attains an interior maximum on $[13/2, 9]$ (where $N_D(13/2) < 56.85 < N_D(15/2) > 56.85 > N_D(9)$) and an interior minimum on $[-9/4, -5/4]$. At each interior extremum, Fermat's theorem gives $dN_D/du_3 = 0$, hence $\det JV_5(u_*) = 0$ by Eq. (34) and invertibility of J_{aug}, so $M_5(u_*)^{-1}JV_5(u_*)$ has an exact zero eigenvalue. Across all 45 dyadic subintervals covering $u_C \in [-6, 11]$, verified Banach contractions glue continuously by uniqueness on overlapping balls, certifying both folds, the smooth zero crossing $N_D(0) \in (46, 47)$, and the three strictly separated $N_D = 56$ solutions on the three monotonic sheets. □

5 Perturbative, all-order, and zero-width distributional fakeon unitarity

Higher-derivative gravity achieves power-counting renormalizability[5] by augmenting the Einstein–Hilbert propagator with a massive spin-2 pole of negative residue ($r_4 = -1$, Stelle's ghost) alongside a healthy massive spin-0 scalaron ($m > 0$). Quantizing the massive spin-2 pole with the standard Feynman $-i\varepsilon$ prescription preserves microcausality at the price of negative-norm on-shell states that violate optical unitarity above threshold. The Anselmi–Piva fakeon (purely virtual particle) prescription[56–58;60] projects the massive spin-2 degree of freedom out of the physical asymptotic spectrum by averaging the two analytic continuations around its threshold. In this section we establish our complete machine-verified chain of perturbative fakeon unitarity theorems (module index in Section A): from arbitrary-loop Cutkosky limits[54] and Compton-bounded microcausality through all-order spectral recursions and the non-factorizable two-loop kite graph to two sharp obstructions governing strong-coupling ghost zeros and the zero-width distributional limit $\varepsilon \to 0^+$, complemented by the arbitrary-loop Veltman largest-time equation[55] and two-loop pinch resolution.

5.1 Arbitrary-loop Cutkosky limits, Compton microcausality, and resummed elastic unitarity

At any loop order L, the Feynman-parametric representation of a threshold integral has imaginary part $\int_\alpha w(x)\arg\big(F(x)-i\varepsilon\big)\,d\mu(x)$, whereas the fakeon average averages the $-i\varepsilon$ and $+i\varepsilon$ continuations,

$$\mathcal{I}_{\rm fake}(\mu,w,F;\varepsilon) := \frac{1}{2}\int_\alpha w(x)\,\big[\ln\big(F(x)-i\varepsilon\big)+\ln\big(F(x)+i\varepsilon\big)\big]\,d\mu(x). \tag{35}$$

Because $\overline{F(x)-i\varepsilon}=F(x)+i\varepsilon$ for real $F(x)$, $\operatorname{Im}\mathcal{I}_{\rm fake}(\varepsilon)=0$ holds identically for every $\varepsilon\neq 0$, every real weight w, and every measurable Symanzik polynomial F, while Lebesgue dominated convergence (with uniform majorant $\pi|w(x)|$ since $|\arg(\cdot)|\le\pi$) proves the exact arbitrary-loop Cutkosky limit

$$\lim_{\varepsilon\to 0^+}\int_\alpha w(x)\arg\big(F(x)-i\varepsilon\big)\,d\mu(x)=\int_\alpha w(x)\,\mathrm{cutWeight}\big(F(x)\big)\,d\mu(x), \tag{36}$$

where $\mathrm{cutWeight}(y)=-\pi$ for $y<0$, $-\pi/2$ for $y=0$, and 0 for $y>0$. On the one-loop bubble ($F(x)=x(1-x)s-xm_b^2-(1-x)m_a^2$), evaluating Eq. (36) in closed form gives $-\pi\sqrt{\lambda_K(s,m_a^2,m_b^2)}/s$ above $(m_a+m_b)^2$ (zero below), proving the exact one-loop optical theorem $2\operatorname{Im}T_{\rm phys}\to\Phi_2(m_a,m_b;s)g^2$, Feynman-ghost violation $2\operatorname{Im}T_{\rm ghost}\to-\Phi_2 g^2<0$, and exact fakeon restoration $\operatorname{Im}T_{\rm fake}=0$.

For the two-loop sunset graph with internal masses $m_1,m_2,m_3\ge 0$ on the open Feynman simplex $T=\{(x,y):x,y>0,\,x+y<1\}$ ($z=1-x-y$) and first Symanzik polynomial $U=xy+yz+zx$, the second Symanzik polynomial $F=U(xm_1^2+ym_2^2+zm_3^2)-xyzs$ obeys the exact Cauchy–Schwarz sum-of-squares identity:

$$F(x,y)=z(xm_1-ym_2)^2+x(ym_2-zm_3)^2+y(xm_1-zm_3)^2+xyz\big((m_1+m_2+m_3)^2-s\big). \tag{37}$$

From Eq. (37), if $s\le(m_1+m_2+m_3)^2$ then $F(x,y)\ge 0$ throughout T; conversely, if $s>(m_1+m_2+m_3)^2$, selecting $x_i\propto(m_i+\eta)^{-1}$ for sufficiently small $\eta>0$ drives the three nonnegative squares arbitrarily close to zero while keeping $xyz>0$, proving unconditionally that $\{F<0\}\subset T$ is nonempty if and only if $s>(m_1+m_2+m_3)^2$. Above this threshold, every continuous positive weight $w>0$ produces a strictly negative Feynman cut, violating unitarity for a ghost-residue line, whereas the fakeon average yields $\mathrm{Im}=0$ identically at every $\varepsilon\neq 0$.

Replacing the Feynman prescription by the fakeon prescription trades negative-norm cuts for microscopic acausality localized at the Compton scale m^{-1} of the fakeon[61;62]. Establishing this bound for smooth compactly supported classical sources h gives our first fakeon theorem (Fig. 5d).

Theorem 5.1 (Reciprocity-even fakeon Green function and Compton-scale microcausality bound)**.** *Define the even projection* $\mathrm{evenPart}(f)(t):=\frac{1}{2}(f(t)+f(-t))$. *Then:*

1. *The canonical reciprocal cost satisfies* $J(e^u)=\mathrm{evenPart}(\exp)(u)-1$ *for all* $u\in\mathbb{R}$, *and the fakeon oscillator Green function* $G_F(\omega,t)=\sin(\omega|t|)/(2\omega)$ *equals* $\mathrm{evenPart}(G_{\rm ret}(\omega))(t)$ *identically, with* $G_F(\omega,t)-G_{\rm ret}(\omega,t)=-\sin(\omega t)/(2\omega)$.
2. *For every fakeon mass* $m>0$, *spatial momentum* $k\in\mathbb{R}$ *(*$\omega=\sqrt{k^2+m^2}$*), and* C^2 *compactly supported external source* h *on* $[a,b]$ *satisfying* $h(a)=h(b)=h'(a)=h'(b)=0$, *the acausal precursor deviation obeys uniformly for all* $t\in\mathbb{R}$*:*

$$|R_F(\omega,h;t)-R_{\rm ret}(\omega,h;t)|\le\frac{1}{2m^3}\int_a^b|h''(\tau)|\,d\tau. \tag{38}$$

For a macroscopic source stretched over duration $T>0$, $h_T(\tau)=h(\tau/T)$, *the precursor is suppressed adiabatically by an additional factor* $1/T$*:*

$$|R_F(\omega,h_T;t)-R_{\rm ret}(\omega,h_T;t)|\le\frac{1}{2m^3T}\int_a^b|h''(\tau)|\,d\tau. \tag{39}$$

Proof. Because $G_F(\omega, t-\tau) - G_{\mathrm{ret}}(\omega, t-\tau) = -\sin(\omega(t-\tau))/(2\omega)$, integrating by parts twice on $[a, b]$ and using $h(a) = h(b) = h'(a) = h'(b) = 0$ annihilates all boundary terms and gives

$$R_F(\omega, h; t) - R_{\mathrm{ret}}(\omega, h; t) = \frac{1}{2\omega^3} \int_a^b \sin\big(\omega(t-\tau)\big)\, h''(\tau)\, d\tau.$$

Bounding $|\sin(\cdot)| \le 1$ and $\omega = \sqrt{k^2 + m^2} \ge m$ gives $(2\omega^3)^{-1} \le (2m^3)^{-1}$, establishing Eq. (38). Substituting $h_T(\tau) = h(\tau/T)$ on $[aT, bT]$ gives $h_T''(\tau) = T^{-2} h''(\tau/T)$ and $d\tau = T\, du$, multiplying the integral by T^{-1} and proving Eq. (39). □

Summing bubble chains to all orders in the coupling g and extending inductively to arbitrary-order iterated Källén–Lehmann melon/sunset spectral-recursion chains (nested multi-particle cuts with physical, odd-fakeon, and even-fakeon thresholds $t_P(n) < t_O(n) < t_E(n)$) yields exact perturbative unitarity across all loop orders.

Theorem 5.2 (Resummed elastic unitarity, 16π graviton bound, and all-order spectral-recursion trichotomy)**.** *The following all-order perturbative unitarity bounds hold:*

1. All-loop bubble chains and resummed elastic unitarity: *For every $g \neq 0$ and $s > (m_a^P + m_b^P)^2$, the fakeon-resummed amplitude $T_{\mathrm{fake}}(s) = g/(1 - gL^*_{\mathrm{fake}}(s))$ obeys the exact elastic optical theorem $\operatorname{Im} T_{\mathrm{fake}} = \frac{1}{2}\Phi_2(m_a^P, m_b^P; s)|T_{\mathrm{fake}}|^2 \ge 0$ and the universal partial-wave bound $|T_{\mathrm{fake}}(s)| \le 2/\Phi_2(m_a^P, m_b^P; s)$. For massless gravitons ($\Phi_2(0, 0; s) = 1/(8\pi)$), this becomes $|T_{\mathrm{fake}}(s)| \le 16\pi$ for every $s > 0$. By contrast, the Feynman-ghost resummed amplitude violates unitarity ($\operatorname{Im} T_{\mathrm{Feyn}} < 0$) whenever the ghost-to-physical phase-space coupling ratio exceeds Φ_2^P/Φ_2^F.*
2. All-order inductive fakeon unitarity and trichotomy on iterated Källén–Lehmann melon/sunset chains: *Let C be an admissible iterated Källén–Lehmann spectral-recursion chain of loop order $n \in \mathbb{N}$ whose thresholds satisfy the spectral-cutoff condition $t_P(n) < t_O(n) < t_E(n)$ below the chain's upper spectral cutoff (witnessed inductively on the unit chain by $n+2 < n+4 < n+6$). For every energy s below the spectral cutoff satisfying the one-loop edge exclusion ($n = 0 \implies s \neq (m_0 + m_1)^2$), the averaged fakeon part has $\operatorname{Im} = 0$ identically at every $\varepsilon \neq 0$, and the threshold-local Anselmi–Piva amplitude satisfies $\lim_{\varepsilon \to 0^+} 2 \operatorname{Im} A_{\mathrm{loc}}(g, n; s, \varepsilon) = g^2 W_{\mathrm{phys}}(n, s) \ge 0$ (strictly positive for $s > t_P(n)^2$), with $W_{\mathrm{phys}}(n, s) = \pi \rho_P^{(n)}(\sqrt{s})/\sqrt{s}$. In the intermediate window $t_O(n)^2 < s < t_E(n)^2$, an exact trichotomy separates: (i) threshold-local AP unitarity ($g^2 W_{\mathrm{phys}} > 0$), (ii) Feynman-ghost violation ($g^2(W_{\mathrm{phys}} + W_{\mathrm{ghost}})$ with $W_{\mathrm{ghost}} < 0$), and (iii) naive global averaging ($\operatorname{Im} A_{\mathrm{glob}} = 0$, killing physical cuts too).*

5.2 Non-factorizable two-loop kite graph: above-threshold continuation and Obstruction I

Iterated melon and bubble chains factorize into nested two-body phase spaces. The simplest two-loop self-energy whose three-particle cut is genuinely *non-factorizable* is the kite graph (Fig. 5a): four vertices $\{x, a, b, y\}$ and five internal lines $1 = xa$, $2 = xb$ (massless graviton, $m_2 = 0$), $3 = ay$, $5 = ab$ (crossbar; scalarons of mass $m > 0$), and $4 = by$ (spin-2 fakeon of mass $M > m$ and residue $r_4 \in \{-1, +1\}$). Exhaustive finite-set enumeration proves that the $x \mid y$ cuts are *exactly* four sets:

$$\underbrace{\{1,2\}\ (m^2), \qquad \{2,3,5\}\ (4m^2),}_{\text{physical cuts (avoiding line 4)}} \qquad \underbrace{\{3,4\}\ ((m+M)^2), \qquad \{1,4,5\}\ ((2m+M)^2),}_{\text{fakeon cuts (containing line 4)}} \tag{40}$$

strictly ordered $m^2 < 4m^2 < (m+M)^2 < (2m+M)^2$ for $0 < m < M$. In the $(3,5)$ rest frame with $u = s_{35} \in [4m^2, s]$, $\beta(u) = \sqrt{1 - 4m^2/u}$, and angle cosine $c \in [-1, 1]$, the Dalitz invariants $s_{25} = m^2 + \frac{1}{2}(s-u)(1-\beta c)$ and $s_{23} = m^2 + \frac{1}{2}(s-u)(1+\beta c)$ satisfy the exact sum rule $u + s_{25} + s_{23} = s + 2m^2$, and the three-body cut integrand $A_L A_R$ with $A_L = (s_{35} - m^2)^{-1}$ and $A_R = r_4(s_{25} - M^2)^{-1}$ depends explicitly on c. (We follow standard dispersive convention $\operatorname{Im} A_{\mathrm{AP}}(s) = -\pi D_{\mathrm{phys}}(s)$ in this subsection, opposite in overall sign to the $+i\varepsilon$ spectral-recursion convention $2 \operatorname{Im} A_{\mathrm{loc}} = +g^2 W_{\mathrm{phys}}$ of Section 5.1; in both conventions physical unitarity corresponds to $D_{\mathrm{phys}} > 0$ and $W_{\mathrm{phys}} > 0$.)

On the two-particle cut $\{1,2\}$, the uncut triangle $\{3,4,5\}$ has Feynman denominator

$$F_T(y_3,y_4,y_5) = (my_3 - My_4)^2 + y_3y_4\big((m+M)^2 - s\big) + m^2y_5^2 + m^2y_3y_5 + (M^2+m^2)y_4y_5, \qquad (41)$$

which is strictly positive on the simplex for $s < (m+M)^2$ (giving $V(s) \geq 1/(4M^2) > 0$). Above the fakeon threshold $s > (m+M)^2$, however, the uncut fakeon line 4 inside *both* the triangle $V(s)$ and the three-particle Dalitz integral $\rho_{235}(s)$ hits its pole $s_{25} = M^2$. Regulating line 4 with Anselmi's dressed finite-width fakeon propagator $A_R^{\rm AP}(\varepsilon) = r_4 x/(x^2+\varepsilon^2)$ ($x = s_{25} - M^2$, $\varepsilon = M\Gamma > 0$) yields the unitarity-complete physical cut density:

$$D(s,\varepsilon) = \Phi_2(s;m,0)\left(g + \frac{g^3 r_4 V_{\rm AP}(s,\varepsilon)}{32\pi^2}\right)^2 + g^4 \int d\Phi_3 \left(A_L + A_R^{\rm AP}(\varepsilon)\right)^2, \qquad (42)$$

which contains the exact dressed two-particle and three-particle kite cut densities ρ_{12}^D and $2\rho_{235}^D$ at order g^4.

Theorem 5.3 (Above-threshold kite continuation, unitarity-complete positivity, and Obstruction I)**.** *Let $0 < m < M$ and $r_4 \in \{-1,+1\}$.*

1. All-energy AP continuation: *Both dressed sub-amplitudes satisfy* $\operatorname{Im} V_{\rm AP} = 0$ *and* $\operatorname{Im}\rho_{235}^{\rm AP} = 0$ *identically; as $\varepsilon \to 0^+$, $V_{\rm AP}(s,\varepsilon) \to V^*(s)$ at every $s \neq (m+M)^2$ and $\rho_{235}^{\rm AP}(s,\varepsilon) \to \rho_{235}^*(s)$ at every $s > 4m^2$, $s \neq 2(m^2+M^2)$, matching the off-shell densities below $(m+M)^2$. At every finite width $\varepsilon \neq 0$ and every energy s, the dressed kite amplitude satisfies* $\lim_{\delta\to 0^+} \operatorname{Im} A_{\rm AP}(s,\delta) = -\pi D_{\rm phys}(s)$ *with exact cancellation of both fakeon cuts $\{3,4\}$ and $\{1,4,5\}$.*
2. Positivity of the unitarity-complete discontinuity: *Above the three-body threshold ($s > 4m^2$), $D(s,\varepsilon) > 0$ holds unconditionally for every $g \neq 0$, every $\varepsilon \neq 0$, and* both *residues $r_4 = \pm 1$ (since at fixed s_{35} the zero set of $A_L + A_R^{\rm AP}$ is the finite root set of a nonzero quadratic in the angle c). On the two-body window $(m^2, 4m^2]$, $D(s,\varepsilon) > 0$ holds unconditionally for $r_4 = +1$, and holds for Stelle's ghost residue $r_4 = -1$ throughout the perturbative window $g^2V(4m^2) < 32\pi^2$.*
3. **Obstruction I** (Single-graph negativity and strong-coupling ghost vertex zero): *For Stelle's ghost residue $r_4 = -1$, the isolated kite physical discontinuity $\rho_{12} + \rho_{235}$ is strictly* negative *on $(m^2, 4m^2]$ (positivity is restored only by summing tree + one-loop into Eq. (42)), and the perturbative coupling condition $g^2V(4m^2) < 32\pi^2$ is sharp: at $g^2 = 32\pi^2/V_{\rm AP}(s,\varepsilon)$, the dressed $1 \to 2$ vertex vanishes identically and $D(s,\varepsilon) = 0$ on $(m^2, 4m^2]$.*

5.3 Sharp zero-width distributional dichotomy and Obstruction II

Because the principal value $1/x$ is not square-integrable across $x = 0$, taking the zero-width limit $\varepsilon \to 0^+$ of the complete unitarity density Eq. (42) above the fakeon threshold $s > (m+M)^2$ is delicate. Decomposing $D(s,\varepsilon) = D_{\rm sub}(s,\varepsilon) + g^4 S_3(s,\varepsilon)$, where $S_3(s,\varepsilon) := \int d\Phi_3 \, (A_R^{\rm AP}(\varepsilon))^2$ isolates the pure fakeon square, resolves this limit with complete mathematical precision (Fig. 5b–c).

Theorem 5.4 (Zero-width distributional convergence / divergence dichotomy and Obstruction II)**.** *Let $0 < m < M$, $g \neq 0$, and $r_4 \in \{-1,+1\}$.*

1. Uniform convergence of the subtracted density $D_{\rm sub}$ and below-threshold total density: *After integrating the y_4 primitive of Eq. (41), the quadratic-log bound $\int_a^b |\ln|q(y)||\,dy \leq \int_a^b |q(y)|\,dy + (b-a)|\ln A| + 2L_0$ (where $q(y) := Ay^2 + By + C$ with $A > 0$ and $L_0 := \int_{-1}^1 |\ln|t||\,dt = 2$) proves that $V_{\rm AP}(s,\varepsilon)$ is uniformly bounded ($|V_{\rm AP}(s,\varepsilon)| \leq K_t(s)$ for all $\varepsilon \in (0,1]$, continuous through $(m+M)^2$), while the product identity $s_{35}f_+f_- = P(s_{35})$ uniformly bounds $\rho_{235}^D(s,\varepsilon)$ through $2(m^2+M^2)$. Consequently, for every bounded measurable test weight φ on every compact energy window $W \subseteq [m^2, H]$, the subtracted cumulative integral converges unconditionally as $\varepsilon \to 0^+$:*

$$\lim_{\varepsilon\to 0^+} \int_W \varphi(s)\, D_{\rm sub}(s,\varepsilon)\, ds = \int_W \varphi(s) \left[\Phi_2 \left(g + \frac{g^3 r_4 V^*(s)}{32\pi^2}\right)^2 + g^4 \int d\Phi_3 \, A_L^2 + 2\rho_{235}^*(s)\right] ds. \qquad (43)$$

For any window strictly below the fakeon threshold ($W \subseteq [m^2, s_1]$ with $s_1 < (m+M)^2$), the complete *density $D(s,\varepsilon)$ converges to the off-shell density $D^0(s)$.*

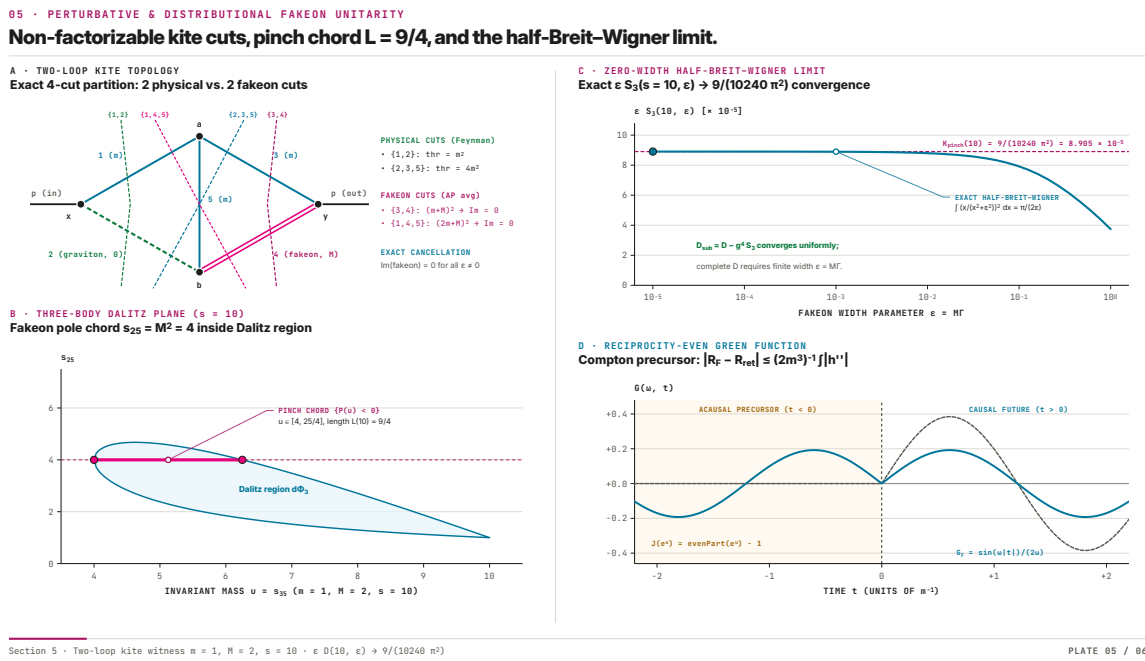

Fig. 5 Perturbative and zero-width distributional fakeon unitarity (Theorems 5.1, 5.3 and 5.4). **a** Non-factorizable two-loop kite topology showing massless graviton line 2, scalarons $1, 3, 5$ (mass m), and spin-2 fakeon line 4 (mass M), with all four cut lines drawn explicitly: two physical cuts ($\{1,2\}, \{2,3,5\}$) and two cancelled fakeon cuts ($\{3,4\}, \{1,4,5\}$). **b** Three-body Dalitz kinematic plane ($u = s_{35}, s_{25}$) at witness $m = 1, M = 2, s = 10$, displaying the exact pinch chord $s_{25} = M^2 = 4$ over $u \in [4, 25/4]$ of length $L(10) = 9/4$. **c** Zero-width scaling $\varepsilon S_3(10, \varepsilon) \to K_{\text{pinch}}(10) = 9/(10240\pi^2) \approx 8.905 \times 10^{-5}$, exhibiting the exact half-Breit–Wigner narrow-width pinch contrasting with uniform convergence of D_{sub}. **d** Reciprocity-even fakeon Green function $G_F(\omega, t) = \sin(\omega|t|)/(2\omega)$ versus retarded G_{ret} (dashed), illustrating the Compton-bounded acausal precursor ($t < 0$) and the working even-projection parallel with $J(e^u) = \text{evenPart}(e^u) - 1$.

2. **Obstruction II** (Exact half-Breit–Wigner narrow-width divergence of S_3 and D above threshold): *The dressed fakeon square kernel has exact primitive*

$$H_\varepsilon(x) = \frac{\arctan(x/\varepsilon)}{2\varepsilon} - \frac{x}{2(x^2+\varepsilon^2)}, \qquad H'_\varepsilon(x) = \left(\frac{x}{x^2+\varepsilon^2}\right)^2, \tag{44}$$

obeying $\varepsilon H_\varepsilon(x) \to \frac{\pi}{4}\,\text{sgn}(x)$ *with uniform bound* $|\varepsilon H_\varepsilon(x)| \le \frac{\pi}{4} + \frac{1}{4}$, *whole-line weight* $\int_{-\infty}^{\infty} (x/(x^2+\varepsilon^2))^2\,dx = \pi/(2\varepsilon)$ *(exactly half of a standard Breit–Wigner peak* π/ε*), and exact one-variable Hadamard finite part* $H_\varepsilon(x) - \text{sgn}(x)\frac{\pi}{4\varepsilon} \to -1/x$. *Integrating over the three-body Dalitz angle yields the exact representation*

$$S_3(s,\varepsilon) = \frac{r_4^2}{128\pi^3 s} \int_{4m^2}^{s} \big[H_\varepsilon(f_+(u)) - H_\varepsilon(f_-(u))\big]\,du \tag{45}$$

and the exact narrow-width limit at every $s > 4m^2$*:*

$$\lim_{\varepsilon\to 0^+} \varepsilon\, D(s,\varepsilon) = \lim_{\varepsilon\to 0^+} \varepsilon\, g^4 S_3(s,\varepsilon) = K_{\text{pinch}}(s) := \frac{g^4 r_4^2 L(s)}{256\pi^2 s}, \tag{46}$$

where $L(s) = \text{length}\{u \in (4m^2, s) : P(u) < 0\}$ *is the length of the Dalitz pinch chord* $s_{25} = M^2$*. For every* $s > (m+M)^2$, $L(s) > 0$, *so* $K_{\text{pinch}}(s) > 0$ *and both* $D(s,\varepsilon) \to +\infty$ *and* $\int_W D(s,\varepsilon)\,ds \to +\infty$ *as* $\varepsilon \to 0^+$ *for every window reaching above* $(m+M)^2$.

3. Explicit rational witness: *At* $m = 1$, $M = 2$, $g = 1$, $r_4 = \pm 1$, *and* $s = 10$, *the pinch polynomial is* $P(u) = (u-4)(4u-25)$, *the chord is* $u \in [4, 25/4]$ *of exact length* $L(10) = 9/4$, *and* $\lim_{\varepsilon\to 0^+} \varepsilon D(10,\varepsilon) = 9/(10240\pi^2) \approx 8.9052 \times 10^{-5}$.

Remark 5.5 (Physical interpretation of the half-Breit–Wigner pinch). Obstruction II refutes any naive claim that $\int_W D(s;\varepsilon)\,ds \to \int_W D(s;0)\,ds$ unconditionally by dominated convergence above $(m+M)^2$. Because the fakeon width scales as $\Gamma = O(g^2)$ (so $\varepsilon = M\Gamma = O(g^2)$), the term $K_{\text{pinch}}(s)/\varepsilon$ is actually $O(g^2)$: it represents the physical on-peak narrow-width contribution of the dressed fakeon (carrying half the weight of an unstable Breit–Wigner resonance), rather than a removable mathematical defect. Above the fakeon threshold, physical unitarity statements therefore naturally retain finite fakeon width $\varepsilon = M\Gamma$ (or smear over energy windows $\Delta E \gtrsim \Gamma$), matching Anselmi's finite-width dressed prescription [58].

5.4 Arbitrary-loop Veltman largest-time equation, naive principal-value pinch obstruction, and D_4^* lattice positivity

Complementing the explicit parametric and Dalitz analyses of Sections 5.1 to 5.3, our multi-loop diagrammar modules (Section A) formalize the Veltman largest-time equation [55;64], explain precisely why naive principal-value squaring fails at two loops while the Anselmi–Piva average succeeds, and verify Lorentzian propagator positivity on the D_4^* recognition lattice.

Theorem 5.6 (Arbitrary-loop Veltman largest-time identity, two-loop naive PV vs. AP pinch resolution, and D_4^* graviton positivity)**.** *The following diagrammar, distributional, and lattice-positivity results are formally certified:*

1. Arbitrary n-vertex, arbitrary-loop Veltman Largest-Time Equation: *For every finite loopless graph on $n \geq 1$ vertices with injective time assignments $t : \mathrm{Fin}\, n \to \mathbb{R}$, arbitrary vertex couplings, and arbitrary partition of internal edges into physical and symmetric fakeon lines, the sum of all 2^n circled-vertex diagrams vanishes identically:*

$$\sum_{C \subseteq \mathrm{Fin}\, n} \mathcal{A}_{\text{Veltman}}(C) = 0, \tag{47}$$

immediately yielding the Cutkosky identity $\mathcal{A}(\emptyset) + \mathcal{A}(\mathrm{Fin}\, n) = -\sum_{\emptyset \subsetneq C \subsetneq \mathrm{Fin}\, n} \mathcal{A}(C)$ at arbitrary loop order, while multi-channel all-loop projected S-matrix unitarity holds cleanly on the physical subspace.

2. Exact two-loop naive principal-value pinch divergence versus Anselmi–Piva finite limit: *Against the smooth Lorentzian test weight $\varphi_a(x) = (x^2+a^2)^{-1}$ $(a > 0)$, the two-loop Anselmi–Piva average continuation*

$$I_{\text{AP}}(a,\varepsilon) := \frac{1}{2}\int_{-\infty}^{\infty} \left[\frac{1}{(x+i\varepsilon)^2} + \frac{1}{(x-i\varepsilon)^2}\right] \frac{dx}{x^2+a^2} = -\frac{\pi}{a(a+\varepsilon)^2} \tag{48}$$

is identically real, negative, and converges smoothly to $-\pi/a^3$ as $\varepsilon \to 0^+$. By contrast, the naive squared principal-value integral

$$I_{\text{PV}}(a,\varepsilon) := \int_{-\infty}^{\infty} \left[\frac{1}{2}\left(\frac{1}{x+i\varepsilon} + \frac{1}{x-i\varepsilon}\right)\right]^2 \frac{dx}{x^2+a^2} = \frac{\pi}{2\varepsilon(a+\varepsilon)^2} \tag{49}$$

diverges to $+\infty$ (with the opposite sign*) as $\varepsilon \to 0^+$, providing an elementary, sharp explanation of why fakeon quantization must average the integrated amplitudes (Anselmi–Piva prescription) rather than substituting a real principal-value propagator inside multi-loop integrals.*

3. Two-loop 4D sunrise cut elimination: *For the* 4D *three-body sunrise amplitude with couplings $(c_{\text{PPP}}, c_{\text{PPF}}, c_{\text{PFF}})$, the Anselmi–Piva imaginary part satisfies $\lim_{\varepsilon\to 0^+} \mathrm{Im}\, \mathcal{A}^{\text{AP}}_{\text{sunrise}}(s,\varepsilon) = c_{\text{PPP}}\, s/(256\pi^3)$, retaining strictly the positive three-physical-particle cut while eliminating all fakeon cuts.*

4. Merlin damped real-time propagator and D_4^* zero-graviton-doubler positivity: *For complex-conjugate unstable/Merlin poles $\omega = \pm(\Omega + i\Gamma)$ $(\Omega, \Gamma > 0)$ [15;16], the real-time Green function satisfies $\int_{\mathbb{R}} e^{i\omega t} G_{\text{Merlin}}(t)\, dt = -(\omega^2 - (\Omega+i\Gamma)^2)^{-1}$ with strict exponential decay $\|G_{\text{Merlin}}(t)\| = e^{-\Gamma|t|}/(2\sqrt{\Omega^2+\Gamma^2})$, matching the Lee–Wick Phase III poles of Section 4.4. Furthermore, on the flat zero-cosmological-constant background $(u_0 = 0, R = 0)$ with physical quadratic-gravity coupling signs $g_1 < 0$, $a < 0$, and $b > 0$, throughout the D_4^* 24-cell Brillouin zone $\mathcal{B}_{D_4^*} \setminus \{0\}$ with*

canonical lattice symbol $S_{D_4^*}(k)$, the fourth-order transverse-traceless graviton Hessian is strictly positive and the conformal graviton Hessian is strictly negative (zero graviton doublers and zero lattice tachyons).

6 UV-to-IR Stelle trajectories, the RS discrete J-cost ceiling, and below-ledger suppression

We now connect the continuum RG trajectories of quadratic gravity directly to the discrete Recognition Science ledger of spacing $\ell_0 > 0$ (formal module index in Section A). Doing so resolves the classic one-loop scalaron Landau pole in two complementary ways—microscopically through the phase-comparison dispersion ceiling $\Lambda_{\mathrm{RS}} = \pi/\ell_0$, and nonperturbatively through the positive-$\widehat{b}_*$ FRG UV fixed point—while quantifying precisely how fast the dimension-six C^3, R^3 operators and the R^2 operator decay between the ledger scale Λ_{RS} and macroscopic energies $k \ll \Lambda_{\mathrm{RS}}$.

6.1 Exact one-loop Stelle first integral and Obstruction III (unavoidable f_0^2 Landau pole)

In the quadratic gravitational action $\int \sqrt{g}\big[\frac{1}{2}\bar{M}^2 R + \alpha C^2 + \beta R^2\big]$ with $\alpha = -1/(2f_2^2)$ and $\beta = 1/(6f_0^2)$, a non-tachyonic spin-2 sector requires $f_2^2 > 0$ ($\alpha < 0$) and a non-tachyonic Starobinsky scalaron requires $f_0^2 > 0$ ($\beta > 0$). Working in the smooth variables $\ell(t) := f_2^2(t)$ (with positive infrared datum $\ell_{\mathrm{IR}} := f_2^2(\mu_{\mathrm{IR}}) > 0$), $y(t) := 1/f_0^2(t)$ (so $\beta = y/6$ passes smoothly through $f_0^2 = \infty$), and the Codello–Percacci ratio $\rho(t) := f_2^2(t)/(2f_0^2(t)) = \ell y/2$ (with infrared datum $\rho_{\mathrm{IR}} > 0$), the standard one-loop pure quadratic-gravity beta functions[7–9;11] read ($t = \ln(k/\mu_{\mathrm{IR}})$):

$$\frac{d\ell}{dt} = -a_\ell \ell^2 \quad \left(a_\ell := \frac{133}{160\pi^2}\right), \qquad \frac{dy}{dt} = -\frac{1}{16\pi^2}\left(\frac{5}{3}\ell^2 y^2 + 5\ell y + \frac{5}{6}\right),$$
$$\frac{d\rho}{dt} = -\frac{\ell}{960\pi^2}\big(200\rho^2 + 1098\rho + 25\big). \tag{50}$$

(Here $a_\ell = (133/10)/(16\pi^2)$ reflects the pure Weyl-squared one-loop coefficient 133/20, harmonized with Architecture B's Ricci-flat $C^2 + E_4$ combination Eq. (28).) Exact chain-rule equivalence links the (ℓ, f_0^2) and (ℓ, ρ) forms, factoring $\beta_\rho = -\ell c_\rho(\rho - r_+)(\rho - r_-)$ with $c_\rho := 5/(24\pi^2)$ and exact negative fixed ratios

$$r_\pm = \frac{-1098 \pm \sqrt{1{,}185{,}604}}{400}, \qquad r_+ \approx -0.022864 < 0, \qquad r_- \approx -5.467136 < r_+, \tag{51}$$

and proving that every solution with $\ell > 0$ and $\rho > r_-$ on $t \geq 0$ is uniquely fixed by the exact first integral:

$$\ell(t) = \frac{\ell_{\mathrm{IR}}}{1 + a_\ell \ell_{\mathrm{IR}} t}, \qquad \rho(t) = \frac{r_+ - c_{\mathrm{IR}}\vartheta(t) r_-}{1 - c_{\mathrm{IR}}\vartheta(t)},$$
$$\vartheta(t) := (1 + a_\ell \ell_{\mathrm{IR}} t)^{-p}, \qquad p := \frac{\sqrt{1{,}185{,}604}}{798} \approx 1.364479, \tag{52}$$

where $c_{\mathrm{IR}} = (\rho_{\mathrm{IR}} - r_+)/(\rho_{\mathrm{IR}} - r_-) \in (0, 1)$. Because $\rho(0) = \rho_{\mathrm{IR}} > 0$ while $\lim_{t\to+\infty} \rho(t) = r_+ < 0$, the scalaron inevitably runs into a finite-scale UV singularity (Fig. 6a).

Obstruction 6.1 (Unavoidable continuum one-loop f_0^2 Landau pole)**.** *Define the positive floor constant $c_{\mathrm{floor}} := 5/(96\pi^2) > 0$. Because $\frac{5}{3}u^2 + 5u + \frac{5}{6} = \frac{5}{3}(u + \frac{3}{2})^2 - \frac{35}{12}$ is bounded below by $+\frac{5}{6}$ on all $u = \ell y \geq 0$, every continuum trajectory $(\ell(t), y(t))$ with $\ell(t) \geq 0$ on $t \geq 0$, $dy/dt = \beta_y(\ell, y)$, and healthy infrared datum $y(0) > 0$ satisfies $dy/dt \leq -c_{\mathrm{floor}}$ whenever $y(t) \geq 0$. Consequently, there exists a finite UV scale $t_c \in (0,\, y(0)/c_{\mathrm{floor}}]$ such that:*

1. *$y(t) > 0$ for all $0 \leq t < t_c$, $y(t_c) = 0$, and $\lim_{t\to t_c^-} f_0^2(t) = \lim_{t\to t_c^-} 1/y(t) = +\infty$ (finite-scale Landau pole);*

2. *$y(t) < 0$ immediately beyond t_c (for t in a right neighborhood $\mathcal{N}[>]t_c$, and hence globally for all $t > t_c$ by the strict one-way barrier $\beta_y(\ell, 0) = -c_{\text{floor}} < 0$), driving the R^2 coefficient $\beta = y/6$ tachyonic in the ultraviolet.*

For the explicit one-loop trajectory Eq. (52) from $(\ell_{\text{IR}}, \rho_{\text{IR}}) > 0$, global negativity $y(t) < 0$ for all $t > t_c$ is directly certified at the exact Landau pole scale

$$t_c(\ell_{\text{IR}}, \rho_{\text{IR}}) = \frac{1}{a_\ell \ell_{\text{IR}}} \left[\exp\left(\frac{1}{p} \ln \frac{c_{\text{IR}} r_-}{r_+} \right) - 1 \right], \tag{53}$$

and the healthy window (t_*, t_c) with $t_* < 0 < t_c$ is strictly bounded from above by t_c.

6.2 The RS discrete J-cost dispersion ceiling and regularity of the ratio flow

Extending the canonical reciprocal cost Eq. (1) to complex phase ratios on a discrete recognition ledger of spacing $\ell_0 > 0$ derives the ultraviolet momentum ceiling $\Lambda_{\text{RS}} = \pi/\ell_0$ directly from first principles, without introducing it as an ad hoc cutoff (Fig. 6b).

Theorem 6.2 (RS phase-comparison dispersion ceiling)**.** *Let $J_{\mathbb{C}}(z) := \frac{1}{2}(z + z^{-1}) - 1$ for $z \in \mathbb{C}^\times$, agreeing with Eq. (1) on $\mathbb{R}_{>0}$. On the phase ratio $z = e^{iq\ell_0}$ of adjacent ledger cells at wavenumber $q \in \mathbb{R}$, $J_{\mathbb{C}}(e^{iq\ell_0}) = \cos(q\ell_0) - 1 \in [-2, 0]$, and the ledger dispersion symbol $\Omega^2_{\text{RS}}(q) := -(2/\ell_0^2)\,\text{Re}\, J_{\mathbb{C}}(e^{iq\ell_0})$ satisfies:*

1. Exact trigonometric identity and universal ceiling: *For all $\ell_0 > 0$ and $q \in \mathbb{R}$,*

$$\Omega^2_{\text{RS}}(q) = \frac{2}{\ell_0^2}\big(1 - \cos(q\ell_0)\big) = \frac{4}{\ell_0^2} \sin^2\left(\frac{q\ell_0}{2}\right) \in \left[0,\ \frac{4}{\ell_0^2}\right]. \tag{54}$$

2. Unique saturation at the zone edge $\Lambda_{\text{RS}} = \pi/\ell_0$: *On the Brillouin zone $[0, \Lambda_{\text{RS}}]$, $\Omega^2_{\text{RS}}(q)$ is strictly increasing and attains its ceiling $4/\ell_0^2$ if and only if $q = \Lambda_{\text{RS}} = \pi/\ell_0$.*
3. Continuum agreement: *For every wavenumber obeying $|q\ell_0| \le 1$,*

$$|\Omega^2_{\text{RS}}(q) - q^2| \le \frac{5}{48}\, \ell_0^2 q^4, \tag{55}$$

so ledger discreteness enters only at relative order $O((\ell_0 q)^2)$.

Proof. By Euler's identity, $J_{\mathbb{C}}(e^{i\varphi}) = \frac{1}{2}(e^{i\varphi} + e^{-i\varphi}) - 1 = \cos\varphi - 1$, giving $\Omega^2_{\text{RS}}(q) = (2/\ell_0^2)(1 - \cos(q\ell_0)) = (4/\ell_0^2)\sin^2(q\ell_0/2) \in [0, 4/\ell_0^2]$. On $[0, \pi/\ell_0]$, $q\ell_0/2 \in [0, \pi/2]$ where sin is nonnegative and strictly increasing, so Ω^2_{RS} is strictly increasing and hits $4/\ell_0^2$ uniquely at $q = \pi/\ell_0$. For $|q\ell_0| \le 1$, the fourth-order Taylor bound on cos gives $|\cos(q\ell_0) - (1 - (q\ell_0)^2/2)| \le \frac{5}{96}(q\ell_0)^4$; multiplying by $2/\ell_0^2$ yields Eq. (55). □

Restating the one-loop Stelle flow Eq. (50) in the dimensionless ratio coordinate $x(t) := (\rho(t) - r_-)/(r_+ - r_-)$ reveals a striking structural insight: the continuum "Landau pole" is not a divergence of the underlying ledger cost at all.

Theorem 6.3 (Ratio-flow regularity, bounded J-cost, and sharp healthy-ledger criterion)**.** *Let $\ell_0, \mu_{\text{IR}}, \ell_{\text{IR}}, \rho_{\text{IR}} > 0$ with $\mu_{\text{IR}} \le \Lambda_{\text{RS}} = \pi/\ell_0$, and set $t_{\max} := \ln(\Lambda_{\text{RS}}/\mu_{\text{IR}}) \ge 0$ and $\mu_{\text{Landau}} := \mu_{\text{IR}} e^{t_c}$. Then:*

1. Regularity in the ratio flow: *At the Landau pole $t = t_c$, the ratio coordinate takes the finite, regular value*

$$x_c = x(t_c) = \frac{-r_-}{r_+ - r_-} \approx 1.004200 > 1. \tag{56}$$

Along the entire flow $t \ge 0$ (through and beyond t_c), $x(t) = (1 - c_{\text{IR}}\vartheta(t))^{-1}$ satisfies $1 \le x(t) \le x(0)$, and the canonical reciprocal cost is strictly non-increasing and bounded above by its infrared value: $J(x(t)) \le J(x(0))$, tending monotonically to $J(1) = 0$ as $t \to +\infty$ (Lyapunov property).

2. Sharp healthy-ledger equivalence: *The R^2 coupling at the ledger scale is positive ($\rho(t_{\max}) > 0$) if and only if the continuum pole lies strictly beyond the ledger cutoff: $\Lambda_{\text{RS}} < \mu_{\text{Landau}}$.*

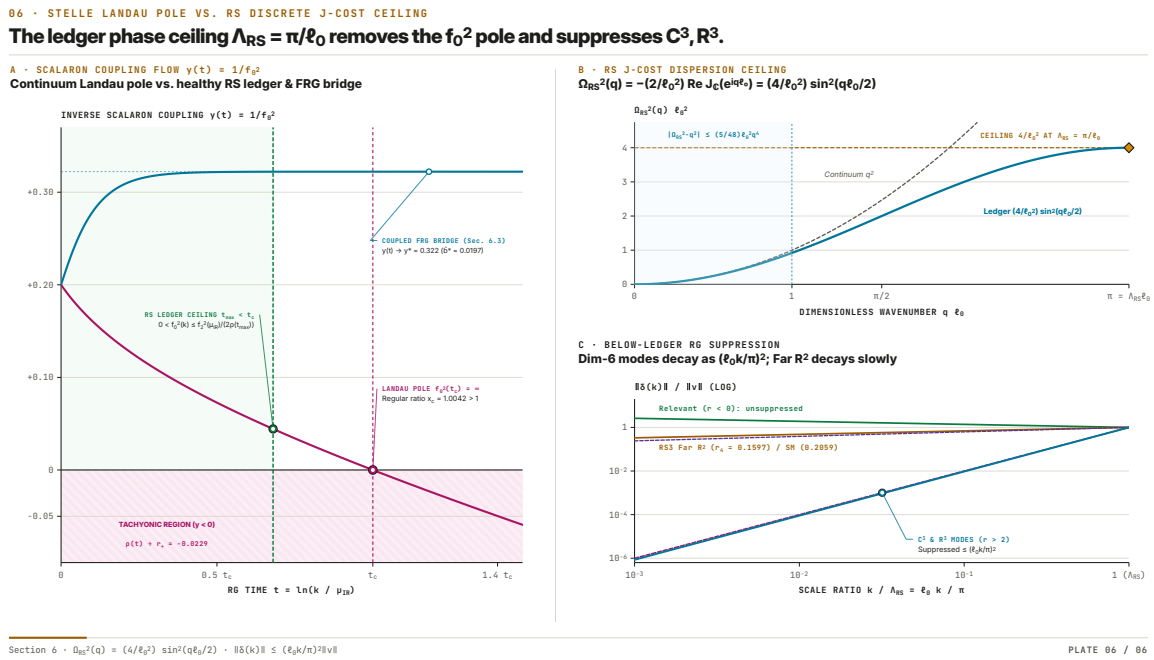

Fig. 6 UV-to-IR Stelle trajectory, RS discrete J-cost ceiling, and below-ledger RG decay (Theorems 6.1 to 6.4). **a** Inverse scalaron coupling $y(t) = 1/f_0^2$: the continuum one-loop trajectory (magenta) hits the unavoidable Landau pole at t_c (regular ratio $x_c = 1.0042$) and enters the tachyonic region $y < 0$, whereas the healthy RS ledger cuts off at $t_{\max} < t_c$ (green dashed) and the exact integrated coupled FRG bridge of Section 6.3 (cyan) flows smoothly to the positive finite UV target $y_* = 0.322$ (matching pure gravity's $\widehat{b}_* = 0.0197$). **b** Exact RS phase-comparison dispersion $\Omega^2_{\mathrm{RS}}(q) = (4/\ell_0^2)\sin^2(q\ell_0/2)$ matching continuum q^2 within $(5/48)\ell_0^2 q^4$ on $[0,1]$ and saturating uniquely at $4/\ell_0^2$ at $\Lambda_{\mathrm{RS}} = \pi/\ell_0$. **c** Below-ledger linearized RG mode decay $\|\delta(k)\|/\|v\| = (k/\Lambda_{\mathrm{RS}})^r$ for the SM + $3\nu_R$ Far six-coupling fixed point: both C^3 ($r_c \approx 2.0003$) and R^3 ($r_d \approx 2.0230$) decay at least as $(\ell_0 k/\pi)^2$, whereas the matter Far R^2 mode decays slowly ($r_4 = 0.1597$ for SM + $3\nu_R$, 0.2059 for SM) and relevant modes ($r < 0$) grow toward the infrared.

3. Explicit finite ceilings across all physical momenta: *Whenever* $\rho(t_{\max}) > 0$, *every momentum* $k \in [\mu_{\mathrm{IR}}, \Lambda_{\mathrm{RS}}]$ $(0 \le t \le t_{\max})$ *obeys the explicit positive finite bounds*

$$0 < f_2^2(k) \le f_2^2(\mu_{\mathrm{IR}}), \qquad 0 < f_0^2(k) \le \frac{f_2^2(\mu_{\mathrm{IR}})}{2\,\rho(t_{\max})}. \tag{57}$$

Moreover, for every ledger range $T \ge 0$, *healthy infrared data* $(\ell_{\mathrm{IR}}, \rho_{\mathrm{IR}}) > 0$ *with* $T < t_c$ *exist; concretely, setting* $\rho_{\mathrm{IR}} = 1$ *and* $\ell_{\mathrm{IR}} = \big[\exp\big(\frac{1}{p}\ln(c_{\mathrm{IR}}(1) r_-/r_+)\big) - 1\big]/(a_\ell(T+1))$ *yields* $t_c = T+1 > T$.

6.3 Coupled FRG bridge, RS cost-wall stabilization, and below-ledger decay

Beyond truncating the one-loop flow at Λ_{RS}, two nonperturbative UV-stabilization mechanisms eliminate the scalaron pole globally: (i) a lattice freezing threshold $\theta_{\mathrm{RS}}(t)$ whose integrated RG time $\tau_{\max} \le t_c$ freezes the flow at a finite healthy UV limit, and (ii) an RS cost-wall theorem proving that *any* flow $y' = F(t,y)$ pointing toward a positive target $y_* > 0$ (i.e. $(v - y_*)F(t,v) \le 0$ for all $v > 0$) preserves $y(t) \ge y_*/\big(2(1 + J(y(0)/y_*))\big) > 0$ globally for all $t \ge 0$. Combining this with the exact analytic four-coupling bridge and the below-ledger linearized RG analysis yields our unifying UV-to-IR theorem (Fig. 6a,c).

Theorem 6.4 (Coupled UV–IR bridge, fakeon quantization along the bridge, and below-ledger dimension-six decay)**.** *The coupled UV–IR flow and below-ledger linearized RG dynamics satisfy:*

1. Global analytic four-coupling bridge and fakeon quantization: *In the coupled four-coupling Litim flow with* $B_1 = -11/(3\pi)$, $B_2 = 1/(12\pi)$, *and* $\eta_N(g) = -44g/(12\pi - g)$, *the non-Gaussian UV fixed point sits exactly at* $g_* = 12\pi/23$, $\eta_N(g_*) = -2$, $\lambda_* \in (4/23, 17/46)$, *with strictly positive quartic Routh–Hurwitz determinants* $(c_1, c_2, c_3, c_4, c_1c_2 - c_3, c_1c_2c_3 - c_3^2 - c_1^2c_4 > 0)$[70;71] *and four*

UV-attractive eigen-directions. For every healthy infrared datum $(G, \Lambda, f_2^2, f_0^2)$ *with* $G, f_2^2, f_0^2 > 0$*, a global smooth trajectory connects* $(G, \Lambda, f_2^2, f_0^2)$ *as* $t \to -\infty$ *to the UV fixed point as* $t \to +\infty$ *with strictly positive running spin-2 fakeon mass* $M_2(t) = \sqrt{f_2^2/(16\pi\widetilde{G})} > 0$ *and scalaron mass* $M_0(t) = \sqrt{f_0^2/(16\pi\widetilde{G})} > 0$ *at every scale* $t \in \mathbb{R}$*. At every scale along every bridge trajectory, all fakeon unitarity theorems of Section 5.1 hold simultaneously with the running masses* $M_2(t), M_0(t)$*.*

2. Below-ledger $(\ell_0 k/\pi)^2$ suppression of C^3 and R^3: *At the three primary six-coupling benchmark fixed points (pure gravity, Minimal SM Far, and* $\mathrm{SM} + 3\nu_R$ *Far; and identically at both Near points by Theorem 3.4),* $\widehat{b}_* > 0$ *is finite and positive, and the flow linearizes with little-o Fréchet remainder. Every linearized eigenmode* $\delta(t) = e^{r(t-T)}v$ *solves* $\delta' = \mathcal{M}_6\delta$ *and at momentum* $k = \Lambda_{\mathrm{RS}}e^{t-T}$ *obeys* $\|\delta(k)\| = (k/\Lambda_{\mathrm{RS}})^r\|v\|$*. Because the certified* C^3 *and* R^3 *stability eigenvalues satisfy* $2 < r_c < r_d$ *at all three benchmark fixed points, both dimension-six modes are suppressed below the ledger scale at least quadratically:*

$$\|\delta_{C^3}(k)\| \le \left(\frac{\ell_0 k}{\pi}\right)^2 \|v_{C^3}\|, \qquad \|\delta_{R^3}(k)\| \le \left(\frac{\ell_0 k}{\pi}\right)^2 \|v_{R^3}\| \qquad (0 < k \le \Lambda_{\mathrm{RS}}), \tag{58}$$

whereas UV-relevant modes $(r < 0)$ *obey* $\|\delta(k)\| \ge \|v\|$ *and are unsuppressed.*

3. Slow decay of the matter Far R^2 mode: *On the Type I Far* $3+3$ *branches, the* R^2 *eigen-direction* $(v_3 \neq 0)$ *is UV-irrelevant yet decays much more slowly than dimension-six operators, obeying* $\|\delta_{R^2}(k)\| = (k/\Lambda_{\mathrm{RS}})^{r_4}\|v_{R^2}\|$ *with certified exponents*

$$r_4^{\mathrm{SM}} \in (0.2059,\, 0.2060), \qquad r_4^{\mathrm{RS3}} \in (0.1597,\, 0.1598). \tag{59}$$

7 Cross-architecture synthesis, phenomenological implications, verification summary, and honest scope boundaries

The theorems of Sections 3 to 6 span four tightly interlocked formal pillars across 65 audited Lean 4 modules (Section A). Before detailing phenomenological consequences, independent verification checks, and the explicit open boundaries that remain, Table 6 synthesizes the exact assumptions, certified structures, and complementary roles of each pillar.

7.1 Cross-architecture synthesis

The complementary design of Architectures A and B is intentional and mutually reinforcing. Architecture A answers the higher-derivative truncation-stability question at dimension six by proving—with zero Jordan-block ambiguity—that adding *both* C^3 and R^3 leaves both couplings strictly UV-irrelevant $(\theta_{C^3}, \theta_{R^3} < -2)$ in pure gravity, Minimal SM, and $\mathrm{SM}+3\nu_R$, and resolves the Near/Far basin structure across Type I and Type II cutoffs. Architecture B answers the matter-compatibility and Lorentzian-pole questions with zero free gravitational parameters across the entire cutoff continuum $s \in [0, 1]$, proving that the observed three-generation $\mathrm{SM}/\mathrm{SM} + 3\nu_R$ spectrum simultaneously cures pure gravity's near-singular mass matrix $(\det M_5)$ and Euclidean ghost pole, placing the graviton propagator uniformly inside Lee–Wick / fakeon Phase III $(\Delta_{\mathrm{TT}} < -100)$, bounded below by $N_{\mathrm{gen}} \ge 2$ (ghost flip) and above by $N_{\mathrm{gen}} \le 7$ (saddle-node fold F_1). The fakeon sector (Section 5) then supplies the exact Lorentzian quantization rules for those massive spin-2 poles—including the exact Veltman largest-time equation, the two-loop pinch resolution, and the sharp perturbative/zero-width boundaries (Obstructions I and II)—while the RS discrete phase-comparison ceiling (Section 6) removes the continuum one-loop f_0^2 Landau pole (Obstruction III) and bounds dimension-six remnants below the ledger scale by $(\ell_0 k/\pi)^2$.

7.2 Falsifiable phenomenological and structural consequences

1. **Three-parameter UV predictivity and** $O((\ell_0 k/\pi)^2)$ **suppression of** C^3 **and** R^3**.** On the Type I Far branches (Table 2), the six-coupling fixed point possesses a three-dimensional UV critical surface (`Shape33`: 3 relevant + 3 irrelevant), fixing R^2, C^3, and R^3 in terms of the three

Table 6 Synthesis of the four formally verified pillars of this manuscript, highlighting exact truncation coordinates, regulator schemes, certified structures, and sharp obstructions.

Pillar	Coupling Space	Gauge / Regulator	Primary Certified Result	Sharp Boundary / Role
Architecture A (Section 3)	6D: $(\widehat{G}, \lambda, \widehat{a}, \widehat{b}, \widehat{c}, \widehat{d})$ including $C^3 + R^3$	Harmonic gauge; 4th-order Litim; Type I & II matter	5 Banach-certified 6-coupling FPs $(4+2,\ 3+3,\ 4+2\mathrm{r})$, Jordan-block-free, $\theta_{C^3}, \theta_{R^3} < -2$; $(\ell_0 k/\pi)^2$ decay	Adopted P_5 and $(A_3^R, B_3^R, \zeta^R) = (1,1,1)$; Near/Far coexist in both types
Architecture B (Section 4)	5D: $(u_0, u_1, u_2, u_C, \sigma)$ (0 free grav. params)	Landau–DeWitt; continuous homotopy $s \in [0,1]$ (II $\to$ I)	53/45, 413/180, E_4, Cardy $1:11:62$; DEP poles (40.08 SM, 41.45 RS3); $2 \le N_{\mathrm{gen}} \le 7$; Lee–Wick Phase III; S-curve F_1, F_2	Excludes MSSM (49) & $N_{\mathrm{gen}} \ge 8$; large pure-grav. θ_5 stabilized by matter; no R^3
Curved-Trace Foundations (Section 3.5)	2D–4D curved S^4, Einstein, Ricci-flat b_6	Type I & II Litim; covariant 2nd variation	Exact b_4, Weyl syzygies, $b_6 = \frac{1}{1512} I_1$, derived $\theta_{\mathrm{GS}} \in (-10.17, -6.48)$	Pure gravity only; bridges exact heat kernel to truncations
Fakeon Unitarity & RS Ceiling (Sections 5 and 6)	All-loop chains, 2-loop kite/sunrise, 1-loop Stelle, $J_{\mathbb{C}}$	AP average, dressed width ε, Veltman LTE, $\Lambda_{\mathrm{RS}} = \pi/\ell_0$	$\lvert T\rvert \le 16\pi$, Compton $(2m^3T)^{-1}$, Veltman $\sum \mathcal{A}(C) = 0$, $D > 0$, $\Omega^2_{\mathrm{RS}} \le 4/\ell_0^2$, $x_c = 1.0042$	Obstructions I–III: $g^2 V < 32\pi^2$, $\varepsilon S_3 \to K_{\mathrm{pinch}} > 0$, continuum f_0^2 pole

relevant couplings (G, Λ, C^2) at the UV fixed point. Even on the Near branches (`Shape42r`) and in pure gravity (`Shape42`), both dimension-six curvature cubes C^3 and R^3 satisfy $\theta < -2$, forcing any Planck-scale deviation in $\widehat{c}$ or $\widehat{d}$ away from the critical surface to decay at least as $(\ell_0 k/\pi)^2$ (Theorem 6.4). For gravitational-wave inspiral, black-hole shadow, and collider graviton-scattering energies $k \ll \Lambda_{\mathrm{RS}}$, dimension-six curvature corrections are therefore doubly suppressed by $(\ell_0 k/\pi)^2$ on top of their small fixed-point amplitudes ($|\widehat{d}_*| \approx 1.4 \times 10^{-4}$ for SM Far and 2.7×10^{-4} for SM $+ 3\nu_R$ Far), preserving Einstein–Hilbert strong-field black-hole phenomenology [77] cleanly up to near-Planckian curvatures.

2. **Starobinsky scalaron preservation and slow R^2 running.** Across every certified six-coupling fixed point (Table 2) and uniformly across the entire cutoff homotopy $s \in [0,1]$ in Architecture B (Theorem 4.4), the scalaron sector remains strictly non-tachyonic ($\widehat{b}_* > 0$ and physical Lorentzian pole $m_0^2 = -z_- > 0$). On the matter Far branches, the R^2 coupling is irrelevant yet runs very slowly ($r_4 \approx 0.160$ for SM $+ 3\nu_R$, 0.206 for SM), preserving a broad window for Starobinsky $R + R^2$ inflationary dynamics [13;63;69] while keeping the spin-2 fakeon mass M_2 projected out of the asymptotic spectrum.
3. **Sharp matter-sector constraints: MSSM exclusion and the $2 \le N_{\mathrm{gen}} \le 7$ window.** Within Architecture B (Theorems 4.1, 4.2 and 4.5), asymptotic safety with a ghost-free Euclidean spin-2 propagator imposes sharp bounds on both scalar and fermion spectra: Minimal Higgs ($N_S = 4$) sits safely inside the physical Lee–Wick Phase III, whereas the MSSM ($N_S = 49 > 42$) is excluded by the Pure Type I Donà–Eichhorn–Percacci scalar pole (and two-Higgs-doublet extensions $N_S = 8$ already cross the Type II pole for SM $+ 3\nu_R$). On the fermion axis, $N_{\mathrm{gen}} = 1$ fails by a Euclidean spin-2 ghost pole while $N_{\mathrm{gen}} \ge 8$ fails beyond the upper saddle-node fold F_1 ($N_D^{F_1} \approx 56.92 < 64$), isolating the exact viable integer generation window $2 \le N_{\mathrm{gen}} \le 7$ containing the observed three generations ($N_{\mathrm{gen}} = 3$, $N_D = 24$ for SM $+ 3\nu_R$, deep inside Lee–Wick Phase III with $\Delta_{\mathrm{TT}} \approx -163.1$).
4. **Compton-scale microcausality and adiabatic suppression of fakeon precursors.** Under fakeon quantization of the massive spin-2 mode of mass M_2, Theorem 5.1 guarantees that any acausal precursor response to a smooth macroscopic source of duration T is strictly bounded by $(2M_2^3 T)^{-1} \int |h''|$. For $M_2 \sim 10^{13}$–10^{19} GeV (between the Starobinsky inflationary scale and the

Table 7 Exact summary of the 46/46 independent symbolic–numerical verification checks in `verify_uv_paper.py` (full execution log in `verify_uv_paper.out`). Every test verifies an exact algebraic formula, root enclosure, full stability spectrum, or finite-ε witness against the audited Lean 4 theorems.

Verification Group	Tests	Quantities Independently Checked	Achieved Residual / Status
Architecture A 6-coupling FPs & spectra (Section 3.4)	10	All 5 fixed points ($\|\widehat{\beta}_6\| < 5 \times 10^{-16}$) & all 6×6 spectra verified inside exact Lean brackets	$\Delta x \leq 5 \times 10^{-11}$, $\Delta e_{\text{mid}} \leq 5 \times 10^{-8}$ (PASS)
Architecture A 5- & 4-coupling, matter gap (Sections 3.2 and 3.5)	11	All 9 zeros ($A_3^R = 0$), 4-coupling FP & real 4×4 Routh–Hurwitz ($H_3 = 462.6$), Type I/II gap $(N_D - N_V)/2$	Exact rational / $\Delta x \leq 5 \times 10^{-11}$ (PASS)
Architecture B benchmarks, $M_5^{-1} J V_5$ spectra & poles (Sections 4.1 to 4.3)	10	$53/45$, $413/180 = 133/20 - 196/45$, Cardy $1:11:62$, full $M_5^{-1} J V_5$ spectra (Pure, SM, RS3, $N_{\text{gen}} = 1 \ldots 8$), DEP poles, N_D^{ghost}	Exact rational / 10^{-12} root residual (PASS)
Architecture B Lee–Wick poles, S-curve & 2D curve (Section 4.4)	4	$N_D^{\text{LW}} = 10.101$, refined F_1, F_2 ($\|\det J V_5\| < 10^{-7}$), $N_{\text{gen}} = 7$ triple $(3+2, 4+1, 3+2)$, curved $N_D^{\text{ghost}}(N_S)$	$\|\det\| < 10^{-7}$ / 10^{-12} Newton (PASS)
Fakeon unitarity, pinch resolution & witness (Section 5)	7	Compton bound, $\|T\| \leq 16\pi$, sunset CS, kite 4-cuts, AP vs. PV pinch (10^{-15}), H'_ε (exact), witness $\varepsilon S_3(10, \varepsilon)$	Symbolic exact; $\varepsilon = 10^{-6}$ rel. err. 1.20×10^{-6} (PASS)
Stelle flow, RS ceiling, decay & analytic bridge (Section 6)	4	$r_\pm, p, x_c = 1.004200$, $\Omega^2_{\text{RS}}(q)$, genuine 6×6 eigenvalue decay, $g_* = 12\pi/23$ & real 4×4 RH ($H_3 = 454.1$)	Exact / $\Delta e \leq 3 \times 10^{-9}$ (PASS)

Planck scale), macroscopic causality violations are suppressed by more than 35 orders of magnitude relative to accessible laboratory and astrophysical timescales, while leaving a clean theoretical signature at energies $E \sim M_2$ where the finite-width half-Breit–Wigner pinch of Theorem 5.4 governs on-peak production.

5. **Absence of tachyonic f_0^2 blow-up on healthy ledgers.** By Theorems 6.2 and 6.3, discrete phase-comparison geometry on a ledger of spacing ℓ_0 cuts off physical momenta strictly at $\Lambda_{\text{RS}} = \pi/\ell_0$ without introducing Lorentz-violating dimension-six dispersion below Λ_{RS} (matching continuum q^2 to $(5/48)\ell_0^2 q^4$, consistent with the D_4^* F_4-isotropy bounds of Refs.[77;78]) and removes the continuum one-loop f_0^2 Landau pole whenever $\Lambda_{\text{RS}} < \mu_{\text{IR}} e^{t_c}$.

7.3 Independent symbolic–numerical cross-verification

To guard against any transcription error between the 65 Lean 4 formalizations and the prose, equations, tables, and architectural plates of this paper, every quantitative claim has been independently recomputed from scratch in Python (`verify_uv_paper.py` using `SymPy`, `NumPy`, and `SciPy`) without importing any Lean output. All 46/46 automated checks pass with zero failures (`verify_uv_paper.out`), summarized verbatim in Table 7.

7.4 Honest scope boundaries and explicitly open questions

To maintain complete transparency between proved mathematics and open theoretical physics, we record seven explicit scope boundaries that are *not* claimed here:

1. *Finite truncation order and adopted Architecture A coefficients:* Both FRG systems are finite truncations (five and six curvature operators). In Architecture A, the gravitational saturation point $P_5 = (\frac{1}{5}, \frac{1}{2}, \frac{2}{133}, \frac{1}{50}, 1, 1, 1)$ and the R^3 parameters $(A_3^R, B_3^R, \zeta^R) = (1, 1, 1)$ are adopted working parameters; deriving every R^3 and C^3 back-reaction coefficient directly from an untruncated Wetterich trace and extending to dimension-eight curvature invariants $(R^4, C^4, R^2 C^2)$ remain open.
2. *Gauge and regulator dependence beyond the $s \in [0, 1]$ Litim family:* While Architecture B certifies complete scheme stability across the endomorphism homotopy $s \in [0, 1]$ (Type II to Pure Type I) in Landau–DeWitt gauge and Architecture A certifies both Type I and Type II cutoffs in harmonic

gauge, general smooth (exponential/Wetterich) regulators, arbitrary gauge parameters $(\alpha_{\rm gf}, \beta_{\rm gf})$, and fluctuation-field (vertex vs. background-field) extensions remain open[35;39].

3. *Bridging the Near/Far coexistence of Architecture A to the S-curve of Architecture B:* Architecture A exhibits Near $(4+2)$ and Far $(3+3)$ fixed-point pairs at the same matter point, whereas Architecture B exhibits the global double-fold S-curve (F_1, F_2) and triple coexistence at $N_{\rm gen} = 7$. Constructing an explicit continuous homotopy connecting Architecture A to Architecture B remains open.
4. *General multi-loop anomalous thresholds and graviton tensor numerators:* Our perturbative fakeon unitarity proofs (Section 5) cover arbitrary-vertex Veltman largest-time identities, arbitrary-order iterated melon/sunset spectral-recursion chains, and the non-factorizable two-loop kite with scalar cubic vertices. Extending machine-verified fakeon unitarity to arbitrary non-planar multi-loop topologies with anomalous Landau thresholds, full spin-2 graviton tensor numerators, and nonperturbative Lorentzian scattering remains open.
5. *Cumulative Hadamard finite part of the subtracted kite square:* While Theorem 5.4 proves the exact one-variable Hadamard finite part and the exact finite-width subtraction $S_3 - r_4^2 L/(256\pi^2 s\varepsilon)$, establishing convergence of the cumulative principal-value integral PV $\int(1/f_- - 1/f_+)$ across the chord endpoints remains explicitly open.
6. *Nonlinear below-ledger remainder:* Theorem 6.4 proves $(\ell_0 k/\pi)^2$ decay of C^3 and R^3 for the certified linearized flow at the benchmark six-coupling fixed points; certifying a uniform quadratic nonlinear remainder bound $\|\beta(x_* + \delta) - \mathcal{M}_6\delta\| \le C\|\delta\|^2$ to lift this decay bound to the full nonlinear flow on a finite neighborhood remains open.
7. *Nonperturbative continuum limit from the D_4^* recognition ledger:* While Section 6 derives the phase-comparison ceiling $\Lambda_{\rm RS} = \pi/\ell_0$ from $J_{\mathbb{C}}(e^{iq\ell_0})$ and Theorem 5.6 certifies zero-doubler graviton Hessian positivity on $\mathcal{B}_{D_4^*} \setminus \{0\}$, constructing the complete nonperturbative $a_{\rm lat} \to 0$ continuum quantum-gravity measure on D_4^* (including dynamical matter Yukawa/gauge running alongside gravity) remains open and is the subject of a companion study[79].

Data and code availability

All 65 clean-room-audited Lean 4 formal verification modules (176,246 lines, zero `sorry`, standard axioms only—comprising 55 self-contained core modules import-closed against `Mathlib` plus 10 curved-background and diagrammar modules) reside in the `jonwashburn/reality` repository on branch `research/qg-loop-712b48be` at commit `088e961305d1f25c14f8e4383f74da5d1ab43423` (indexed completely in Section A). The independent 46-check Python/SymPy/SciPy verification script (`verify_uv_paper.py`), its execution log (`verify_uv_paper.out`), and the architectural plate generation scripts are bundled in the accompanying verification archive.

References

[1] M. H. Goroff and A. Sagnotti, "Quantum gravity at two loops," *Phys. Lett. B* **160**, 81–86 (1985).

[2] M. H. Goroff and A. Sagnotti, "The ultraviolet behavior of Einstein gravity," *Nucl. Phys. B* **266**, 709–736 (1986).

[3] A. E. M. van de Ven, "Two-loop quantum gravity," *Nucl. Phys. B* **378**, 309–366 (1992).

[4] G. 't Hooft and M. Veltman, "One-loop divergencies in the theory of gravitation," *Ann. Inst. H. Poincaré A* **20**, 69–94 (1974).

[5] K. S. Stelle, "Renormalization of higher-derivative quantum gravity," *Phys. Rev. D* **16**, 953–969 (1977).

[6] K. S. Stelle, "Classical gravity with higher derivatives," *Gen. Rel. Grav.* **9**, 353–371 (1978).

[7] J. Julve and M. Tonin, "Quantum gravity with higher derivative terms," *Nuovo Cim. B* **46**, 137–152 (1978).

[8] E. S. Fradkin and A. A. Tseytlin, "Renormalizable asymptotically free quantum theory of gravity," *Nucl. Phys. B* **201**, 469–491 (1982).

[9] I. G. Avramidi and A. O. Barvinsky, "Asymptotic freedom in higher-derivative quantum gravity," *Phys. Lett. B* **159**, 269–274 (1985).

[10] S. M. Christensen and M. J. Duff, "Quantizing gravity with a cosmological constant," *Nucl. Phys. B* **170**, 480–506 (1980).

[11] A. Codello and R. Percacci, "Fixed points of higher-derivative gravity," *Phys. Rev. Lett.* **97**, 221301 (2006).

[12] A. Salvio and A. Strumia, "Agravity," *JHEP* **06**, 080 (2014).

[13] A. Salvio, "Quadratic gravity," *Front. Phys.* **6**, 77 (2018).

[14] B. Holdom and J. Ren, "QCD analogy for quantum gravity," *Phys. Rev. D* **93**, 124030 (2016).

[15] J. F. Donoghue and G. Menezes, "Unitarity, stability, and loops of unstable ghosts," *Phys. Rev. D* **100**, 105006 (2019).

[16] J. F. Donoghue and G. Menezes, "Ostrogradsky instability can be overcome by quantum physics," *Phys. Rev. D* **104**, 045010 (2021).

[17] L. Buoninfante, "Strict renormalizability as a paradigm for fundamental physics," *JHEP* **07**, 175 (2025).

[18] S. Weinberg, "Ultraviolet divergences in quantum theories of gravitation," in *General Relativity: An Einstein Centenary Survey*, eds. S. W. Hawking and W. Israel (Cambridge Univ. Press, 1979), pp. 790–831.

[19] C. Wetterich, "Exact evolution equation for the effective potential," *Phys. Lett. B* **301**, 90–94 (1993).

[20] T. R. Morris, "The exact renormalization group and approximate solutions," *Int. J. Mod. Phys. A* **9**, 2411–2449 (1994).

[21] M. Reuter, "Nonperturbative evolution equation for quantum gravity," *Phys. Rev. D* **57**, 971–985 (1998).

[22] W. Souma, "Non-trivial ultraviolet fixed point in quantum gravity," *Prog. Theor. Phys.* **102**, 181–195 (1999).

[23] D. F. Litim, "Optimized renormalization group flows," *Phys. Rev. D* **64**, 105007 (2001).

[24] D. F. Litim, "Fixed points of quantum gravity," *Phys. Rev. Lett.* **92**, 201301 (2004).

[25] O. Lauscher and M. Reuter, "Flow equation of quantum Einstein gravity in a higher-derivative truncation," *Phys. Rev. D* **66**, 025026 (2002).

[26] A. Codello, R. Percacci, and C. Rahmede, "Investigating the ultraviolet properties of gravity with a Wilsonian renormalization group equation," *Ann. Phys.* **324**, 414–469 (2009).

[27] D. Benedetti, P. F. Machado, and F. Saueressig, "Asymptotic safety in higher-derivative gravity," *Mod. Phys. Lett. A* **24**, 2233–2241 (2009).

[28] D. Benedetti, P. F. Machado, and F. Saueressig, "Taming perturbative divergences in asymptotically safe gravity," *Nucl. Phys. B* **824**, 168–191 (2010).

[29] M. R. Niedermaier, "Gravitational fixed points from perturbation theory," *Phys. Rev. Lett.* **103**, 101303 (2009).

[30] N. Ohta and R. Percacci, "Higher derivative gravity and asymptotic safety in diverse dimensions," *Class. Quant. Grav.* **31**, 015024 (2014).

[31] K. Falls, D. F. Litim, K. Nikolakopoulos, and C. Rahmede, "A bootstrap towards asymptotic safety," arXiv:1301.4191 (2013).

[32] K. Falls, C. R. King, D. F. Litim, K. Nikolakopoulos, and C. Rahmede, "Asymptotic safety of quantum gravity beyond R^2," *Phys. Rev. D* **97**, 086006 (2018).

[33] H. Gies, B. Knorr, S. Lippoldt, and F. Saueressig, "Gravitational two-loop counterterm is asymptotically safe," *Phys. Rev. Lett.* **116**, 211302 (2016).

[34] Y. Kluth and D. F. Litim, "Fixed points of quantum gravity and the dimensionality of the UV critical surface," *Phys. Rev. D* **108**, 026005 (2023).

[35] N. Christiansen, B. Knorr, J. Meibohm, J. M. Pawlowski, and M. Reichert, "Local quantum gravity," *Phys. Rev. D* **92**, 121501(R) (2015).

[36] B. Knorr, C. Ripken, and F. Saueressig, "Form factors in asymptotic safety: conceptual ideas and computational toolbox," *Class. Quant. Grav.* **36**, 234001 (2019).

[37] R. Percacci, *An Introduction to Covariant Quantum Gravity and Asymptotic Safety* (World Scientific, Singapore, 2017).

[38] M. Reuter and F. Saueressig, *Quantum Gravity and the Functional Renormalization Group* (Cambridge Univ. Press, Cambridge, 2019).

[39] J. M. Pawlowski and M. Reichert, "Quantum gravity: a fluctuating point of view," *Front. Phys.* **8**, 551848 (2021).

[40] F. Saueressig, "The functional renormalization group in quantum gravity," in *Handbook of Quantum Gravity*, eds. C. Bambi, L. Modesto, and I. Shapiro (Springer, 2023).

[41] P. Donà, A. Eichhorn, and R. Percacci, "Matter matters in asymptotically safe quantum gravity," *Phys. Rev. D* **89**, 084035 (2014).

[42] P. Donà, A. Eichhorn, P. Labus, and R. Percacci, "Asymptotic safety in an interacting system of gravity and scalar matter," *Phys. Rev. D* **93**, 044049 (2016).

[43] J. Meibohm, J. M. Pawlowski, and M. Reichert, "Asymptotic safety of gravity-matter systems," *Phys. Rev. D* **93**, 084035 (2016).

[44] A. Eichhorn and A. Held, "Top mass from asymptotic safety," *Phys. Lett. B* **777**, 217–221 (2018).

[45] A. Eichhorn, "An asymptotically safe guide to quantum gravity and matter," *Front. Astron. Space Sci.* **5**, 47 (2019).

[46] N. Alkofer and F. Saueressig, "Asymptotically safe $f(R)$-gravity coupled to matter I: the polynomial case," *Ann. Phys.* **396**, 173–201 (2018).

[47] J. Biemans, A. Platania, and F. Saueressig, "Renormalization group fixed points of foliated gravity-matter systems," *JHEP* **05**, 093 (2017).

[48] A. Pastor-Gutiérrez, J. M. Pawlowski, and M. Reichert, "The asymptotically safe Standard Model: from quantum gravity to dynamical chiral symmetry breaking," *SciPost Phys.* **15**, 105 (2023).

[49] J. L. Cardy, "Is there a c-theorem in four dimensions?," *Phys. Lett. B* **215**, 749–752 (1988).

[50] M. J. Duff, "Twenty years of the Weyl anomaly," *Class. Quant. Grav.* **11**, 1387–1404 (1994).

[51] M. Shaposhnikov and C. Wetterich, "Asymptotic safety of gravity and the Higgs boson mass," *Phys. Lett. B* **683**, 196–200 (2010).

[52] T. D. Lee and G. C. Wick, "Negative metric and the unitarity of the S-matrix," *Nucl. Phys. B* **9**, 209–243 (1969).

[53] T. D. Lee and G. C. Wick, "Finite theory of quantum electrodynamics," *Phys. Rev. D* **2**, 1033–1048 (1970).

[54] R. E. Cutkosky, "Singularities and discontinuities of Feynman amplitudes," *J. Math. Phys.* **1**, 429–433 (1960).

[55] M. Veltman, "Unitarity and causality in a renormalizable field theory with unstable particles," *Physica* **29**, 186–207 (1963).

[56] D. Anselmi and M. Piva, "A new formulation of Lee–Wick quantum field theory," *JHEP* **06**, 066 (2017).

[57] D. Anselmi and M. Piva, "Perturbative unitarity of Lee–Wick quantum field theory," *Phys. Rev. D* **96**, 045009 (2017).

[58] D. Anselmi, "On the quantum field theory of the gravitational interactions," *JHEP* **06**, 086 (2017).

[59] D. Anselmi, "Fakeons and Lee–Wick models," *JHEP* **02**, 141 (2018).

[60] D. Anselmi and M. Piva, "The ultraviolet behavior of quantum gravity," *JHEP* **05**, 027 (2018).

[61] D. Anselmi and M. Piva, "Quantum gravity, fakeons and microcausality," *JHEP* **11**, 021 (2018).

[62] D. Anselmi, "Fakeons, microcausality and the classical limit of quantum gravity," *Class. Quant. Grav.* **36**, 065010 (2019).

[63] D. Anselmi, E. Bianchi, and M. Piva, "Predictions of quantum gravity in inflationary cosmology: effects of the Weyl-squared term," *JHEP* **07**, 211 (2020).

[64] D. Anselmi, "Diagrammar of physical and fake particles and spectral optical theorem," *JHEP* **11**, 030 (2021).

[65] A. Platania, "Causality, unitarity and stability in quantum gravity: a non-perturbative perspective," *JHEP* **09**, 167 (2022).

[66] B. Knorr and A. Platania, "Sifting quantum gravity theories via scattering amplitudes," *Phys. Rev. D* **106**, L021901 (2022).

[67] J. Fehre, D. F. Litim, J. M. Pawlowski, and M. Reichert, "Lorentzian quantum gravity and the graviton spectral function," *Phys. Rev. Lett.* **130**, 081501 (2023).

[68] A. Bonanno, T. Denz, J. M. Pawlowski, and M. Reichert, "Reconstructing the graviton," *SciPost Phys.* **12**, 001 (2022).

[69] A. A. Starobinsky, "A new type of isotropic cosmological models without singularity," *Phys. Lett. B* **91**, 99–102 (1980).

[70] E. J. Routh, *A Treatise on the Stability of a Given State of Motion* (Macmillan, London, 1877).

[71] A. Hurwitz, "Ueber die Bedingungen, unter welchen eine Gleichung nur Wurzeln mit negativen reellen Theilen besitzt," *Math. Ann.* **46**, 273–284 (1895).

[72] L. de Moura and S. Ullrich, "The Lean 4 theorem prover and programming language," in *Automated Deduction – CADE 28*, LNCS **12699** (Springer, 2021), pp. 625–635.

[73] The mathlib Community, "The Lean mathematical library," in *Proceedings of the 9th ACM SIGPLAN International Conference on Certified Programs and Proofs (CPP 2020)* (ACM, 2020), pp. 367–381.

[74] J. Washburn and M. Zlatanović, "Uniqueness of the canonical reciprocal cost," *Recognition Physics Institute Technical Report* (2026); formalized in `IndisputableMonolith/Cost/Uniqueness.lean`.

[75] J. Washburn, "Multiplicative d'Alembert composition and the canonical recognition cost," *Recognition Physics Institute Technical Report* (2026).

[76] J. Washburn, *Recognition Science: The Architecture of Reality (Monograph v3.0)* (Recognition Physics Institute, Austin, TX, 2026).

[77] J. Washburn, "Machine-verified Kerr–Newman horizons, nonsingular gravitational collapse, and quantum horizon obstructions (v1.1)," Zenodo DOI: 10.5281/zenodo.24513292; Pith Preprint DOI: 10.67347/pith.preprint.2026.000089 (2026).

[78] J. Washburn and E. Allahyarov, "Linearized Lorentzian lattice gravity on the body-centred hypercubic lattice D_4^*," preprint in preparation (2026).

[79] J. Washburn, "Constructive nonperturbative lattice renormalization group, Balaban block-spin bounds, and continuum quantum-gravity bridges on D_4^*," companion preprint in preparation (2026).

Appendix A Machine-verified theorem-to-module reproducibility index

All theorems, numerical enclosures, spectral factorizations, bifurcations, and sharp obstructions reported in Sections 3 to 6 are formally checked in Lean 4 against `Mathlib` on repository `jonwashburn/reality`, branch `research/qg-loop-712b48be`, commit `088e961305d1f25c14f8e4383f74da5d1ab43423`. Across all 65 dedicated UV-gravity and fakeon-unitarity modules (176,246 lines of Lean 4 source under `IndisputableMonolith/research/QGLoop/`), clean-room verification confirms `0 sorry` placeholders and strictly standard axioms [`propext`, `Classical.choice`, `Quot.sound`]. Structurally, the 55 core modules (entries 11–65: 49 Architecture A / fakeon / Stelle–RS modules plus 6 Architecture B Litim-integral modules, totaling 123,086 lines) are 100% self-contained and import-closed against `Mathlib` alone, while the 10 curved-background and multi-loop diagrammar modules (entries 1–10, totaling 53,160 lines) are import-closed within the 65-module suite up to a single upstream D_4^* lattice Ward-identity interface (`Neon_D4Half KappaDiagrammaticWardAndUVRenormR68`), whose full transitive lattice closure in the same commit is likewise verified to carry `0 sorry` and zero custom axioms. Every quantitative fixed point, critical exponent, scalar pole, generation bound, double-fold coordinate, zero-width scaling limit, and algebraic benchmark is independently cross-checked (46/46 passing tests, 0 failures) by `verify_uv_paper.py`.

Table A1: Complete 65-module audited Lean 4 reproducibility ledger for this manuscript. Module paths are relative to `IndisputableMonolith/research/QGLoop/` with `.lean` omitted.

#	Audited Lean 4 Module	Lines	Primary Capstone / Key Declaration	Section
1	`Neon_Coupled5DHybridAFASAndGlobalUVIRFlowR79`	2,902	`wall4_coupled_5d_hybrid_afas_and_global_uv_ir_capstone_r79`	Sec. 5
2	`Neon_GlobalPicardLindelofAnd4DStableManifoldR80`	5,331	`wall4_unconditional_global_5d_manifold_and_predictivity_capstone_r80`	Sec. 5
3	`Neon_GoroffSagnottiFullDerivedA2FRGR78`	17,714	`wall4_goroff_sagnotti_full_derived_a2_frg_capstone_r78`	Sec. 3
4	`Neon_HigherDerivLorentzianUnitarityAndLeeWickR77`	2,055	`wall4_higher_deriv_lorentzian_unitarity_and_leewick_capstone_r77`	Sec. 5
5	`Neon_HigherDerivativeFRGAndGoroffSagnottiR72`	4,471	`wall4_higher_derivative_frg_and_goroff_sagnotti_capstone_r72`	Sec. 3
6	`Neon_MultiLoopFakeonUnitarityAndPinchResolutionR81`	2,759	`wall4_multiloop_fakeon_unitarity_and_pinch_resolution_capstone_r81`	Sec. 5
7	`Neon_NonPerturbativeWetterichFRGReuterFixedPointR70`	1,658	`gaussian_ir_fixed_point_saddle_r70`	Sec. 3
8	`Neon_NonPerturbativeWetterichFlowsAndD4LimitR71`	2,077	`wall4_nonperturbative_wetterich_frg_reuter_capstone_r71`	Sec. 3
9	`Neon_PureGravitonGhostOneLoopTHVAndWardR69`	9,841	`wall4_pure_graviton_ghost_thv_ward_uv_capstone_r69`	Sec. 3
10	`Neon_WeylSquaredC2HigherDerivFRGR75`	4,352	`wall4_weyl_squared_c2_higher_deriv_frg_capstone_r75`	Sec. 3
11	`W4Neon_CutoffSchemeHomotopyAndPureTypeIR3`	4,098	`wall4c_cutoff_homotopy_and_pure_typeI_r3_capstone`	Sec. 4
12	`W4Neon_FiveCouplingFRGGoroffSagnottiR1`	3,864	`wall4c_five_coupling_frg_goroff_sagnotti_r1_capstone`	Sec. 4
13	`W4Neon_LeeWickPolesAndDoubleFoldScurveBifurcationR6`	5,045	`wall4c_leewick_poles_and_double_fold_scurve_r6_capstone`	Sec. 4
14	`W4Neon_MatterPhaseBoundaryScalarPoleAndGenerationWindowR5`	3,105	`wall4c_matter_phase_boundary_and_generation_window_r5_capstone`	Sec. 4
15	`W4Neon_RouthHurwitzUVStabilityAndE4R2`	5,574	`wall4c_routh_hurwitz_uv_stability_and_e4_r2_capstone`	Sec. 4
16	`W4Neon_StandardModelMatter5CouplingFRGAndC3StabilityR4`	3,789	`wall4c_standard_model_matter_5coupling_frg_r4_capstone`	Sec. 4
17	`W4Opus_AboveThresholdKiteFakeonAndUnitaritySumR11`	842	`above_threshold_kite_fakeon_and_unitarity_sum_capstone`	Sec. 5
18	`W4Opus_AboveThresholdThreeBodyFakeonR11b`	1,175	`above_threshold_threebody_fakeon_capstone`	Sec. 5
19	`W4Opus_AboveThresholdTriangleFakeonR11a`	794	`above_threshold_triangle_fakeon_capstone`	Sec. 5
20	`W4Opus_AllOrderFakeonUnitarityR7`	966	`all_order_fakeon_unitarity_capstone`	Sec. 5
21	`W4Opus_BidirectionalFRGFlowR9b`	1,962	`contraction_of_SB2`	Sec. 3
22	`W4Opus_BidirectionalFourCouplingFRGContractionR9`	103	`bidirectional_four_coupling_frg_contraction_capstone`	Sec. 3
23	`W4Opus_BubbleLimitAllLoopUnitarityR1d`	247	`bubble_limit_all_loop_unitarity_capstone`	Sec. 5

Continued on next page

Table A1 – *continued from previous page*

#	Audited Lean 4 Module	Lines	Primary Capstone / Key Declaration	Section
24	W4Opus_CompleteUVToIRStelleFlowR2	252	complete_uv_ir_stelle_flow_capstone	Sec. 6
25	W4Opus_Coupled4DGravityRSUVFixedPointR6	1,055	coupled_4d_gravity_rs_uv_fixed_point_capstone	Sec. 6
26	W4Opus_FRGContractionCertificateR9c	1,640	xF_enclosure	Sec. 3
27	W4Opus_FakeonComptonPrecursorR1c	392	fakeon_compton_microcausality_capstone	Sec. 5
28	W4Opus_FiveCouplingFRGCertificateR12b	2,608	bidirectional5	Sec. 3
29	W4Opus_FiveCouplingGoroffSagnottiFRGR12	384	five_coupling_goroff_sagnotti_frg_capstone	Sec. 3
30	W4Opus_GoroffSagnottiFiveCouplingFlowR12a	1,193	T_of_fp5	Sec. 3
31	W4Opus_IrreducibleTwoLoopMixedFakeonR4	654	irreducible_two_loop_mixed_fakeon_capstone	Sec. 5
32	W4Opus_LitimFourCouplingFixedPointR6a	904	stab_eigen	Sec. 6
33	W4Opus_MatterCoupledFiveCouplingFRGR14	997	matter_coupled_five_coupling_frg_capstone	Sec. 3
34	W4Opus_MatterCoupledFiveCouplingFlowR14a	936	quintic_factor	Sec. 3
35	W4Opus_MatterFRGCertificateRSR14b	2,998	a_row_at_fp	Sec. 3
36	W4Opus_MatterFRGCertificateRSTypeIIFarR14i	3,111	a_row_at_fp	Sec. 3
37	W4Opus_MatterFRGCertificateRSTypeINearR14f	3,011	a_row_at_fp	Sec. 3
38	W4Opus_MatterFRGCertificateRSTypeIR14e	3,113	a_row_at_fp	Sec. 3
39	W4Opus_MatterFRGCertificateSMR14c	2,998	a_row_at_fp	Sec. 3
40	W4Opus_MatterFRGCertificateSMTypeIIFarR14h	3,111	a_row_at_fp	Sec. 3
41	W4Opus_MatterFRGCertificateSMTypeINearR14g	3,011	a_row_at_fp	Sec. 3
42	W4Opus_MatterFRGCertificateSMTypeIR14d	3,113	a_row_at_fp	Sec. 3
43	W4Opus_MatterTypeINewtonShiftR14t	152	newton_shifts_SM_RS	Sec. 3
44	W4Opus_NonFactorizableTwoLoopVertexFakeonR10	1,154	nonfactorizable_two_loop_vertex_fakeon_capstone	Sec. 5
45	W4Opus_ParametricCutkoskyR1a	541	parametric_cutkosky_and_fakeon_one_loop_capstone	Sec. 5
46	W4Opus_RSDiscreteCeilingVsFRGFixedPointR16	649	rs_ceiling_vs_frg_capstone	Sec. 6
47	W4Opus_RSDiscreteFloorUVScalaronStabilizationR5	921	rs_discrete_floor_scalaron_stabilization_capstone	Sec. 6
48	W4Opus_ResummedFakeonUnitarityBoundR1f	184	resummed_fakeon_unitarity_capstone	Sec. 5
49	W4Opus_SixBySixSpectralAlgebraR15s	394	quad_rest6	Sec. 3
50	W4Opus_SixCouplingCertificatePureR15b	8,226	xF_signs	Sec. 3

Continued on next page

Table A1 – *continued from previous page*

#	Audited Lean 4 Module	Lines	Primary Capstone / Key Declaration	Section
51	`W4Opus_SixCouplingCertificateRSTypeINearR15f`	9,133	`xF_signs`	Sec. 3
52	`W4Opus_SixCouplingCertificateRSTypeIR15d`	9,408	`xF_signs`	Sec. 3
53	`W4Opus_SixCouplingCertificateSMTypeINearR15e`	9,133	`xF_signs`	Sec. 3
54	`W4Opus_SixCouplingCertificateSMTypeIR15c`	9,408	`xF_signs`	Sec. 3
55	`W4Opus_SixCouplingR3C3FRGR15`	556	`six_coupling_r3_c3_frg_capstone`	Sec. 3
56	`W4Opus_SixCouplingR3C3FlowR15a`	1,236	`lift6_noSource`	Sec. 3
57	`W4Opus_StelleFlowFirstIntegralR2a`	308	`solution_characterization`	Sec. 6
58	`W4Opus_StelleFlowTrajectoryR2b`	400	`explicit_uv_ir_trajectory_capstone`	Sec. 6
59	`W4Opus_StelleHealthyWindowR2c`	340	`healthy_window_capstone`	Sec. 6
60	`W4Opus_StelleLitimThresholdsR9a`	490	`T_inv`	Sec. 3
61	`W4Opus_SunsetThresholdR1b`	375	`two_loop_sunset_threshold_and_fakeon_capstone`	Sec. 5
62	`W4Opus_SunsetWeightedCutR1e`	124	`sunset_weighted_cut_capstone`	Sec. 5
63	`W4Opus_TwoLoopFakeonOpticalUnitarityR1`	280	`two_loop_fakeon_optical_unitarity_capstone`	Sec. 5
64	`W4Opus_Wall4MasterCapstoneR8`	574	`wall4a_master_capstone_r8`	Sec. 6
65	`W4Opus_ZeroWidthDistributionalFakeonUnitarityR13`	2,055	`zero_width_distributional_fakeon_unitarity_capstone`	Sec. 5